The application and suitability of unmanned airborne vehicle based imagery to determine river dynamics:
A case study of the Buëch in France

The Buëch at La Bâtie-Montsaléon 2015

Master Thesis – Earth Surface and Water
Hazards & Earth Observation
30 June 2016 (2nd version)

Sven Hemmelder (3858057)
S.D.Hemmelder@students.uu.nl
Utrecht University

Utrecht University
Department of Physical Geography

1st supervisor Prof. Dr. S.M. De Jong
2nd supervisor Dr. W.A. Marra

Acknowledgments

Abstract

The Buëch is a dynamic river in south-eastern France with active erosion and accretion processes. In this river both alternating braiding and meandering patterns occur. Bank erosion has resulted in the closure of roads and the loss of agricultural lands. Therefore, it is important to monitor and better understand river dynamics. In this study, a method is developed to derive and describe the changes in geomorphological features using Unmanned Airborne Vehicle (UAV) based imagery and the positional accuracy in XYZ directions of the UAV products are determined and evaluated.

Three research locations along the Buëch have been established, providing imagery for multiple years. At each location in 2014 and 2015, a Differential Global Positioning System (DGPS) was used to measure the location of markers that were used as Ground Control Points (GCPs). OrthoMosaics and Digital Elevation Models (DEMs) were created using the Structure from Motion (SfM) algorithm available in Agisoft PhotoScan. The OrthoMosaics have a high resolution (cell size) of approximately 3 cm and the OrthoDEMs have a resolution of approximately 6 cm. The positional accuracy is on average approximately 30 cm in the XY-direction and 2 cm in the Z-direction. The created time series enables description of erosion and accretion processes on a sub meter scale which yields an increase in insight of the river dynamics of the Buëch.

With OrthoMosaics and OrthoDEMs riverbed morphology and patterns can be mapped and quantified. The result show significant changes in geomorphology over the timespan monitored (2014-2015). Channel displacements of up to 20 m are observed at La Bâtie-Montsaléon. Bank erosion in general reaches up to 3 m in width. At La Bâtie-Montsaléon, a part of the river bank including trees on top with a length of 150 m and a maximum width of 40 m eroded. This resulted in a volume change of 5853.55 m^3. This river bank erosion was not recognised without the OrthoMosaics and OrthoDEMs on basis of the UAV imagery.

Table of Contents

List of Figures

List of Tables

List of Abbreviations

DEM	*Digital Elevation Model*
DGPS	*Differential Positioning System*
DSM	*Digital Surface Model*
DTM	*Digital Terrain Model*
GCP	*Ground Control Point*
GNSS	*Global Navigation Satellite System*
GPS	*Global Positioning System*
IGN	*Institut Géographique National*
LiDAR	*Light Detection And Ranging*
MVS	*Multi-View Stereo*
NDVI	*Normalized Difference Vegetation Index*
NIR	*Near-Infrared Reflectance*
OBIA	*Object Based Image Analysis*
RGB	*Red Green Blue*
RTK	*Real Time Kinematic*
SfM	*Structure from Motion*
SIFT	*Scale Invariant Feature Transform*
TLS	*Terrestrial Laser Scanner*
UAV	*Unmanned Airborne Vehicle*
UTM	*Universal Transverse Mercator*
WGS	*World Geodetic System*

1 Introduction

1.1 Relevance

Many rivers are controlled by humans. For example, conditions like discharge, temperature and quality of the rivers are continuously measured in the Netherlands. In addition, humans have influenced entire stretches of rivers. River banks have been fixed by placing boulders, meander belts have been cut off to straighten the channel and groynes have been placed to influence flow velocity and river depth. As a result the erosion is minimal, banks are protected and there is no material deposited passed the floodplains (*Frings et al., 2009*). To protect urban areas for high water, dykes or levees have been built (*Frings et al., 2014a, 2014b*) to assure the safety for areas alongside the river when there is an increase in discharge due to precipitation or snowmelt upstream.

In contrast, rivers can be highly dynamic, especially when there is no human influence. During events, channels can displace, start or stop meandering and banks can be eroded. The Buëch in south-eastern France is an example of a highly dynamic river. This river is not continuously monitored or modified. The embankments are generally not fixed and thus the Buëch can meander freely. Floods and erosion occur regularly during high discharge (*Descroix and Gautier, 2002*). Understanding river dynamics is highly relevant for socio-economic reasons. Such rivers may erode agricultural land and infrastructure like roads and railways. The Buëch is a key location to gain more knowledge about river dynamics.

1.2 The Buëch

The river Buëch is used as a case study and is located in the south-eastern part of France. In the research area, the erosion caused by the Buëch has resulted in loss of agricultural lands and closure of roads. The river system of the Buëch consists out of le Grande Buëch and le Petit Buëch that confluences just upstream of Serres. The Buëch is located in the mountain range the Pre-Alps in the department the Hautes-Alpes (*Figure 1.1*).
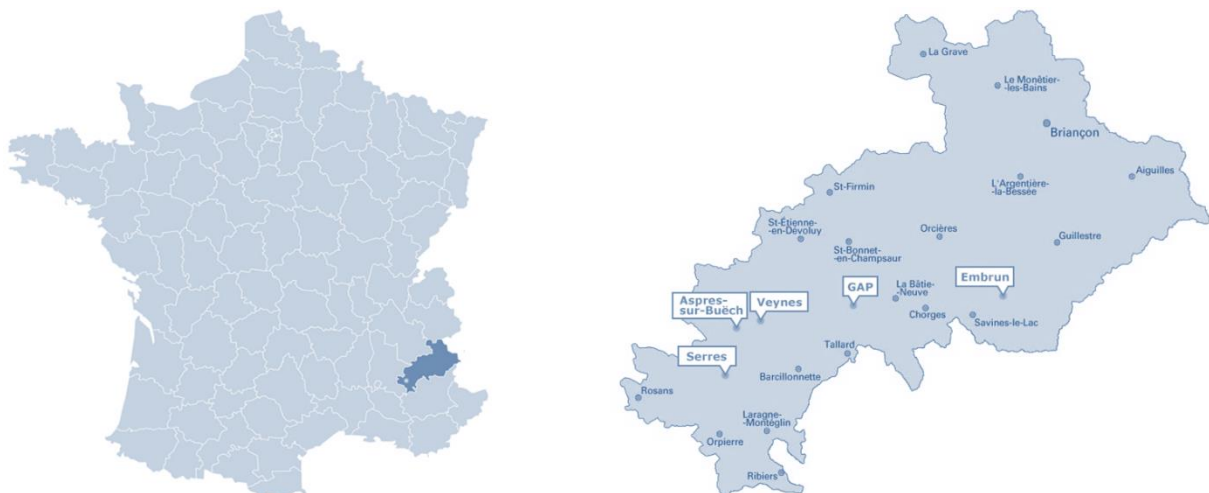
Figure 1.1 (A) Department Hautes-Alpes. (B) Detailed map of Hautes-Alpes with location of the larger communities. The Buëch flows alongside Serres.

The source of le Grande Buëch is located on the western flank of the Massif du Dévoluy. Le Grande Buëch has a length of 85.2 km and a basin of 1490 km^2 (*Sandre, 2016*). Le Petit Buëch originates from the south-east part of the Massif du Dévoluy and has a length of 44.5 km with a basin of 389 km^2 (*Sandre, 2016*). The highest point of the Massif du Dévoluy is 2789 m and the area primarily consists of limestone. The Buëch flows mostly across areas with forest (approximately 78%) and agriculture (approximately 21%). Urban areas are uncommon (less than 1%) alongside to the Buëch (*Sandre, 2016*). In general, the course of the river is natural. Only near communities the river course is occasionally adapted. This river system has a snow regime (*Descroix and Gautier, 2002; Liébault et al., 2013*). The main tributary of le Petit Buëch is the Béoux. The Buëch confluences with the Durance which flows through the Rhône towards to Mediterranean Sea (*Sandre, 2016*).

During the Holocene period the Buëch had varying characteristics (*Descroix and Gautier, 2002*). In the pre-Boreal period (10300 – 8000 years BP) to the Atlantic period (7600 – 4500 BP) the Buëch had a phase of deposition of mainly loamy, gravelly or even finer materials. At the Sub-Boreal period (4500 – 2800 BP) incision occurred. During this phase of erosion only deposits with cobbles or boulders could be found. From the Sub-Atlantic (2800 – 700 BP) to the present the Buëch is again in a low erosion stage (*Descroix and Gautier, 2002*). Nevertheless, the Buëch is a dynamic system with accretion and erosion processes (*Liébault et al., 2013*).

Two types of floods can occur in the Buëch region (*Descroix and Gautier, 2002*). Mediterranean (thunder) storms can occur in the summer and at the start of autumn. During these storms precipitation occurs with a high intensity and high volume. This results in a rapid increase of the discharge of the Buëch. The second flood type occurs during winter when westerly storms result in long periods of precipitation. Consequently, there is a slow but steady increase of the discharge of the Buëch. Sometimes this can occur together with snowmelt generating larger volumes of discharge.

The Buëch has similar to many other rivers in the French Alpine region a sediment deficient. This is mostly caused by quarries that are either active or inactive. These quarries are used to excavate gravel. In addition, there are dams in the river that trap sediments. This disturbs the sediment budget. The resulting sediment deficient causes an increase in uptake of sediments or entrenchment (*Descroix and Gautier, 2002; Frings et al., 2014b*). Furthermore, the Buëch is a difficult river to classify. Depending on moment of observation, the river has either braided, meandering characteristics or a combination of both. Therefore, it is important to know factors like channel displacements, bank displacements and bank erosion.

1.3 Discharge Buëch

There was a hydrological measuring station located at Les Chambons near Serres since 1964 (*HYDRO, 2016*). This location is just passed the confluence of le Grande Buëch and le Petit Buëch. The measuring station was built in 1964 and operated until it was damaged in 2009 due to an erosion event. The measuring station was never rebuilt or repaired. Between 2009 and 2012 there is a provisional dataset available which contains estimate discharge data. A verified dataset is available that averages the conditions from 1969 to 2011 (*Table 1.1* and *Figure 1.2*).

Table 1.1 Average discharge per month in m^3/s for the Buëch at Les Chambons from 1969 to 2011.

	Jan	Feb	Mar	Apr	May	Jun	Jul	Aug	Sep	Oct	Nov	Dec	Year
Discharge (m^3/s)	15.40	15.50	21.00	26.70	22.50	11.30	4.58	2.69	4.40	11.6	17.30	14.80	*14.00*
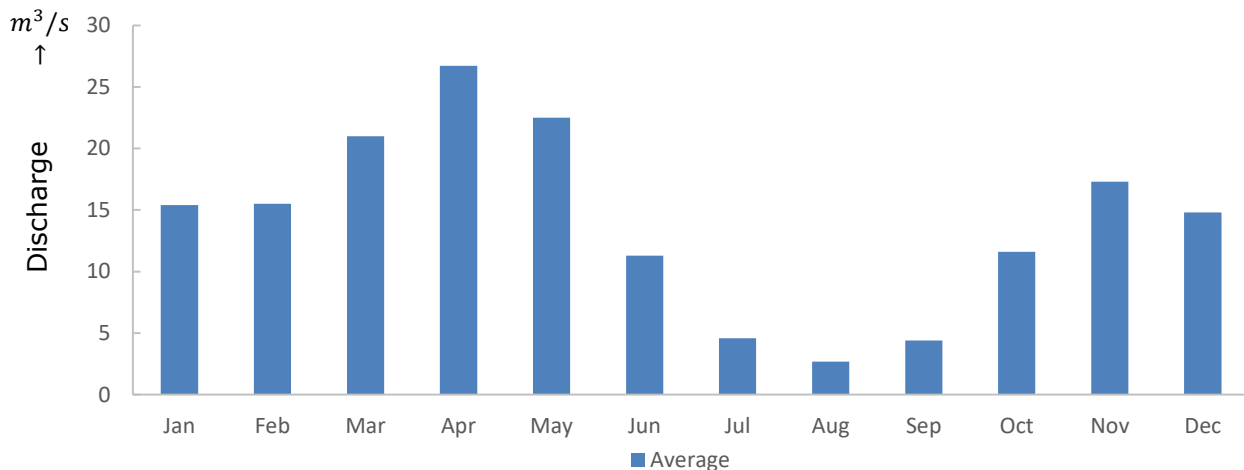
Figure 1.2 Graph of average discharge per month in m^3/s for the Buëch at Les Chambons from 1969 to 2011 (*HYDRO, 2016*).

1.4 Research locations

Three different research locations alongside the Buëch have been established (*Figure 1.3*). Two research locations are located before le Grand Buëch and le Petit Buëch confluences and one research location is located downstream this point.

Chabestan is the most upstream research location at le Petit Buëch. In the middle there is La Bâtie-Montsaléon at le Petit Buëch. The La Bâtie-Montsaléon site is located near an active quarry (*Descroix and Gautier, 2002*). The third research location is situated just downstream of Serres near the Saint-Sauveur Dam. This is downstream of the point where le Grand Buëch and le Petit Buëch confluences. The distance from the research location at Chabestan to the research location at Serres is approximately 10 kilometres. At each site a distance of approximately 1000 m is covered.
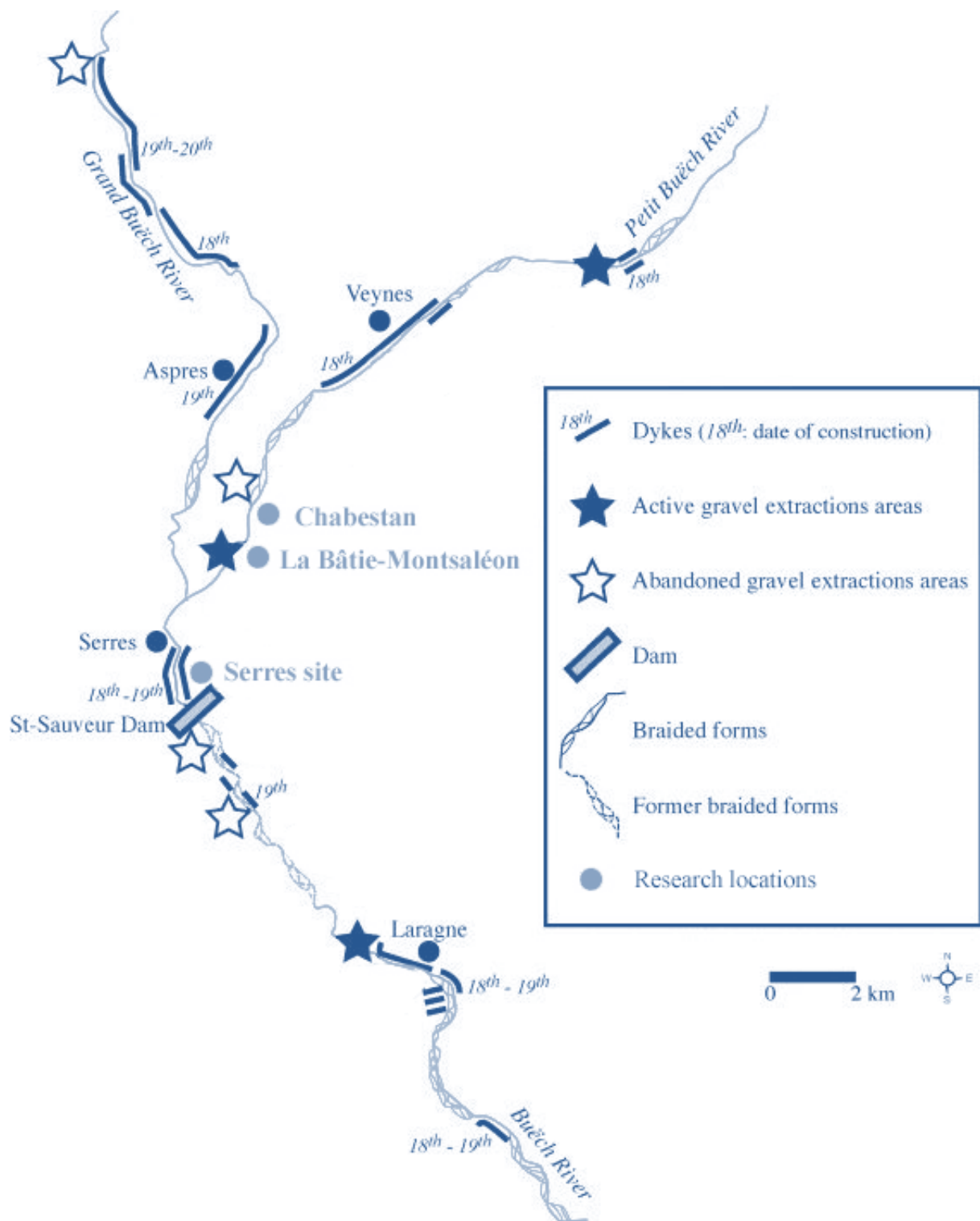
Figure 1.3 Map of the Buëch river system with the research locations: Chabestan, La Bâtie-Montsaléon and Serres. In addition, the location of confluence of le Grande Buëch and le Petit Buëch is indicated. Human influences such as the largest cities, active and abandoned quarries, locations with dykes and dams are also depicted. This map is adapted from Descroix and Gautier (*2002*).

1.5 Climate Hautes-Alpes

There is no climate data available for Chabestan, La Bâtie-Montsaléon or Serres. The closest weather station is situated in Embrun at an elevation of 871 m (*LaMétéo, 2016*) which is approximately 80 km of Serres. This weather station has collected records of temperature (*Table 1.2* and *Figure 1.4*) and precipitation (*Table 1.3* and *Figure 1.5*) from 1981 to 2010. The temperature is high during summer with an average of approximately 20 °C even though the Hautes-Alpes is a mountainous area. The number of sunshine hours is high. The winters are cold with on average 25 days with heavy frost (<-5 °C) and 98 days below zero.

Table 1.2 Embrun (Hautes-Alpes) temperature data from 1981-2010 (*LaMétéo, 2016*).

Temperature	Jan	Feb	Mar	Apr	May	Jun	Jul	Aug	Sep	Oct	Nov	Dec	Year
Minimum (°C)	-2.8	-2.5	0.6	3.4	7.5	10.6	13.1	12.9	9.6	6.2	1.1	-1.7	*4.8*
Maximum (°C)	6.8	8.4	12.4	15.2	19.7	23.8	27.0	27.0	22.3	17.1	10.8	7.1	*16.5*
Average (°C)	2.0	3.0	6.5	9.3	13.7	17.2	20.3	20.0	16.0	11.7	6.0	2.7	*10.7*
< -5 °C (days)	8.4	6.7	2.2	0.0	0.0	0.0	0.0	0.0	0.0	0.0	1.7	5.9	*24.9*
< 0 °C (days)	23.9	20.5	13.4	4.9	0.6	0.0	0.0	0.0	0.0	1.8	12.1	20.8	*98.0*
> 25 °C (days)	0.0	0.0	0.0	0.1	3.2	13.4	23.6	22.5	8.9	0.5	0.0	0.0	*72.2*
> 30 °C (days)	0.0	0.0	0.0	0.0	0.2	2.5	8.1	7.0	0.6	0.0	0.0	0.0	*18.4*
>35 °C (days)	0.0	0.0	0.0	0.0	0.0	0.0	0.2	0.2	0.0	0.0	0.0	0.0	*0.4*
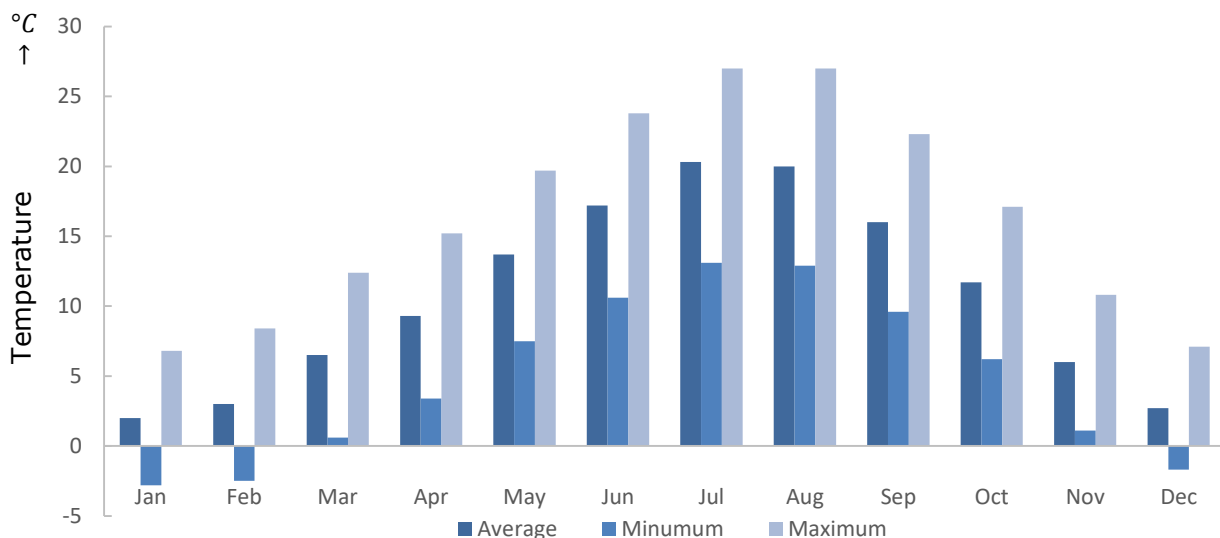
Figure 1.4 Graph of the Embrun (Hautes-Alpes) average monthly minimum, average monthly maximum and average monthly (1981-2010) temperature data in °C (*LaMétéo, 2016*).

The number of days with rain is low in the Hautes-Alpes. Nevertheless, the cumulative precipitation is 723 mm per year. In summer, there are many thunderstorms in the mountains. Throughout the year, there are on average 25 days with heavy precipitation (>10 mm). Erosive storms of 10 mm or more on one day occur mainly in October and September (*Table 1.3*). This can result in a vast increase in discharge and probably erosion events.

Table 1.3 Embrun (Hautes-Alpes) precipitation data from 1981-2010 (*LaMétéo, 2016*).

Precipitation	Jan	Feb	Mar	Apr	May	Jun	Jul	Aug	Sep	Oct	Nov	Dec	Year
Monthly (mm)	51.8	45.1	50.1	61.2	68.0	60.5	46.8	51.9	69.0	85.8	67.5	65.1	*723*
> 1 mm (days)	5.8	5.0	6.2	8.0	9.4	8.1	5.8	6.7	6.6	8.4	6.6	6.6	*83.2*
> 5 mm (days)	3.1	3.0	3.4	4.0	4.3	3.9	2.7	3.3	3.5	4.8	3.9	3.9	*43.8*
> 10 mm (days)	1.7	1.7	2.3	2.3	2.3	1.9	1.6	1.6	2.6	3.0	2.4	2.2	*25.0*
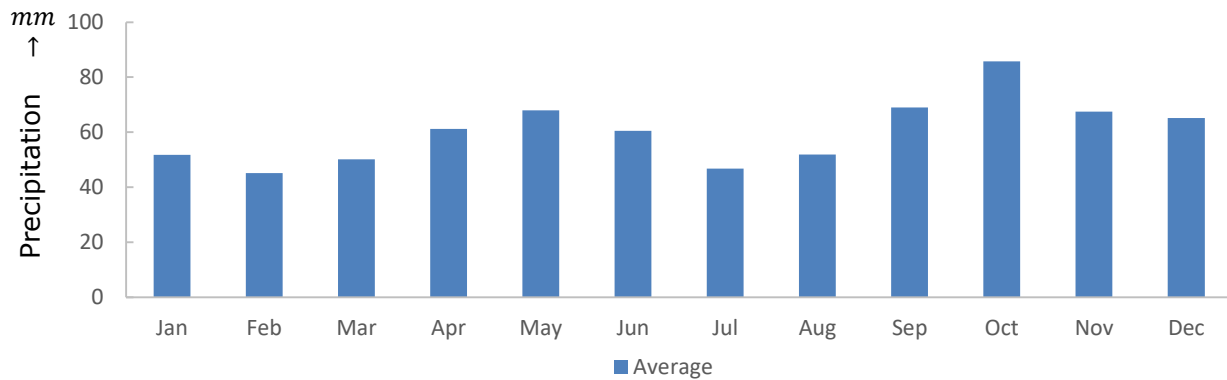
Figure 1.5 Graph of the Embrun (Hautes-Alpes) average monthly precipitation data (1981-2010) in mm (*LaMétéo, 2016*).

The average annual discharge data shows that there are two periods with high discharge. The increase in discharge starts in February and reaches its maximum in April with an average discharge of 26.70 m^3/s. This occurs in the spring when the temperature increases and snow melt starts. During the summer, there is a low discharge around 2.69 m^3/s. The second increase occurs in the autumn and reaches its peak in November with an average discharge of 17.30 m^3/s caused by rainfalls.

1.6 Research with Unmanned Airborne Vehicles (UAVs)

Unmanned Airborne Vehicles (UAVs) are increasingly used and are an evolving tool to acquire datasets. Datasets acquired with UAVs have a high resolution in which subtle changes of the surface are detectible (*Westoby et al., 2012*). The UAV products can be compared with either conventional photogrammetry or with laser based derived products such as Light Detection And Ranging (LiDAR) and Terrestrial Laser Scanner (TLS) and have a higher resolution compared to most satellite products (*Smith et al., 2015*).

An important advantage of flying with UAVs is that it is relatively cheap compared with other remote sensing techniques. There is no need for an expensive TLS device or even a piloted plane. UAVs can acquire a dataset with just a compact camera. This result in a lightweight tool that can easily be transported. UAVs are usable in all types of environments of different sizes on a moment notice (*Fonstad et al., 2013; Miřijovský and Vavra, 2012*). The UAV datasets are intuitive. They are similar to other point cloud based data products. An upcoming difficulty with UAV is legislation. Depending on the location, legislation is already strict or might become even more strict in the future (*Miřijovský and*

Langhammer, 2015; Smith et al., 2015). UAVs mostly uses light weight sensors and consequently Red Green Blue (RGB) and sometimes infrared cameras are most commonly used. Heavier sensors for example thermal sensors are generally not usable with UAVs (*Fleury et al., 2015; Smith et al., 2015*).

UAVs are used in many different research fields. UAVs are often used in research related to landslides to determine the surface displacements or fissures (*Marek et al., 2015; Niethammer et al., 2010, 2012*). It can also be used to monitor the activity and dynamics of the landslides (*Turner et al., 2015*). Furthermore, UAVs can be used in colder environments for monitoring glaciers (*Bhardwaj et al., 2016; Immerzeel et al., 2014; Kraaijenbrink et al., 2016*)

In addition, UAVs are increasingly used in fluvial geomorphological research. Here, the focus is on mapping of river channels, topography (*Dietrich, 2016*) and some type of change detections with growing meander belts (*Flener et al., 2013*). The UAVs are used to derive and map fluvial dynamics (*Miřijovský and Langhammer, 2015*) and bank erosion (*Prosdocimi et al., 2015*).

1.7 Research questions

This thesis is split up into two themes: A technical theme (*results chapter 3.1*) and a river dynamics theme (*result chapter 3.2, 3.3, 3.4 and 3.5*).

In the technical theme the focus is on the effectiveness of acquired data with Unmanned Airborne Vehicles (UAVs). Any difficulty such as quality problems or problems experienced during acquisition will be analysed and if applicable solved. The main goal is to determine if the UAV techniques are advanced and accurate enough to use the workflow derived in this thesis for fluvial geomorphological research at different locations.

The second theme focusses on the river Buëch dynamics and the changes in geomorphology of the river between observed years. This includes bank erosion, channel displacements and deposition or accretion processes.

To achieve the scope set for this study, the river Buëch will be used as case study. Additionally, two separate research questions, one for each theme, are defined:

1. How does the OrthoMosaics and OrthoDEMs, derived by UAV mapping, relate with the Different Global Position System (DGPS) measurements in terms of positional accuracy and elevation?

2. What is the change in geomorphological features over multiple years at various locations along the Buëch?

2 Materials and Methods:

In this chapter the available datasets of the research locations, the used materials for acquiring the datasets, the implementation of the fieldwork, the processing methods with fundamental algorithms and analysing methods are described.

2.1 Available Datasets

This research uses mainly imagery that has been acquired by a fixed-wing UAV owned and operated by Utrecht University. In addition, there are also datasets addressing the research locations available from the French institute for information about geography and forestry, Institut Géographique National (IGN).

2.1.1 Unmanned Airborne Vehicle (UAV) based datasets

There are three established research locations for which UAV-based datasets were acquired. Each dataset consists of many photographs saved as JPG files taken with a short time interval (*Figure 2.1*). The sites were visited each year during a field campaign, that was carried out each year, within roughly the same period. Not every research site has complete records and the available data varies per location. The number of photographs acquired per location per year varies (*Table 2.1*). The datasets have more than 4600 photographs for all years combined. The amount of photographs largely depends on the size of the area that was covered and the number of flights.
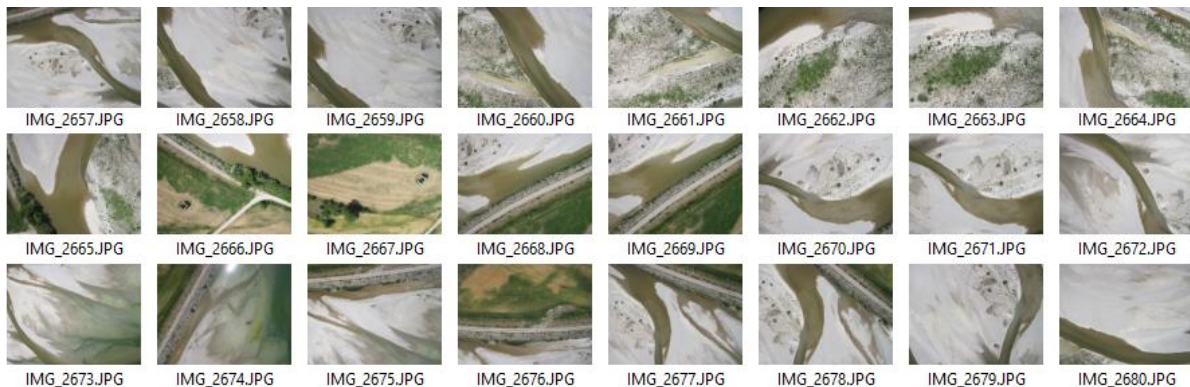
Figure 2.1 Example of a small part of the Serres 2015 dataset. The photographs are acquired consecutively.

Table 2.1 The availability of acquired datasets and number of photographs from 2002 onwards. When a certain year is coloured green the dataset is acquired with markers, orange the dataset is acquired without the use of markers and when a certain year is red the dataset is absent.

	2002	2010	2011	2013	2014	2015
La Bâtie-Montsaléon	63	926	164		473	696
Chabestan				84	380	665
Serres					374	779

The first UAV flight was carried out in 2002 at La Bâtie-Montsaléon. This is the oldest dataset in the time series. This dataset contains photographs without markers or metadata such as the photograph GPS location or platform altitude. After 2002, no data was acquired until 2010. From 2010 onwards the goal was to have a dataset each year. However, this was dependent on weather, time constraints and personal availability during the fieldworks. In 2010 and 2011, more UAV flights were carried out in La Bâtie-Montsaléon. However, there is no dataset for 2012. In 2013, an UAV flight was carried out for the first time at another location called Chabestan. There was no UAV flight in the same year at La Bâtie-Montsaléon.

In the year 2014, it was the first time that the third location Serres was used as a research location. Furthermore, in 2014, the methodology changed as since that year markers were used as Ground Control Points (GCPs) while acquiring the imagery. Also each research site was visited within the same field period. In 2014 and 2015, all three datasets including markers were acquired. As of 2015, the most complete record is La Bâtie-Montsaléon, followed by Chabestan and Serres. However, the years 2014 and 2015 are most suitable to quantify river dynamics, as the markers enables geo-referencing and thereby enable the option to compare the datasets with each other. When markers were used during the acquisition of the dataset then the markers locations are available. These files contain: the GCP Number, date and time of measurement, X-coordinate, Y-coordinate and height of the measurements. Sometimes, there is also a remark added to provide more detailed information on the measurement location.

2.1.2 Institut Géographique National (IGN) datasets

The IGN dataset is tiled based and consists of the entire Hautes-Alpes region in which the research locations are situated. Five tiles, in which the Buëch and research locations are situated, were extracted. Version 1 of the dataset was released in 2012. The dataset was renewed in June 2014 and Version 2 depicts the region around May 2013 which falls within the same timeframe as when the UAV datasets were acquired. These French datasets are geo-referenced in the Lambert 93 coordinate system.

The IGN datasets consist of OrthoPhotos and Digital Elevation Models (DEMs). The OrthoPhotos are corrected for distortions in the imagery caused by lens and camera orientation deformations and consequently have a uniform scale. The OrthoPhotos have a resolution of 50 cm while the DEM has a resolution of 5 m. The IGN datasets were not acquired by UAV but by an aircraft. A large disadvantage of this dataset is that the documentation is only available in the French language.

2.2 Materials

The main materials used for this research during the fieldwork and data acquisition were an UAV, markers with coordinates, a compact camera and a Differential GPS. The acquired data was processed on a dedicated computer with dedicated software for UAV imagery.

2.2.1 Fixed-Wing UAV

For this kind of research, there are two types of UAV that can be used, copters with multiple rotors that take off vertically or fixed-wing UAVs that are more similar to traditional aircraft but take off horizontally. A fixed-wing UAV (*Figure 2.2*) was used based on the need to cover a large area quickly. A launch platform was used to easily launch the UAV.

The UAV is made out of Styrofoam, which is very light-weight and durable. There is a single rotor above the wings which controls the velocity. The rotor can be turned on and off on demand to minimise vibrations within the UAV. Contact with the UAV is kept by radio and is manually steered and thus the UAV needs to remain within visual range. The UAV height and steering is controlled by using the flaps that are installed at the tail.

Figure 2.2 Side-view from the in 2015 used fixed-wing UAV connected with the launch platform.

Within the UAV, below the wings, a rechargeable battery is installed. It is only used for powering the rotor and has a capacity to keep the UAV in the air for approximately 10 to 15 minutes. If needed, the battery can easily be swapped out for another battery. In the front of the UAV there is a socket for a compact camera. The camera is exchangeable. This enables the use of different sensors. For example, a Near-Infrared Reflectance (NIR) camera can be used instead of a Red Green Blue (RGB) camera to calculate the normalized difference vegetation index (NDVI) which can be used to mask out vegetation. To take a photograph, the camera is manually triggered via a radio signal. The inside is painted black to minimise the distortion caused by light reflections. The coordinates of the UAV during flight are unknown as there is no standard GPS and altimeter on-board.

2.2.2 Camera

Due to weight constraints it is important that the camera used in the UAV is light-weight. Another important factor is that the camera is durable because the landings of the UAV can be rough. The camera must be small as there is not much room in the socket to place the camera. Therefore, compact cameras are suitable. This type of camera meets the requirements and provide good quality photographs.

The Canon PowerShot D10 (*Figure 2.3*) was used to take photographs for all the 2013, 2014 and 2015 datasets. This is a light-weight camera that is especially useful for outdoor image acquisition as it is firm, durable and can handle some drops and shocks without suffering any damage. The camera is dirt and waterproof which is useful for fluvial geomorphological research. The firmware of the camera was modified in such a way that it could be triggered to take photographs over radio contact. The photographs are saved in JPG format and contain the metadata with camera settings.

Figure 2.3 The Canon PowerShot D10, the camera used to acquire the imagery for the datasets in 2013, 2014 and 2015.

Some camera parameters (*Table 2.2*) are predetermined. The most important one is focal length. This is the distance between the lens and its focus point. This fixed focal length is used in many calculations. The focal length is the basis to determine the distance of a certain object from the lens. In practice, the focus length might vary slightly. Therefore, the focal length is updated during the calculations. The resolution and pixel size is high to assure that small details will be visible in the photographs.

Table 2.2 The camera parameters that are predetermined for the 2013, 2014 and 2015 datasets.

Camera Model	Resolution	Focal Length	Pixel Size	Pre-calibrated
Canon PowerShot D10	4000 x 3000	6.2 mm	1.54199 x 1.54199 µm	No

Other parameters are not predetermined and vary between the photographs. These variables differ each time to optimise the quality. The most important variables are the F-Stop, exposure time and ISO-speed. The F-Stop is a dimensionless number that can quantify the lens speeds which determines the depth of field and sharpness of the objects. The exposure time is the length of time that the sensor is exposed to light and determines the brightness. The ISO-speed determines the sensitivity of the sensor. However, with a higher value the noise in the image will increase and thus if possible the ISO-speed needs to be small.

Before 2013, different cameras were used by Utrecht University (*Figure 2.4*). In 2002, the Canon PowerShot S10 was used while in 2010 and 2011 the Canon Digital IXUS 85 IS acquired the photographs. These cameras were less durable as they are not waterproof or shock resistant and are more likely to be damaged during landing. The photographs are saved as jpg file, the same data format that is used for the newest datasets.

Figure 2.4 (A) The Canon PowerShot S10 used in 2002. (B) Canon Digital IXUS 85 IS used in 2010 and 2011.

Both cameras have also predetermined parameters (*Table 2.3*). Similar, as with the other camera, the variables such as F-Stop, exposure time and ISO-speed are written within the metadata of the files. The specifications such as resolution and pixel size of these cameras are lower than of the Canon PowerShot D10 which can result in images with less details depending on the platform height. All used cameras captured imagery in RGB.

Table 2.3 Camera parameters that are predetermined for the 2002, 2010 and 2011 datasets.

Camera Model	Resolution	Focal Length	Pixel Size	Pre-calibrated
Canon PowerShot S10	1600 x 1200	6.4 mm	3.89996 x 3.89996 μm	No
Canon Digital IXUS 85 IS	3648 x 2736	6.2 mm	1.67981 x 1.67981 μm	No

2.2.3 Markers as Ground Control Points (GCPs)

Markers are used as GCPs in the research area of which the exact location (XY) including the elevation (Z) is known. This information can be used to derive the location and height of the platform at the moment the photograph was created. Markers are also used to orthorectify or georeference imagery. Coded octagon shaped plastic sheets are used as field markers (*Figure 2.5*).

The markers are white and the coding is black to assure a high difference in contrast. There were forty markers available to use. The minimum of three markers are needed to orthorectify or geo-referenced an image. However, when more markers are used the results will improve. These markers in general have a very high accuracy up to centimetres. The location of a marker is measured within the centroid with the highest accuracy possible.

Figure 2.5 Example of a marker (number 38) used in the field.

The coding on the makers corresponds with a number (1 to 40) and is placed 360° around the centre (*Figure 2.6*). This ensures that from each viewing angle there is only one possible solution. In theory, the coding should make it possible to automatically detect the markers within the imagery. If the acquired imagery has sufficient details, then the centre of the markers should be visible in the imagery with readable coding around it.
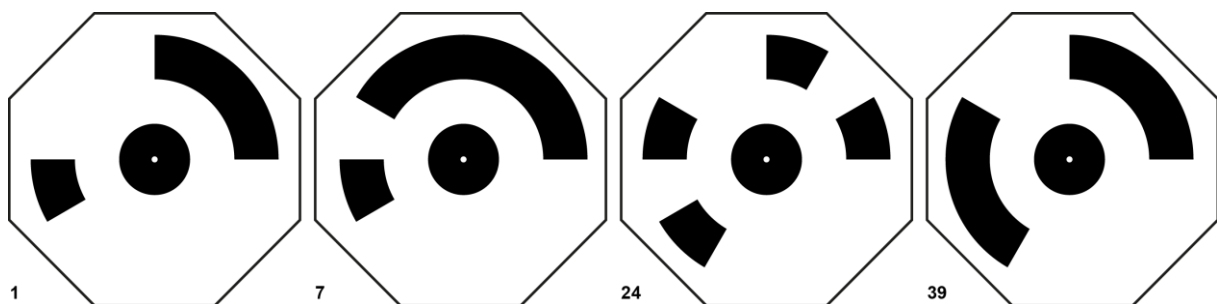
Figure 2.6 Example of the coding on the markers for the values 1, 7, 24 and 39.

2.2.4 Differential GPS

A normal handheld field GPS needs minimal to receive four satellite signals to calculate the location with a clear line of sight as hills and trees will disturb the signal. In a worst case scenario, the accuracy is around 15 m. This is insufficient when the exact location must be determined. Therefore, the errors must be differentially corrected. This is automatically done when a Differential Global Positioning System (DGPS) is used. Such systems do have an accuracy that can reach up to a couple of centimetres (*Malaimani, 2013)*.

The DGPS is not only connected to a satellite signal to determine the exact location but also with another GPS receiver that has an exactly known and fixed location (*Figure 2.7*). In principal, if the DGPS and reference receiver are close enough they will experience the same atmospheric disturbances in the signal, making them comparable. Therefore, when the difference in calculated position of the DGPS is compared with the exactly known location of the second receiver, the more accurate coordinates can automatically be calculated (*Landau et al., 2009; Malaimani, 2013*).
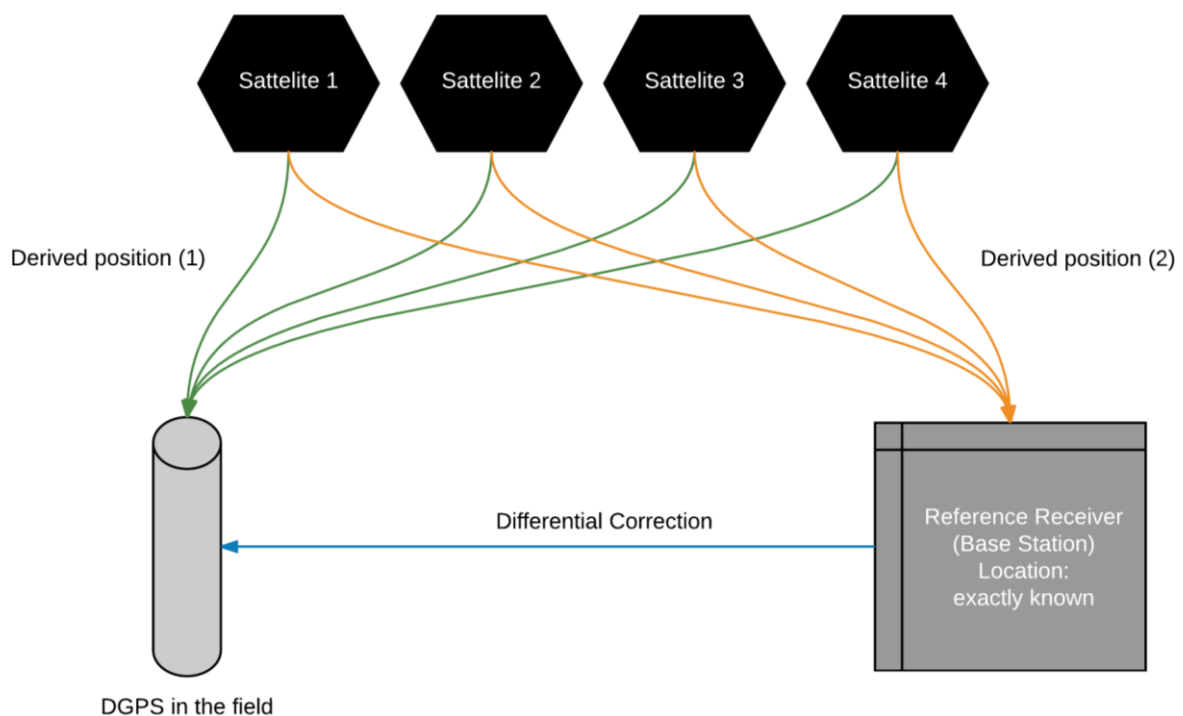
Figure 2.7 Diagram that explains in general how the location measurement error is minimised by a DPGS.

For this research, a Trimble R8 GNSS System was used (*Figure 2.8*). This DGPS uses Real Time Kinematic (RTK) to compute the location measurements. The system was placed on a pole for which the length was known and includes a spirit level. The spirit level is used to assure that the DGPS is standing completely upright when measuring. If not upright, the measurement will be less accurate.

The differential corrections are decoded and not available for free in France. Therefore, a decoder with internet connection and with a subscription was added to the system. The controller has software which enables the user to record the actual coordinates in any coordinates system. The DGPs will only record when the accuracy is lower than a certain threshold. If the threshold is exceeded, the signal needs to improve to continue measuring. In general, the longer the time interval taken for a measurement, the more accurate the measurement becomes.

A.

B.

Figure 2.8 (A) The DGPS that was used during the fieldwork on a pole. (B) The controller of the DGPS on which the coordinate data can be displayed and settings can be edited.

2.2.5 Software

One of the options to process UAV imagery is Agisoft PhotoScan (Agisoft LLC). Agisoft PhotoScan is a commercial fully automated photogrammetric software product that uses the Structure from Motion (SfM) algorithm (*Smith et al., 2015*) to stitch multiple images together to generate spatial data such as high resolution 3D models, OrthoMosaics and OrthoDEMs (*detailed in chapter 2.4.1*). For this reason, Agisoft PhotoScan is used by UAV companies, universities but also game developers and animation studios.

The software works on Windows, OS X and Linux. The software can also be used on network clusters. For this research, the Professional Edition 1.1.6 version was used (*Figure 2.9*). The Professional edition includes, as extra, the ability to geo-reference images by using GCPs and the capability to export OrthoDEMs. These extra are a necessity if the data must be quantified.
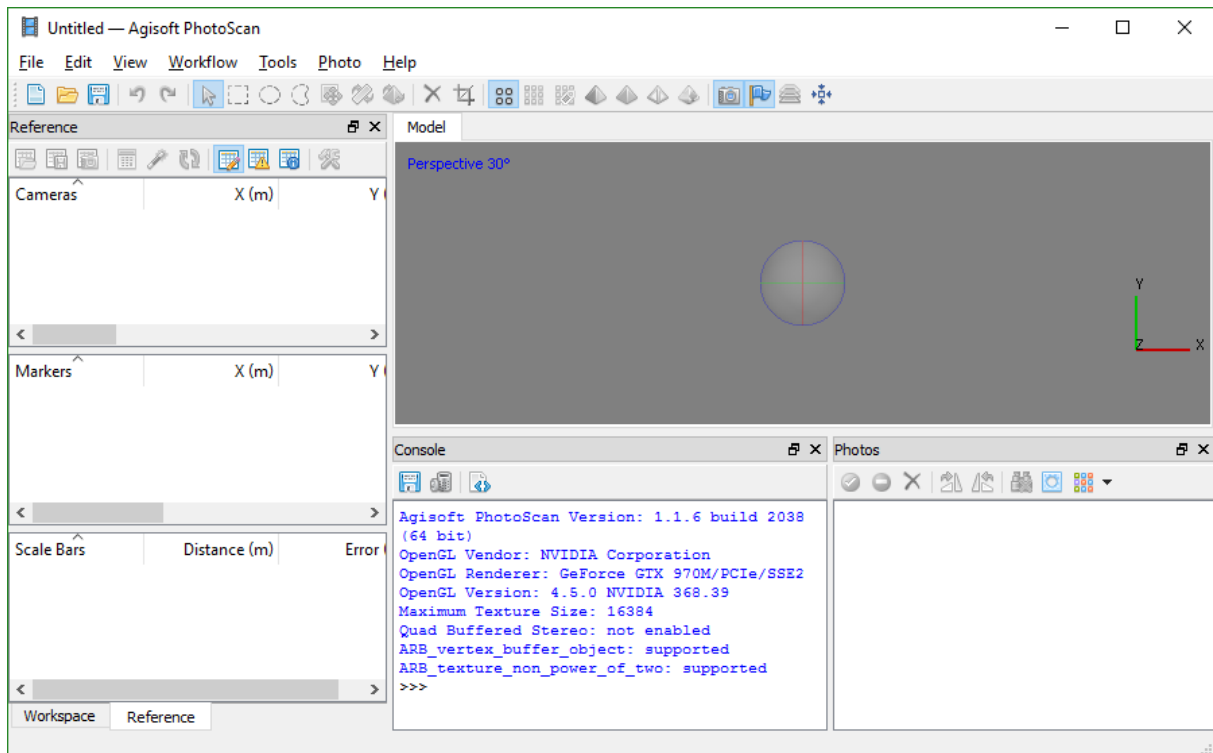
Figure 2.9 An empty workspace in the Agisoft PhotoScan software.

A large advantage of this software package is the easy to follow workflow. It is possible to use Python to fully automate batch runs. A disadvantage of Agisoft PhotoScan are the high system requirements. The program is also usable as viewer for 3D data. The file format used is either PSX or PSZ.

2.2.6 PC

Agisoft PhotoScan is a heavy software package and will not run smoothly on many systems when high accurate processing settings are selected. Therefore, a dedicated system was used to calculate the 3D models, OrthoMosaics and OrthoDEMs.

The most important components of this computer are the processor (CPU) as this controls the speed of the calculations, the memory (RAM), to ensure larger files and datasets can be calculated and the graphics card (GPU) to enhance to calculation time and to easily view the calculated 3D models. The system used (*Table 2.4*) more or less corresponds to the basic system requirements advised by the company behind Agisoft PhotoScan.

Table 2.4 The main specification of the system used to run the Agisoft PhotoScan models.

System specifications	Processor (CPU)	Memory (RAM)	Graphics card (GPU)
	Quad Core i7-4790 @3.60 GHz	32 GB	NVIDIA NVS 315 1024 MB DDR3

2.3 Fieldwork 2015

The fieldwork was performed from 29 May 2015 to 7 June 2015. Within this time depending on weather conditions the datasets for the three research locations needed to be acquired.

2.3.1 Conditions

During this fieldwork, the weather conditions were exceptional. Historical weather (*LaMétéo, 2016*) shows that in May the maximum temperature is 19.7 °C and 23.8 °C in June with an average precipitation of 6.8 cm in May and 6.1 cm in June. However, during the fieldwork, it did not rain for a couple of weeks and the temperature was higher than normal, well above 30 °C at noon. This led to a low water level and discharge of the Buëch. As an advantage, there were many dry river banks visible within the river and the river could more easily be crossed.

2.3.2 In the field

In the fieldwork period, three research sites were visited. The goal was to finish collecting the dataset for a certain location within a single day, as it could not be assured that the weather conditions or discharges were similar on the following day. This was achieved for La Bâtie-Montsaléon and Serres, but not for Chabestan. Chabestan research area was too large to fly in a single day. In general, in the morning markers would be distributed within the area of interest, followed by the UAV flights roughly at noon. The fieldwork could be split up into two main parts: 1. *Distribution of markers across the area and measure the DGPS location of these GCPs.* 2. Acquiring and *checking the UAV imagery whether it covers the entire area without gaps.*

When a site was visited, the first task was to distribute the forty markers across the research area. The aim was to have two or more makers visible within one image. The markers were evenly distributed. A group of markers have a negative effect on the accuracy as the accuracy decrease with distance from a marker. The most important factor in finding a suitable location to place a marker is that it must by easily visible on the photograph. To assure this, markers were if possible put on a flat and sandy location. This gives the highest contrast between the marker and the surroundings. After a marker was placed, the centre was accurately measured with the DGPS. When all markers were in the field, the UAV could start acquiring imagery. Meanwhile, other locations such as the height and edges of banks that experience erosion could be mapped with the DGPs.

After an UAV flight, the acquired imagery was processed in the field with a laptop to an OrthoMosaic. This was done to assure that there were no gaps in the data, that the imagery had enough overlap and that the data completely covered the previous datasets. If these requirements were not met, another flight was necessary with the UAV to fill in the gaps.

2.4 Processing

In this chapter background information will be given about the processing of the sets of UAV imagery using the Structure from Motion (SfM) algorithm. In addition, a general workflow for the Agisoft PhotoScan software will be exemplified into three separate sections: Pre-processing, the algorithms and the exporting of the data.

2.4.1 Structure from Motion (SfM) algorithm

SfM is not a newly developed principle but is adapted from other fields such as photogrammetry and computer vision (*Smith et al., 2015*). It is used to derive point clouds and 3D models from ten to hundreds of photographs (*Favalli et al., 2012*). These derived point clouds and models can be compared with LiDAR and TSL derived products (*Javernick et al., 2014*). The previous techniques have problems with shadowing but as SfM uses multiple different angles, the errors caused by shadowing are minimised (*Niethammer et al., 2012*). SfM is a survey method that is non-selective. In other words, the algorithm determines which points are included or removed (*Smith et al., 2015*).
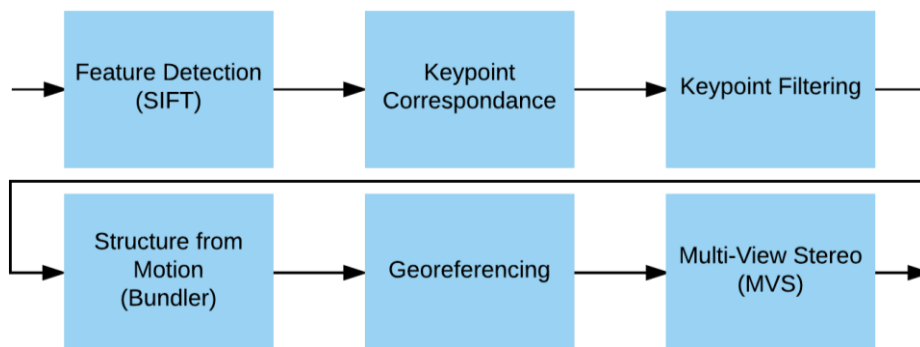
Figure 2.10 Diagram of the principles behind SfM based on Smith et al., 2015. The SfM algorithm uses six different main steps to result in a correct 3D model.

Agisoft PhotoScan is a commercial product and, consequently, the actual algorithms are not well documented. However, there is some general information available about the processes behind SfM that are used in Agisoft PhotoScan (*Figure 2.10*). The first step in the SfM algorithm is feature detection. During this step, identical features, within each photograph are identified regardless of scale or angle (*Fonstad et al., 2013*). This can be done by Scale Invariant Feature Transform (SIFT). These identified features are matched between the imagery. A threshold is used because not each feature will be in every photograph. Incorrect matches are filtered by determining the correspondence between imagery (*Smith et al., 2015*). It is important that the imagery has enough overlap. The overlap must be at least 60% but preferable is around 80%. To estimate the location where the photograph was taken in a 3D scene and to estimate the intrinsic and extrinsic camera poses, an algorithm similar to Bundler is used (*Westoby et al., 2012*). This algorithm uses the abundance of different imagery and camera angles. This results in an unscaled 3D model which can be geo-referenced with GCPs. Furthermore, the camera parameters can

be refined with the location information set by the GCPs. The final step is to use Multi-View Stereo (MVS) algorithms to increase the point cloud density by letting more pixel of an image produce a point (*Javernick et al., 2014*).

2.4.2 General workflow

Every processing step for Agisoft PhotoScan is documented in a workflow diagram (*Figure 2.12*). The workflow is divided into three main parts: preparations, processing and exporting.

2.4.2.1 *Preparations*

The input for Agisoft PhotoScan consists of the set of individual UAV acquired imagery and coordinate data of the markers. Only good quality imagery can be used. Accordingly, imagery that was either blurred or not perpendicular to the ground were removed from the datasets. The model will be given a coordinate system that is identical to the GCPs dataset. In this case the coordinate system is WGS 1984. If lens, measurement accuracy, location and orientation parameters of the imagery are available, these parameters are added to the model. For this research these parameters were not available and, therefore, estimated by Agisoft PhotoScan.

DPGS measured locations were used as input in Agisoft PhotoScan. The DGPS measured location of the markers must be matched with the corresponding markers on each photograph (*Figure 2.11*). After processing three of the forty markers, the other locations of the markers will be estimated. These estimated locations need to be moved manually to the centre of the markers. The matching of markers in the imagery is the most important part to obtain a correct OrthoMosaic or OrthoDEM. If errors occur in this step, each following processing step will contain the same erroneous information.

Figure 2.11 Part of a photograph for the La Bâtie-Montsaléon site. Two markers visible on a photograph have been matched with their actual DGPS coordinates. This is shown by the green flag on the marker.

2.4.2.2 *Agisoft PhotoScan*

The SfM algorithm produces a 3D model that can be used to export an OrthoDEM and OrthoMosaic. The photos were aligned with the highest accuracy settings available but without pre-selection as location data was not available. The default key points (40000) and tie points (1000) were used to obtain a sparse point cloud. Incorrect points were removed from the sparse point cloud with the tool called gradual selection or by manually deleting these points. The sparse cloud was automatically scaled up, with some mild height

filtering, to a dense point cloud of high quality. The height filtering is mild because otherwise this could remove important details such as subtle riverbed elevation variations out of the model.

A 3D height model (mesh) was derived based on the dense point cloud with triangulation. Gaps in the model were interpolated. A 3D height model has only one Z-coordinate for every XY-coordinate. This improves processing time and removes all floating artefacts. The number of faces and vertices determines the details that are visible in the model. The vertex colours and vertex normals were derived from the imagery to texture the mesh.

2.4.2.3 *Exporting results*

After processing, a 3D height model is obtained. This derived 3D height model is geometrically corrected and contains elevation data. Consequently, can be exported as an OrthoDEM. This is a Digital Surface Model (DSM) as it depicts the height of the surface, vegetation and buildings. In addition, the 3D height model imagery can be exported as OrthoMosaic. Here, the photographs are blended across the mesh. As these datasets are located in UTM Zone 31N, the coordinate system WGS 1984 UTM Zone 31N was used.
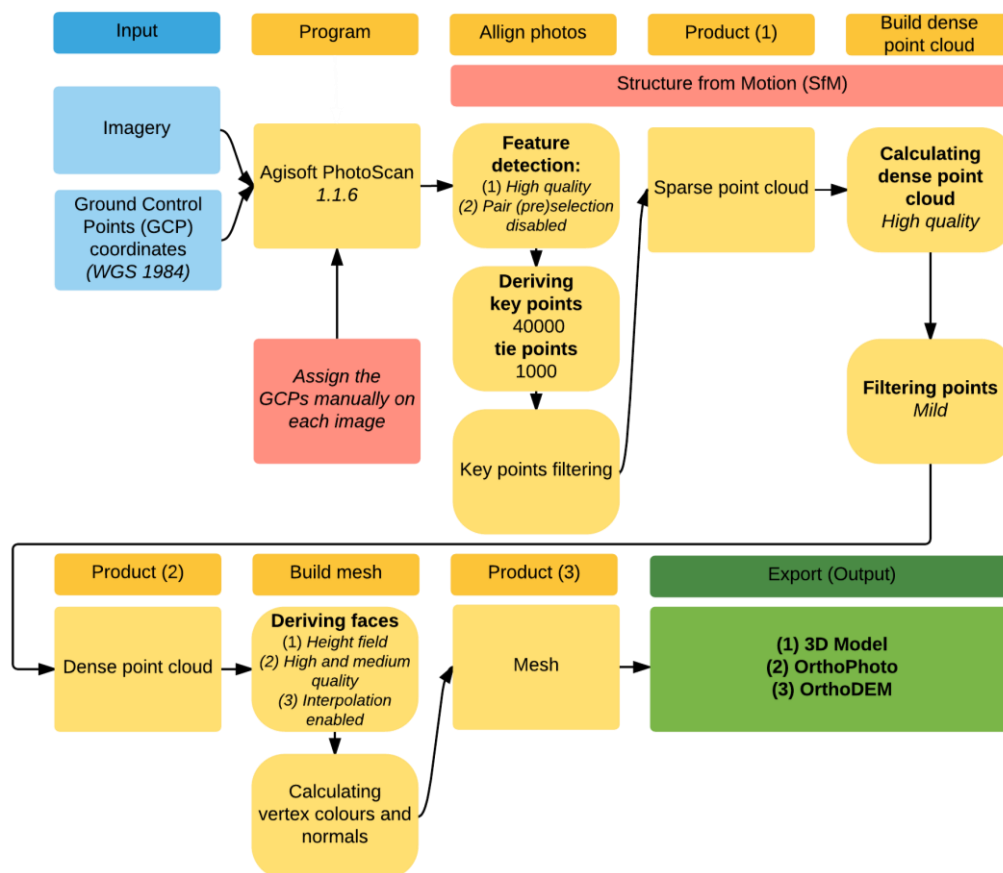
Figure 2.12 Flowchart that describes the entire workflow. It is divided into three parts starting with the pre-processing of the imagery and GCPs, the processing with the SfM algorithm (alignment, building point clouds and deriving meshes) in the Agisoft PhotoScan software and the resulting products (OrthoMosaic and OrthoDEM).

2.5 Method of analysing

The calculated products such as 3D models, OrthoMosaics and OrthoDEMs will be qualitatively described. With an accuracy analysis it is determined and evaluated how the OrthoMosaics and OrthoDEMs of 2014 and 2015 relate with the DPGS measurements which answers the technical part of the research question. Next to that, channel displacements and bank erosion sites were analysed to obtain more information about the river dynamics, answering the second morphological research question.

2.5.1 Positional accuracy analysis

Agisoft PhotoScan exported products are OrthoMosaics and OrthoDEMs. These products of 2014 and 2015 have the coordinate system WGS 1984 UTM Zone 31N that is based on the DGPS location information of the markers visible in the photographs. Markers are also visible on the OrthoMosaic. The location of the markers that were visible in the OrthoMosaic are slightly different than the location that was measured with the DGPS. The location of the markers on the OrthoMosaic can be exported. Similar, at the same locations the elevation can be extracted from the OrthoDEM. This creates a point based dataset with the modelled location of the markers on the OrthoMosaic which then can be compared with the original marker location of the DGPS measurements.

When two marker locations are compared it will result in a Euclidian distance (near distance) value. This is the difference in the combined XY-direction and a difference in Z-direction. The XY-direction can only contain positive values as it is the distance. The Z-direction can have either a negative difference or a positive difference. As XY-directions are combined, the angle between modelled and original DGPS measurements can be calculated (*Figure 2.13*). The orientation of the uncertainty provides information whether the dataset was correctly acquired. When the orientation is random, it shows that the entire research area was covered from all angles. Otherwise, the errors generally have the same direction.
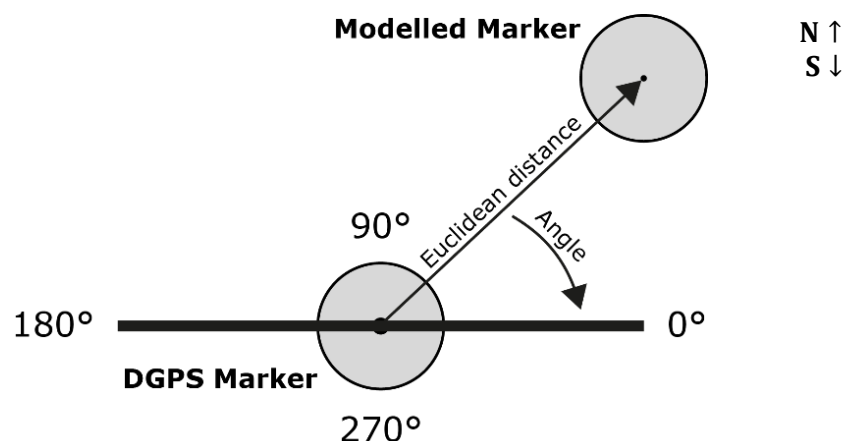
Figure 2.13 Visual explanation of Euclidean distance and angle between modelled marker location and marker location measured with the DGPS.

There are also a couple of independent DGPS measurement made in 2015 at bank erosion sites. These measurements are taken on above (top of the bank edge) and below (at the water edge) the river bank. Therefore, the OrthoDEMs elevation can be validated with an independent measurement.

2.5.2 Qualitative description

At each research location alongside the Buëch, characteristics and notable geomorphological features are qualitatively described. The river description will include the older datasets that could not be geo-referenced and not be quantified due to missing marker DGPS points. For these datasets, a qualitative description is the only method to include information. This description is based on the OrthoMosaics and the underlying OrthoDEMs. Furthermore, prominent differences between certain years will be highlighted. A reference grid will be used to pinpoint locations of interest such as river banks, bifurcations and locations with erosion.

2.5.3 Quantifying channel displacements

The OrthoMosaics of the 2014 and 2015 datasets were accurately geo-referenced and consequently could be compared to study river morphology dynamics. The channels will be manually mapped with a graphic editor using neighbouring cell information. The river channel is greenish while the surrounding river banks are white. A pixel within the channel will be compared with the neighbouring pixel. If the pixels have a similar colour they will be selected. By doing this for the entire channel, all pixels will be selected up until the edge of the river banks. A shapefile for the channels can then be exported. Separate shapefiles are made 2014 and 2015. Key locations will be selected where the channel displacements (*Figure 2.14*) can be analysed and quantified.
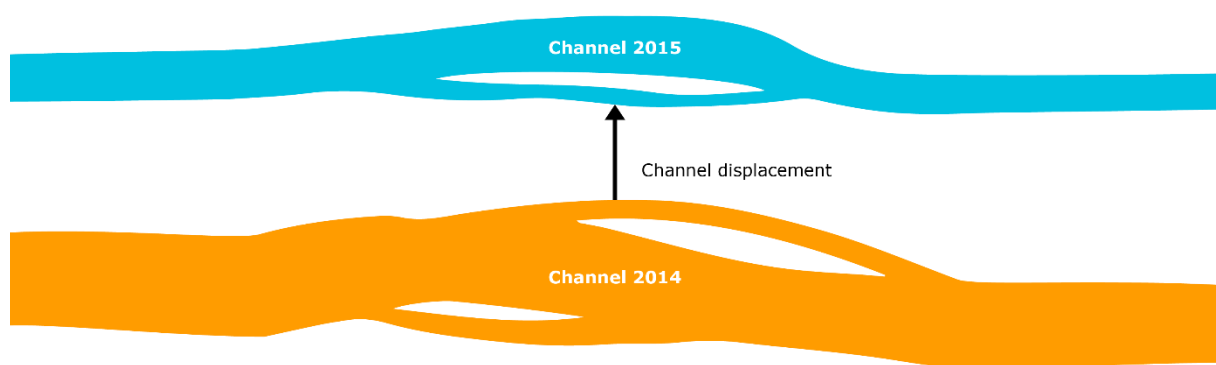
Figure 2.14 Abstract view of channel displacements between 2014 and 2015.

2.5.4 Quantifying bank erosion

The river bank has a higher elevation and, therefore, the location can be derived from elevation data. In addition, the location can be derived by determining the channel location within the OrthoMosaic. Geo-referenced OrthoDEMs of La Bâtie-Montsaléon and Chabestan of the 2014 and 2015 datasets will be used to create multiple cross sections from one side of the channel to the bank erosion site. The elevation information is plotted and the difference in location of the bank between 2014 and 2015 is measured (*Figure 2.15*). Consequently, this will give information about the activity of measured bank erosion sites.

Figure 2.15 Abstract view of bank erosion between 2014 and 2015.

2.5.5 Quantifying volume

A significant erosion site at La Bâtie-Montsaléon was selected to look at the amount of erosion that took place between 2014 and 2015. Two geo-referenced OrthoDEMs are used to calculate the volume. For each pixel in the erosion site the difference between 2014 and 2015 is calculated. The location of the erosion site in 2014 was covered with vegetation and consequently the height was extrapolated from a nearby clear bank. In 2015 there was no vegetation and thus the elevation corresponds with ground level. After the difference of the elevation data (height) is calculated, it is multiplied with the cell size (length and width) to get a volume in cubic meters (*Figure 2.16*).
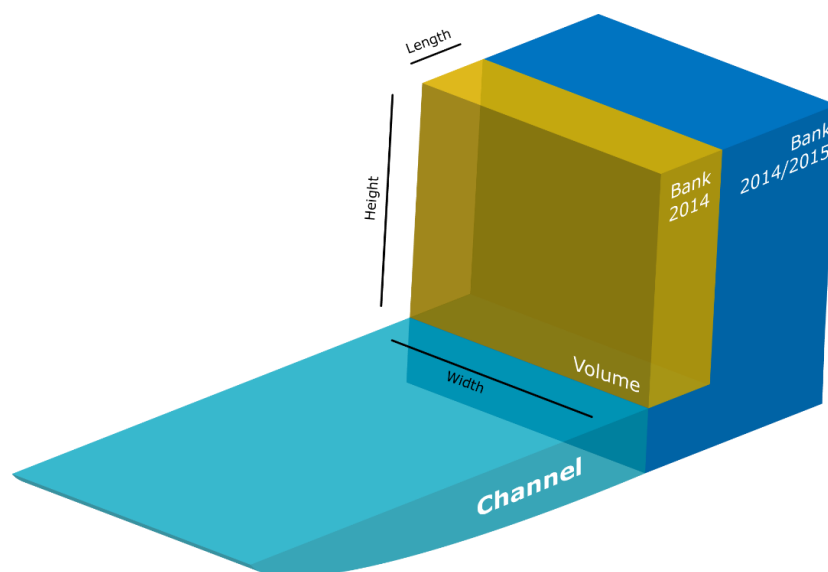
Figure 2.16 Abstract view of how to calculate a volume on different erosion sites. The orange part is eroded between 2014 and 2015.

3 Results

This chapter will present the results with respect to the two research questions and contains an accuracy analysis, descriptions of the river for each year, quantification of channel displacements, bank erosion and erosion volumes. The OrthoMosaic and OrthoDEM for each dataset matches correctly with the IGN OrthoMosaic of the research area at fixed location such as bridges and roads. The resolution of the OrthoMosaics are approximately 2.6 cm and the resolution of the OrthoDEMs are approximately 5.7 cm. Each geo-referenced dataset has after processing an Agisoft PhotoScan Report (*Addendum A*). This report contains information about the processing details, the used parameters, the number of matches, marker locations and errors.

3.1 Positional accuracy analysis 2014 and 2015

For both years 2014 and 2015 and for all three research locations, statistics and boxplots were computed. The boxplots with statistics are based on all markers and illustrate the difference in meters between the original location of the marker measured with the DGPS with the modelled location of the marker in the OrthoMosaic.

3.1.1 Statistics 2015

For each of the three research locations, the results are comparable. The Euclidean distance (XY-direction) varies between 2 cm up to 70 cm, while the Z-direction is between -10 cm and +10 cm. The distribution of errors for the Z-direction for all research locations are narrow and around zero, which indicates a high accuracy. The opposite applies for the Euclidean distance. The distribution of errors is broad, indicating a lower accuracy (*Figure 3.1*).
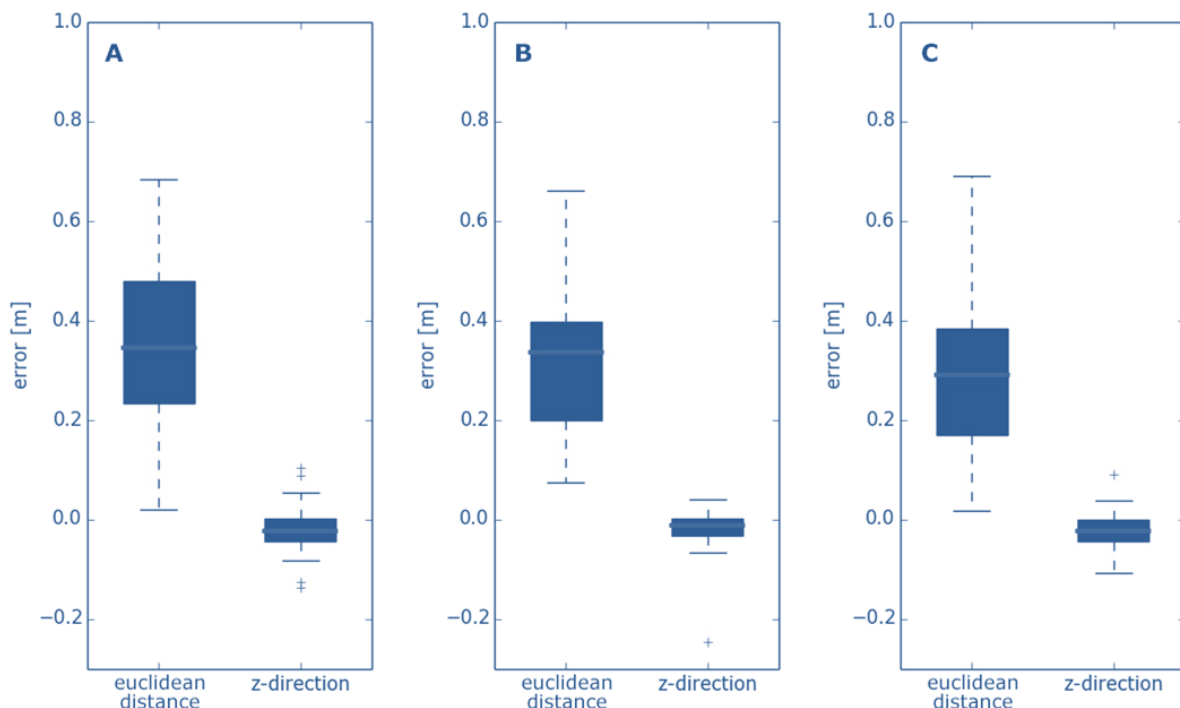
Figure 3.1 Boxplots for the three research locations in 2015: (A) Chabestan, (B) La Bâtie-Montsaléon and (C) Serres. The outliers are visible as a 'plus' sign.

According to calculated statistics (*Table 3.1* and *Table 3.2*), Serres is the most accurate dataset with an average error in the Euclidean distance of 28 cm. The less accurate dataset based on the Euclidean distance is Chabestan. This dataset has an accuracy of 35 cm. The most accurate in the Z-direction is Chabestan with an average 2.0 cm mismatch. The other locations have only a 3 mm difference compared with Chabestan. La Bâtie-Montsaléon dataset has uncertainties that are between the values of Chabestan and Serres. There are a couple of outliers within the datasets showed by the large difference between median, maximum and minimum values. It can be concluded that all 2015 datasets have a fairly comparable accuracy. It can be concluded that Z-direction is very accurate but the Euclidean distance is not on that same level.

Table 3.1 Euclidean distance accuracy statistics for the three research locations in 2015.

Location	Mean (m)	Median (m)	Upper quartile (m)	Lower quartile (m)	Minimum (m)	Maximum (m)
Chabestan	0.3498	0.3448	0.4778	0.2328	0.0190	0.6821
La Bâtie-Montsaléon	0.3192	0.3347	0.3968	0.1978	0.0733	0.6609
Serres	0.2839	0.2902	0.3827	0.1690	0.0161	0.6899

Table 3.2 Z-direction accuracy statistics for the three research locations in 2015

Location	Mean (m)	Median (m)	Upper quartile (m)	Lower quartile (m)	Minimum (m)	Maximum (m)
Chabestan	-0.0196	-0.0240	0.0018	-0.0450	-0.1366	0.1042
La Bâtie-Montsaléon	-0.0201	-0.0132	0.0012	-0.0328	-0.2473	0.0396
Serres	-0.0222	-0.0249	-0.0014	-0.0441	-0.1075	0.0892

3.1.2 Statistics 2014

For the 2014 datasets, the Euclidean distance varies between 6 cm up to 2 m, while the Z-direction varies between -11 cm and +12 cm. The data includes more outliers than the 2015 dataset as the maximum and minimum values are larger and sometimes even outside of the plot (*Figure 3.2*). A primary example is the maximum Euclidean distance of 2.1 m at Chabestan.

The boxplots for the Z-direction for all research locations are shorter than the boxplots for the Euclidean distance. This corresponds with a higher accuracy for the Z-direction then for the Euclidean distance. Compared with 2015, all the Euclidean distance

boxplots are shorter and so the uncertainty is smaller. The Z-direction is almost equally certain between 2014 and 2015 datasets.
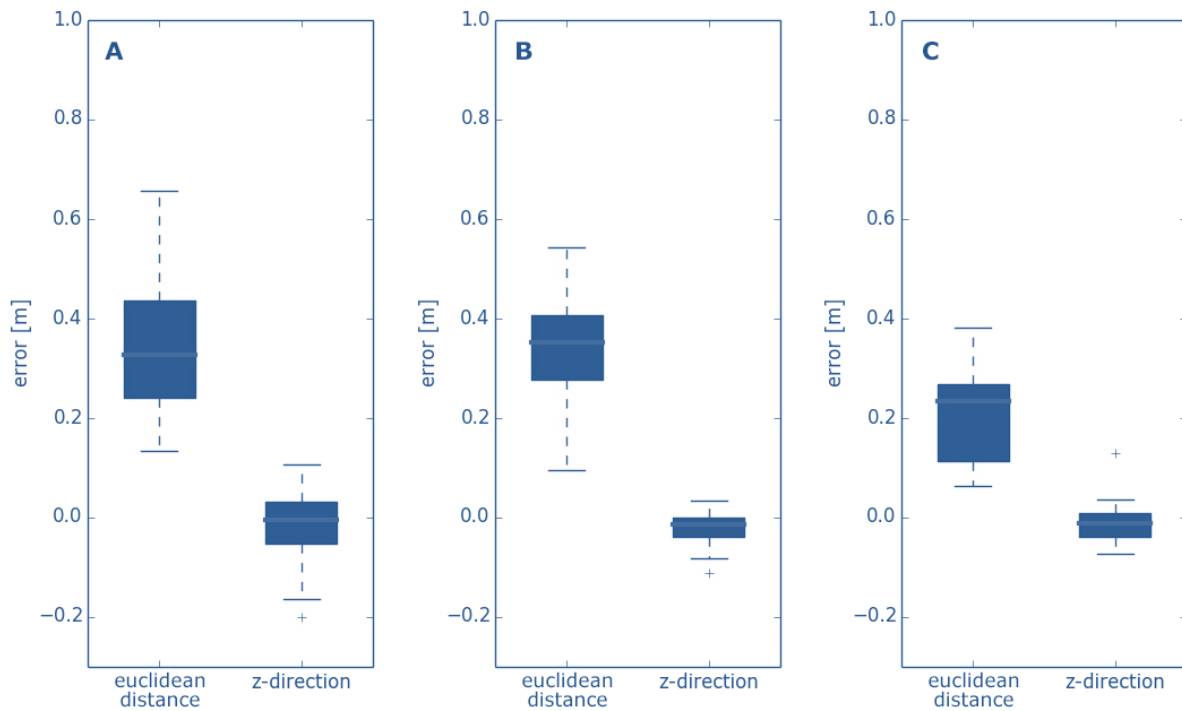
Figure 3.2 Boxplots for the three research locations in 2014: (A) Chabestan, (B) La Bâtie-Montsaléon and (C) Serres. The outliers are visible as a 'plus' sign.

As for 2014, the calculated statistics show (*Table 3.3* and *Table 3.4*) that Serres is the most accurate dataset in the Euclidean distance with an accuracy of 21 cm. Chabestan and La Bâtie-Montsaléon are the less accurate with an average accuracy of 39 cm and 33 cm respectively in the Euclidean distance. The Serres 2014 dataset is the most accurate in the Z-direction with an average accuracy of 0.8 cm. La Bâtie-Montsaléon and Chabestan are less accurate with an average accuracy of 2.1 cm and 1.9 cm in the Z-direction. Overall, the accuracy values are comparable between the research sites.

Table 3.3 Euclidean distance accuracy statistics for the three research locations in 2014.

Location	Mean (m)	Median (m)	Upper quartile (m)	Lower quartile (m)	Minimum (m)	Maximum (m)
Chabestan	0.3854	0.3266	0.4360	0.2397	0.1332	2.1187
La Bâtie-Montsaléon	0.3307	0.3501	0.4047	0.2755	0.0934	0.5410
Serres	0.2106	0.2321	0.2675	0.1115	0.0616	0.3808

Table 3.4 Z-direction accuracy statistics for the three research locations in 2014.

Location	Mean (m)	Median (m)	Upper quartile (m)	Lower quartile (m)	Minimum (m)	Maximum (m)
Chabestan	-0.0189	-0.0063	0.0308	-0.0544	-0.2007	0.1065
La Bâtie-Montsaléon	-0.0218	-0.0158	-0.0005	-0.0400	-0.1129	0.0332
Serres	-0.0084	-0.0136	0.0068	-0.0391	-0.0748	0.1280

3.1.3 Magnitude and size distribution

The angle of the error between the DGPS measured marker and the modelled marker is random in each dataset. Additionally, the magnitude is random across the research areas. For example, at Chabestan 2014 and Serres 2015 (*Figure 3.3*) there is no increasing trend in uncertainty close by moving vegetation by wind or running water.
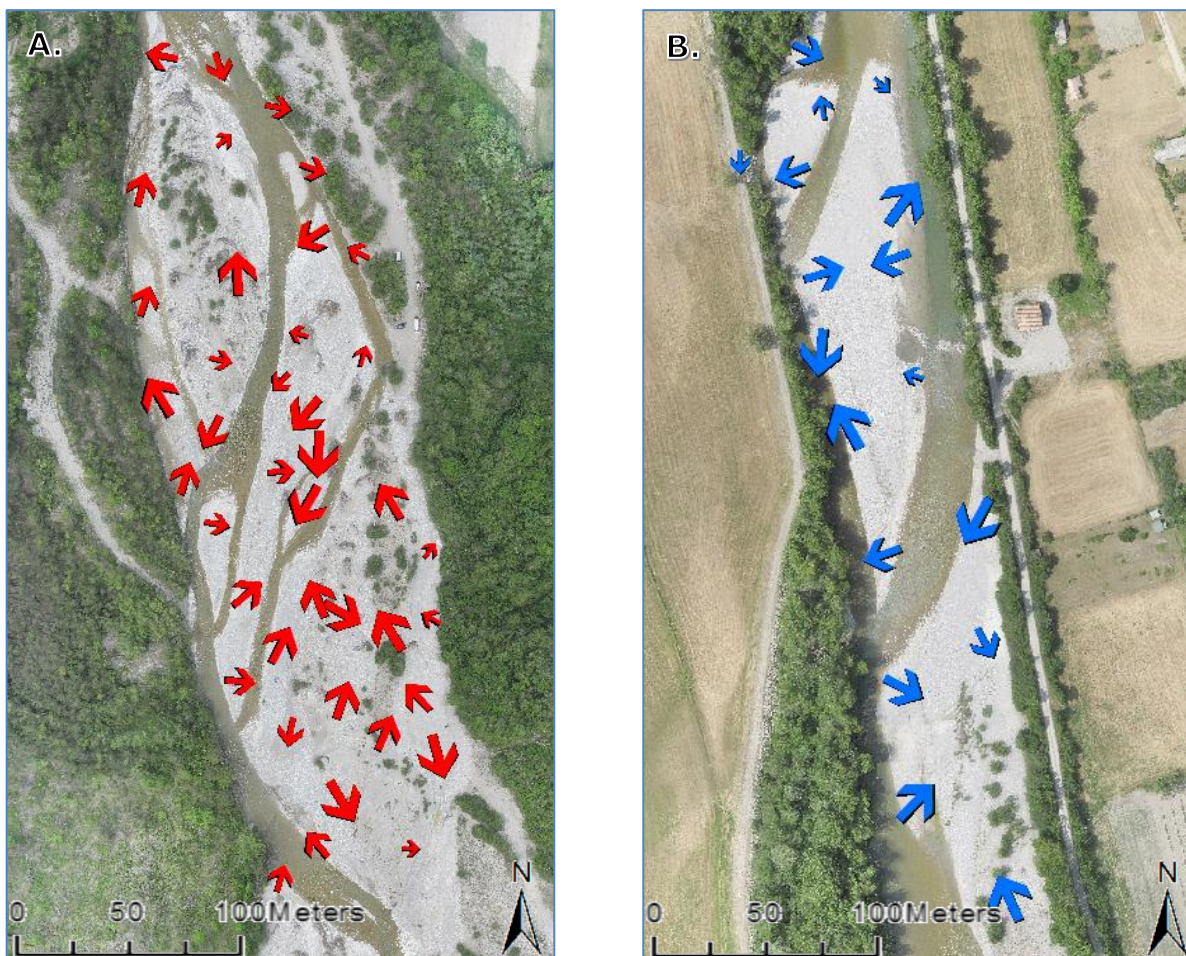
Figure 3.3 (A) Chabestan 2014. (B) Serres 2015. Direction of the arrow is the orientation and the size of the arrow is the Euclidean distance (*Figure 2.13*). The arrow size is multiplied by a factor to enhance visibility and consequently the Euclidian distance is exaggerated in this figure.

3.1.4 Independent DGPS measurements

Extra DGPS measurements at the top at the edge and below at the foot of the bank erosion site were not included in the calculations in the model for Agisoft PhotoScan (*Figure 3.4*). There were no markers associated with these independent DGPS measurement.
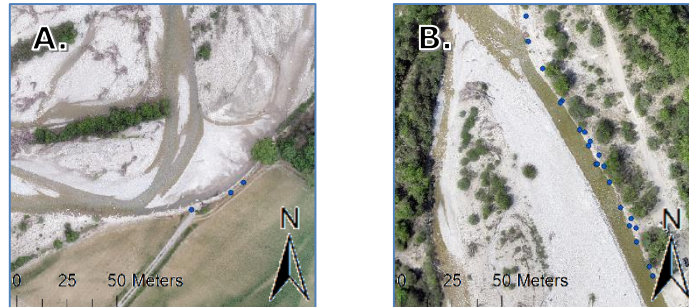
Figure 3.4 Location of the DGPS measurement indicated as points at bank erosion sites at (A) La Bâtie-Montsaléon and (B) Chabestan.

Only elevation differences were compared and differences in XY-direction were not taken into account as the exact measurement location could not be determined due to lack of markers and blurry edges. The mismatch between the DGPS measurement, taken at the edge or at the foot of the bank and the DSM, varies (*Table 3.5* and *Figure 3.5*). The largest difference (-7.381 m and -2.138 m) are caused by overhanging vegetation. In general, the difference in DGPS measurements and DSM above the bank is smaller than the difference between the DGPS measurements and DSM below the bank. The DGPS measurements coincides with DSM with an approximate error of 6 cm above the bank and 14.5 cm below the bank.

Table 3.5 Difference between measured DGPS elevation and elevation DSM above and below the river bank for Chabestan and La Bâtie-Montsaléon.

Edge above bank (in m)		Chabestan	Edge below bank (in m)		Chabestan
DGPS	*DSM*	*Difference*	*DGPS*	*DSM*	*Difference*
775.922	776.035	-0.113	774.035	774.048	-0.013
776.009	776.062	-0.053	774.081	781.462	-7.381
775.631	775.701	-0.070	774.081	774.099	-0.018
776.628	776.545	0.083	774.156	774.241	-0.085
776.623	776.545	0.078	774.081	774.415	-0.334
776.350	776.365	-0.015	774.292	774.493	-0.201
776.191	776.164	0.027	774.426	774.314	0.112
776.261	776.274	-0.013	774.383	774.484	-0.101
776.147	778.285	-2.138	774.486	774.553	-0.067
775.854	775.809	0.045	774.569	774.997	-0.428
775.764	775.773	-0.009	774.581	774.675	-0.094
Edge above bank (in m)		Chabestan			
DGPS	*DSM*	*Difference*			
751.962	751.182	0.780			
751.565	751.520	0.045			
751.703	751.702	0.001			
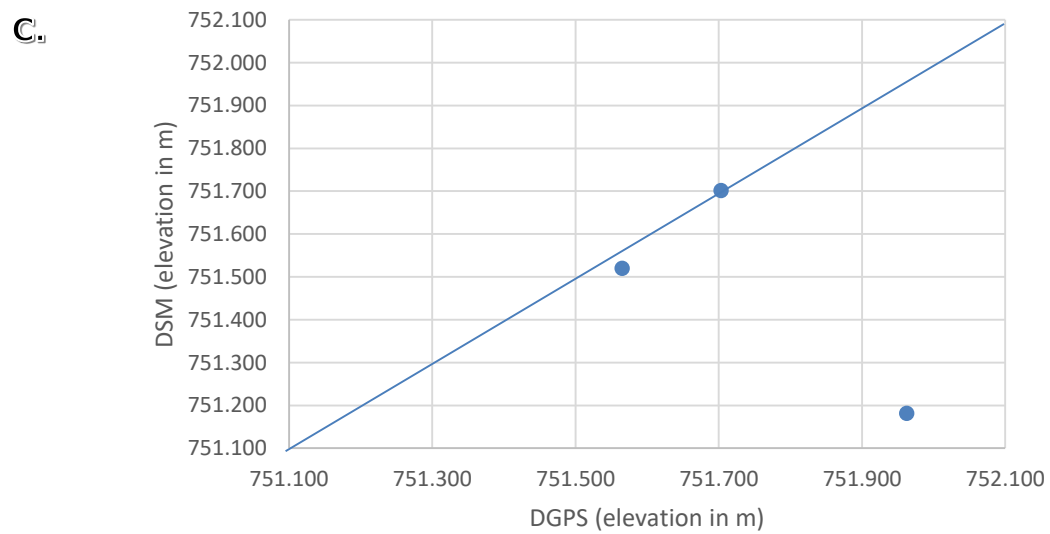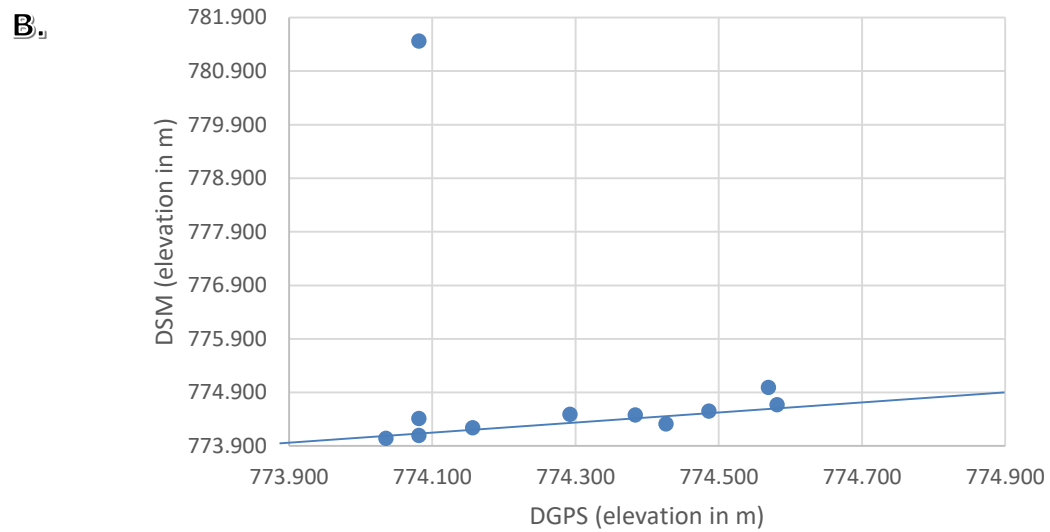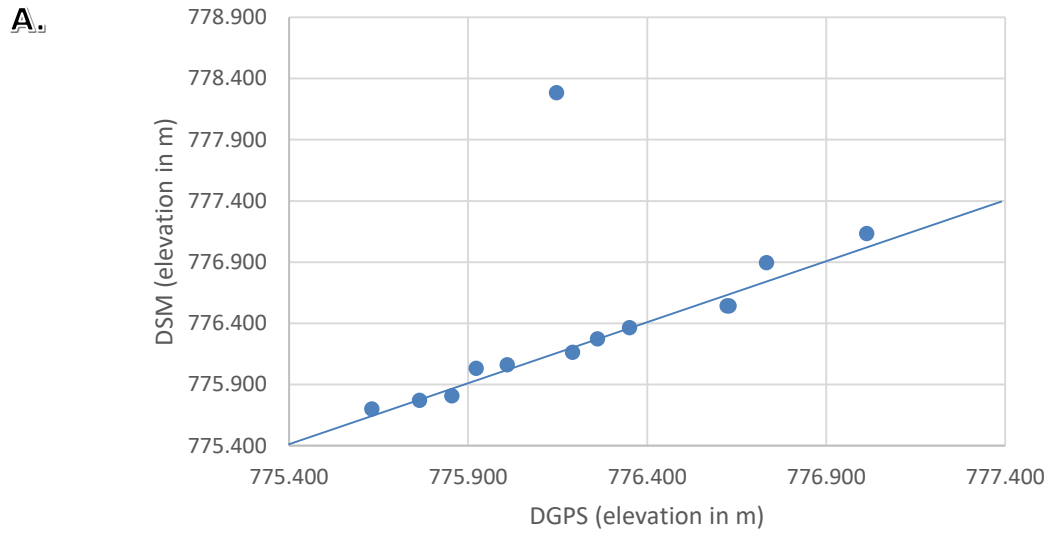
Figure 3.5 Elevation DGPS measurement plotted with elevation DSM for (A) Top of bank Chabestan, (B) foot of bank at Chabestan and (C) top of bank La Bâtie-Montsaléon. The 1:1 line indicate the difference between observed elevation and modelled elevation.

3.2 River description

River channel position is qualitatively described based on the corresponding OrthoMosaic for each available year and for each of the three locations. Additional data that is used in the analysis is the DSM. The sites are analysed from the most upstream part of the research location to the downstream part of the research location and afterwards compared with the older datasets. A reference grid is used to identify which part of the datasets is described.

3.2.1 Chabestan

The Chabestan dataset includes the years 2013, 2014 and 2015 covering a maximum upstream-downstream distance of approximately 1000 m. This part of the Buëch is described starting from the upstream direction (north) towards to downstream direction (south).

3.2.1.1 *Chabestan 2015*

At Chabestan (*Figure 3.6*), there was a low discharge during image acquisition and, as a result, there are many dry banks enhancing the visibility of geomorphological features.

Upstream, there is only one channel as the Buëch passes under a bridge (just outside of the area). When the river plain starts to widen, the Buëch splits up in a large main channel (mainly C2) and a secondary channel (mainly B2) that has a lower discharge. In the middle, a large river bank is situated (B2 and C2). These channels flow alongside the river embankment. The main channel starts with rapids (increase of flow velocity) when the channel becomes narrower and the flow is affected by large boulders. It continues alongside the eastern side by a natural vegetated river embankment, causing bank erosion until the channel narrows and rapids occur for the second time. The secondary channel (B2) flows at the western side and splits up and joins again multiples time. The main channel continues to flow more towards the middle of the river plain until it coincides again (C3).

The river bank was eroded by channels that are presently not active (B2 and C2). Older channels can be distinguished crossing from the eastern to the western side. In the upper left part of the river bank alongside the smaller secondary channel separate trees are visible. Adjacent to the main channel, there is no vegetation. The lower part of this river bank contains a few scattered trees alongside the main channel. Here, the river flows towards the outer band as a single channel up to the most downstream part of the study area (A4). The main channel in general has meandering characteristics. Vegetation is present as patches with small shrubbery or trees (B4 and C1). There is a patch with older trees but it is cut off from the embankment (B3). On many locations tree remains are

deposited. The tree remains might still have leaves depending on passed time. There are no agricultural fields directly next to the river as the entire river bank is covered by trees.

Figure 3.6 UAV based OrthoMosaic located at Chabestan acquired in 2015. The Buëch flows in north-south direction and has multiple active channels. The river banks alongside the Buëch are covered with trees.

3.2.1.2 *Chabestan 2013 and 2014*

By comparing the mosaic of 2013 with OrthoMosaic of 2014 and 2015 (*Figure 3.7*), it is apparent that two active channels merged (B2 and C2). The main channel is situated approximately at the same locations and there is no clear indication that large patches of vegetation are eroded. Determining exactly the changes between the years is difficult as the 2013 dataset is not georeferenced and uses a local coordinate system.

The channels cross from the east side of the river plain to the west side of the river plain at the same location (B2) in 2013 and 2014. In 2015, the channel abandoned this area and moved towards to eastern edge of the river plain. It appears that in 2013 the discharge conditions were higher as the water is more turbid and channels are fuller. This will influence the number of active channels. In 2013 and 2014, the channel has mainly a meandering characteristic. However, at every time there are multiple channels active so the channel can also be identified as braided.

In both datasets, many obstructions like tree stumps are visible within the imagery. Tree remains are deposited on river banks, especially at the downstream part (2013 and 2014 B3). This illustrate the active erosion of the upstream river banks of the Buëch.

Figure 3.7 (A) UAV based OrthoMosaic located in Chabestan acquired in 2014, in the same frame as the 2015 dataset. (B) UAV based mosaic located in Chabestan acquired in 2013 (without coordinates).

3.2.2 La Bâtie-Montsaléon

La Bâtie-Montsaléon has the largest time series compared with Chabestan and Serres. The La Bâtie-Montsaléon dataset includes the years 2002, 2010, 2011, 2014 and 2015. The flow direction of the Buëch is east to west at La Bâtie-Montsaléon in contrast to north to south at Chabestan. At La Bâtie-Montsaléon, the UAV mosaic covers an area of approximately 1000 m along the river. This will be described starting at the eastern side, where a bridge is located, to the middle, where a tarred agricultural road was located, and ends towards the western side, where there are no recognisable landmarks.

3.2.2.1 *La Bâtie-Montsaléon 2015*

At La Bâtie-Montsaléon (*Figure 3.8*) discharge conditions were still favourable for analysing geomorphological features as the discharge was low.

Near the bridge, the channel can be described as a single main channel. However, there are some small river banks in the middle (D2). The inner bank contains coarser materials. One of the agricultural lots is located directly north of the Buëch in the outer bend (C1). In the outer bend, the channel splits up (B2). This results in a main channel that has meandering characteristics and a smaller channel. There is a river bank between these two channels. The active channels join together (B3) and afterwards get a braided pattern with multiple active channels until all the channels join into a single channel (A3) at the edge of the image. Some smaller, presently not active, river channels are noticeable in the river. However, there are no clear deposits visible that suggest that the main channel recently drastically changed its course.

A road was located between the agricultural lots (between D2-C2-B3-A4). However, due to bank erosion, this road has been collapsed (C3). Some parts of the agricultural field are as well eroded away. At the other side of the river (B2), erosion is only partly visible as vegetation keeps obstructing the view and is likely to stabilise the banks. The agricultural field (C1) has also high probability to experience erosion during high discharges. North of the Buëch (B1 and C1) is a railway track located. This track may be subject to erosion in the coming years if no counter-measures are taken. North of the tarred agricultural road (C2), there is vegetation that consists of trees and shrubbery. This part is likely flooded during high discharge and a river channel without vegetation can be seen between the two large vegetation patches (C2). Some small longitudinal vegetation patches are scattered throughout the middle of the river (B3). Single trees and younger shrubbery are located in the southwestern bank next to some agricultural lots (B3 and A3). Logs and tree stumps are found everywhere in the river but especially grouped together as these tree remains block the river flow, trap the passing trees and sediment. In the agricultural field (B3 and C2), humidity differences are apparent in the grass.
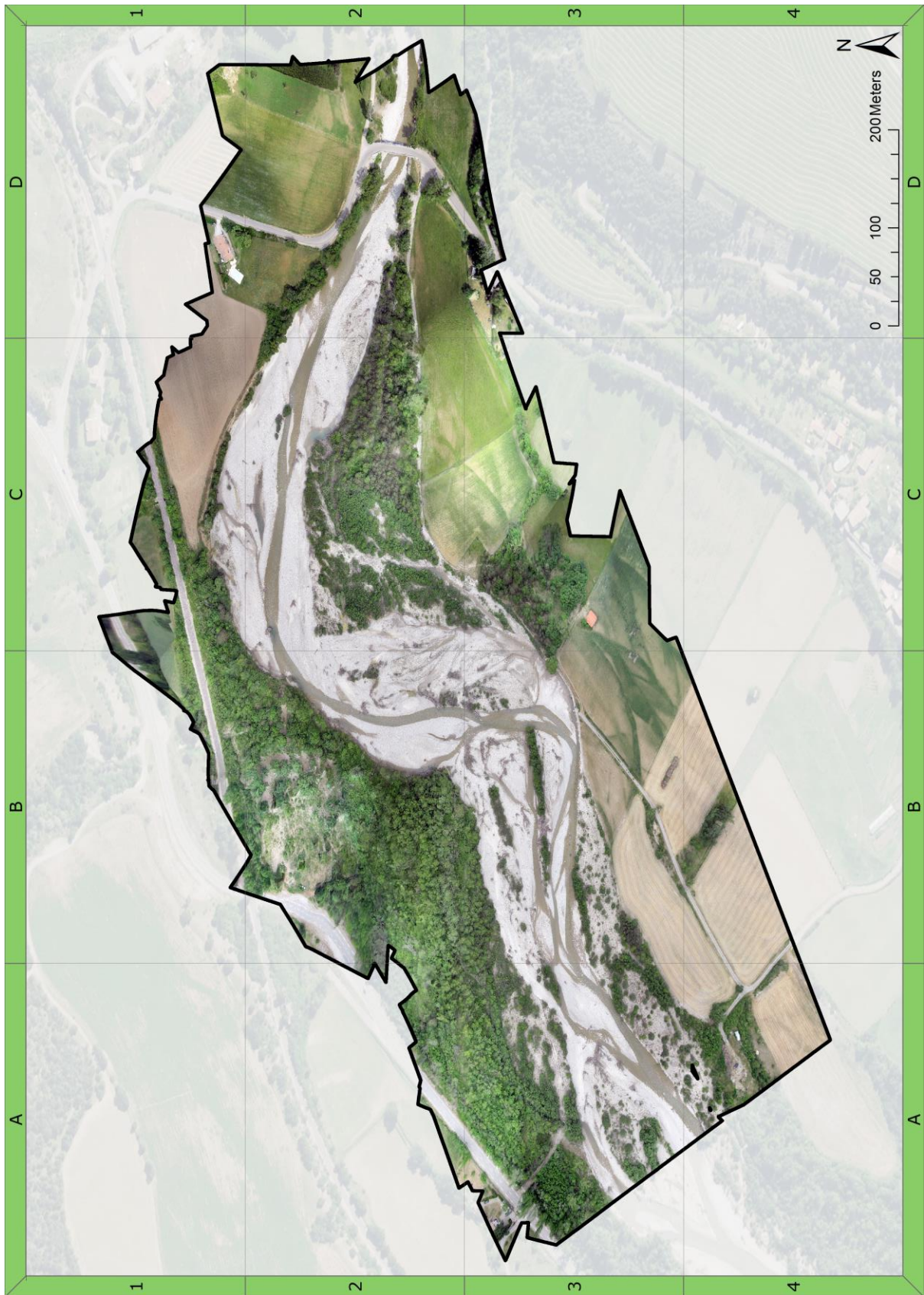
Figure 3.8 UAV based OrthoMosaic at La Bâtie-Montsaléon acquired in 2015. Agriculture is directly alongside the river at locations where that have experienced erosion. The other river banks next to the river are covered with trees. The Buëch meanders with multiple active channels.

3.2.2.2 *La Bâtie-Montsaléon 2002, 2010 and 2014*

Comparison of the mosaics of 2002/2010 with the OrthoMosaics of 2014/2015 (*Figure 3.7*) reveals that this is an area with many geomorphological changes between the years. The dataset of 2002 is interesting as in this dataset there was still a road (2002 - C3) next to the river. In 2010, the road is eroded (2010 - B3). Between the years, the meanders belts expanded and eroded the banks. In addition, vegetation started to grow between 2010 (B2/3) and 2014 (C2). The related time series show that every agricultural field near the river may be prone to erosion (2014 – C1/B3/C3). Between 2014 and 2015, at least one high discharge event occurred as a large part of forest eroded. This erosion site has a length of approximately 150 m and a maximum width of approximately 40 m.
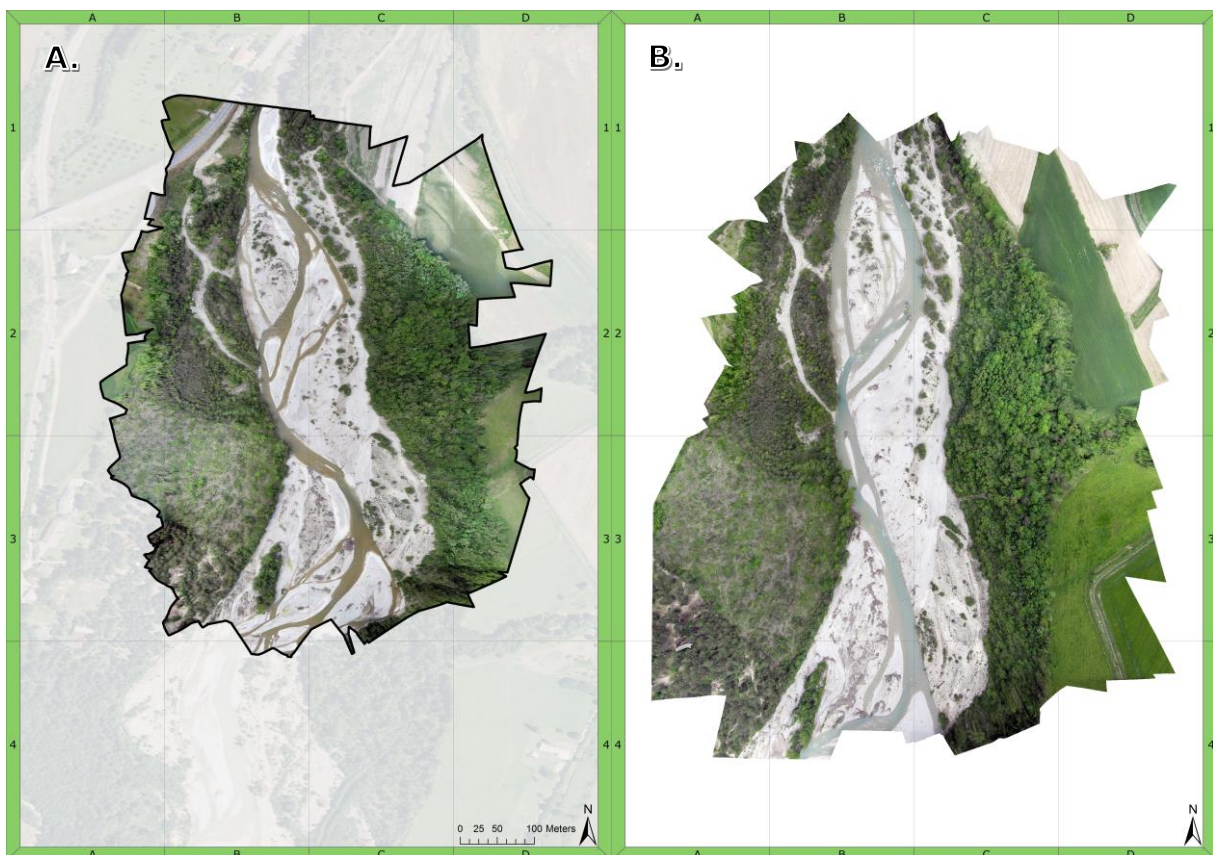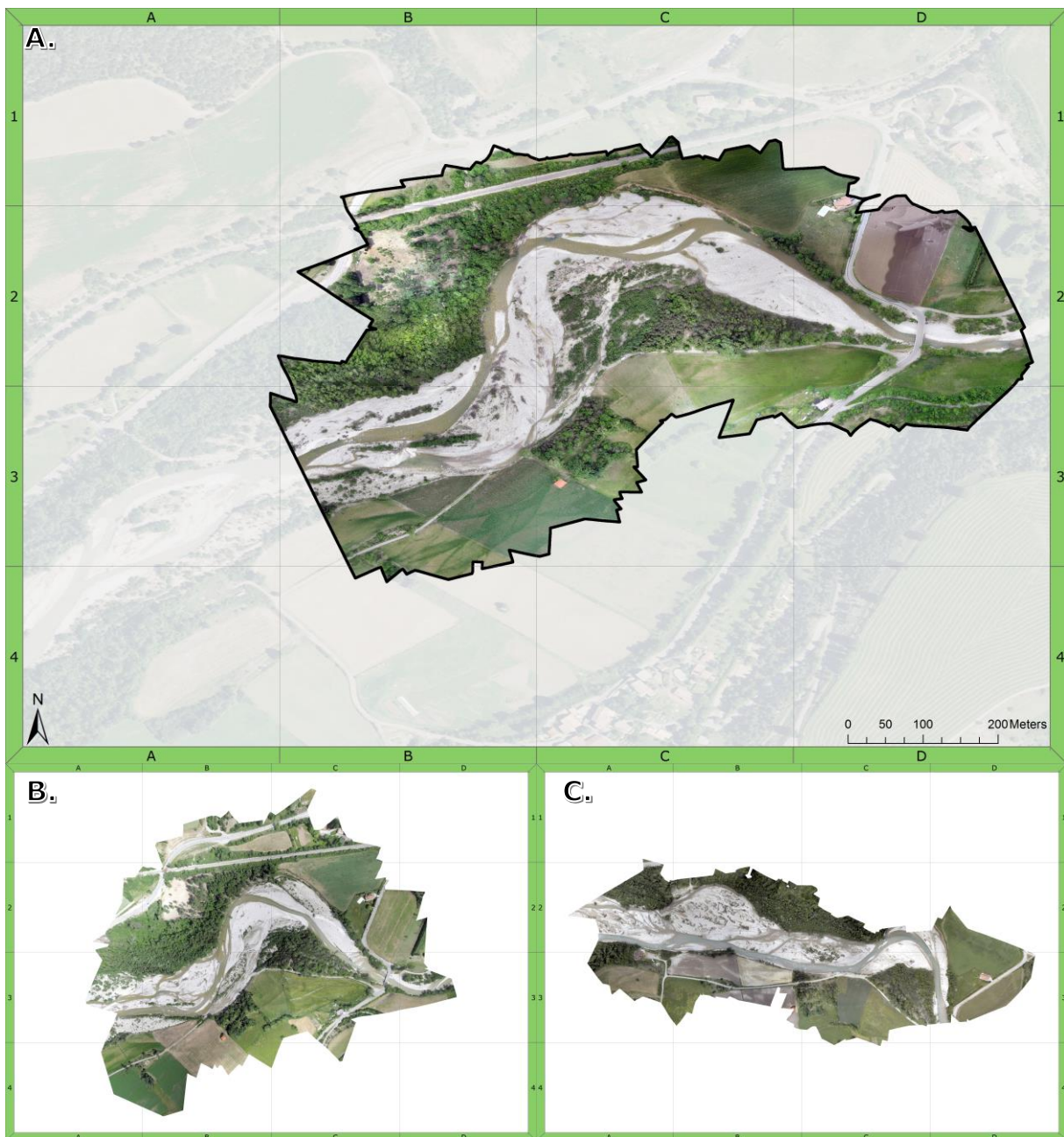

Figure 3.9 (A) UAV based OrthoMosaic of La Bâtie-Montsaléon acquired in 2014, in the same frame as the 2015 dataset. (B) UAV based mosaic of La Bâtie-Montsaléon acquired in 2010 (without coordinates). (C) UAV based mosaic of La Bâtie-Montsaléon acquired in 2002 (without coordinates).

3.2.3 Serres

Serres is the smallest dataset as only two years of data are available. The Buëch is flowing here from the north to the south. Just beyond the covered area, there is the Saint-Sauveur Dam. The distance covered by the UAV mosaic is approximately 900 m alongside the Buëch. The qualitative river description will start upstream (north). Discharge conditions were low during image acquisition and hence again favourable for observing geomorphology.

3.2.3.1 *Serres 2015*

At Serres (*Figure 3.10A*), the Buëch has a narrow river plain at the start of this area (B1) as the embankments are fixed by concrete dykes. There is one main channel that sometimes splits up to form a secondary channel (B1 and B3). In between those channels there are some river banks (B2). Most river banks do not have any vegetation. Some ridges of older channels are visible within the banks (B2).

The river plain starts to widen when the Buëch becomes nearer to the Saint-Sauveur dam (B3). The channel continues to branch a couple of times until it reaches a small lake. This causes backwater effect: A thin layer of water is located above the banks. This sheet of water follows the direction of older channels upstream (C4 and D4). There is a larger river bank (B3 and C3) with vegetation, likely older than one year, that follows a longitudinal pattern.

The region around the Buëch is primarily used for agriculture such as orchards (C3) or grass fields. Next to the entire stretch of the Buëch, a row of trees is located. Old river terraces are located in this area (A2 and B3) that have a higher elevation than the surroundings. There are dykes constructed in this area. The river plain is influenced and organised by humans. The channel does not contain any obstructions such as tree remains. They are likely removed as they may do damage to the dam. Those obstructions are also not identified on the banks. This results in an increased flow velocity. In addition, the entire embankment is protected with boulders against erosion events. Roads are on the human made embankments. There are many small sites were gravel has been extracted by the local population or were water is drained to the river.

At the Chabestan and La Bâtie-Montsaléon, the Buëch behaves naturally with active channel displacements and bank erosion. In comparison, at Serres there is almost no natural geomorphological activity. This part of the Buëch is almost completely human controlled and consequently less suitable to study natural river dynamics.

3.2.3.2 *Serres 2014*

When comparing the OrthoMosaics of 2014 (*Figure 3.10B*) and 2015, it is clear that this area is controlled by humans as there are no geomorphological changes. Only the channel

locations are changed between the two years and consequently also the location of the river banks. Vegetation identified in 2015 also is visible in the 2014 dataset.
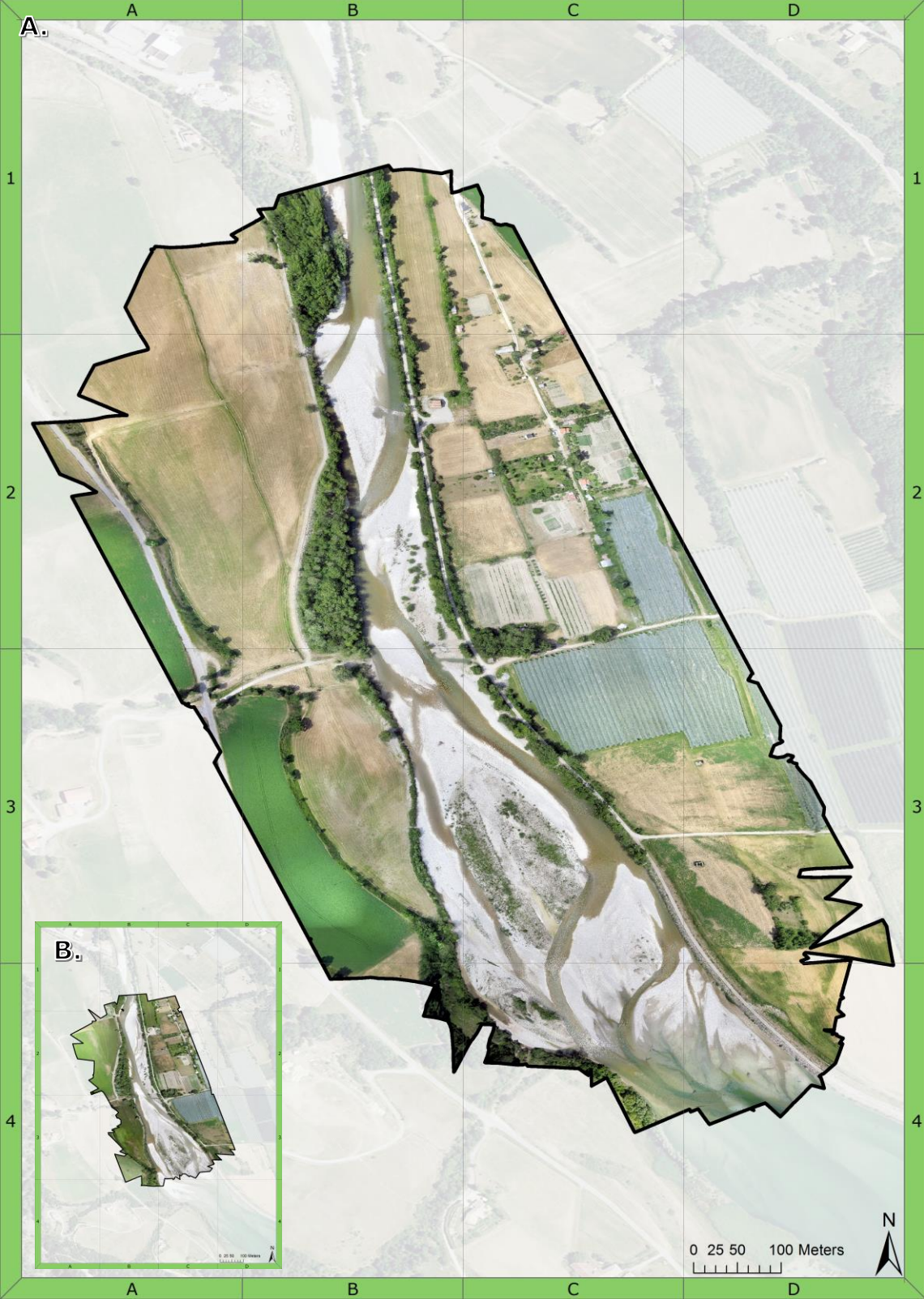
Figure 3.10 (A) UAV based OrthoMosaic of Serres acquired in 2015. (B) Picture in picture of UAV based OrthoMosaic of Serres acquired in 2014. The river banks are fixed in place. Alongside the Buëch there is primarily agriculture.

3.3 Channel and banks displacements

The Buëch is an active system with both erosion and accretion processes. This results in the displacements of channels over time. The data of 2014 and 2015 for each research location is geocoded and can consequently be visualised on top of each other. Each figure in this chapter shows the location of the channel belt in 2014 in red in 2015 in blue. The total area covered in the two datasets is different. Therefore, the area that was covered in 2014 and 2015 is visualised by a mask in blue and red respectively. Each complete map is added at the end of chapter 3.3 (*Figure 3.15*).

3.3.1 Channels displacements at Chabestan

For Chabestan, the most remarkable change between 2014 and 2015 is the number of active channels. In 2015, there is an active channel on both sides of the river plain. Though the channel on the right side is clearly the active channel as this channel is broader and field observations did show a higher discharge. In 2014, the active channels crossed the river plain dividing the large river bank.

In 2014, the channel could generally be classified as meandering with a high sinuosity. In 2015, the Buëch might still have a meandering pattern, however the sinuosity is lower and, therefore, the covered area is not sufficient to determine this with certainty. For both years the river has not a single channel but the channel has wandering tendencies.

Within a single year a large part of the area has changed. A large part of the main channel in 2015 was not active in 2014. The active channel in 2014, located in the middle of the river bank, is inactive in 2015. While on the left side in 2014 and 2015 there still is an active channel (*Figure 3.11*). For Chabestan, it is not clear how much the channels have eroded or moved within one year as the location of the main channel is completely different. In other words, no clear expanding features between the two years.

In 2014, the area had multiple river banks. Each river bank was divided by an active channel. The river bank was divided at locations where vegetation was absent. In 2015, when the channel became inactive, the largest river bank that has an active channel on every site was formed. In the rest of the area, due to changing active channels, smaller river banks between the two years have either emerged or disappeared.

If the water level increases, the first channels that will become active will be older channels (2014) as these channels might not be filled up and consequently have a lower elevation than the surrounding river banks. If the water level increases even more, bank full discharge conditions will occur.
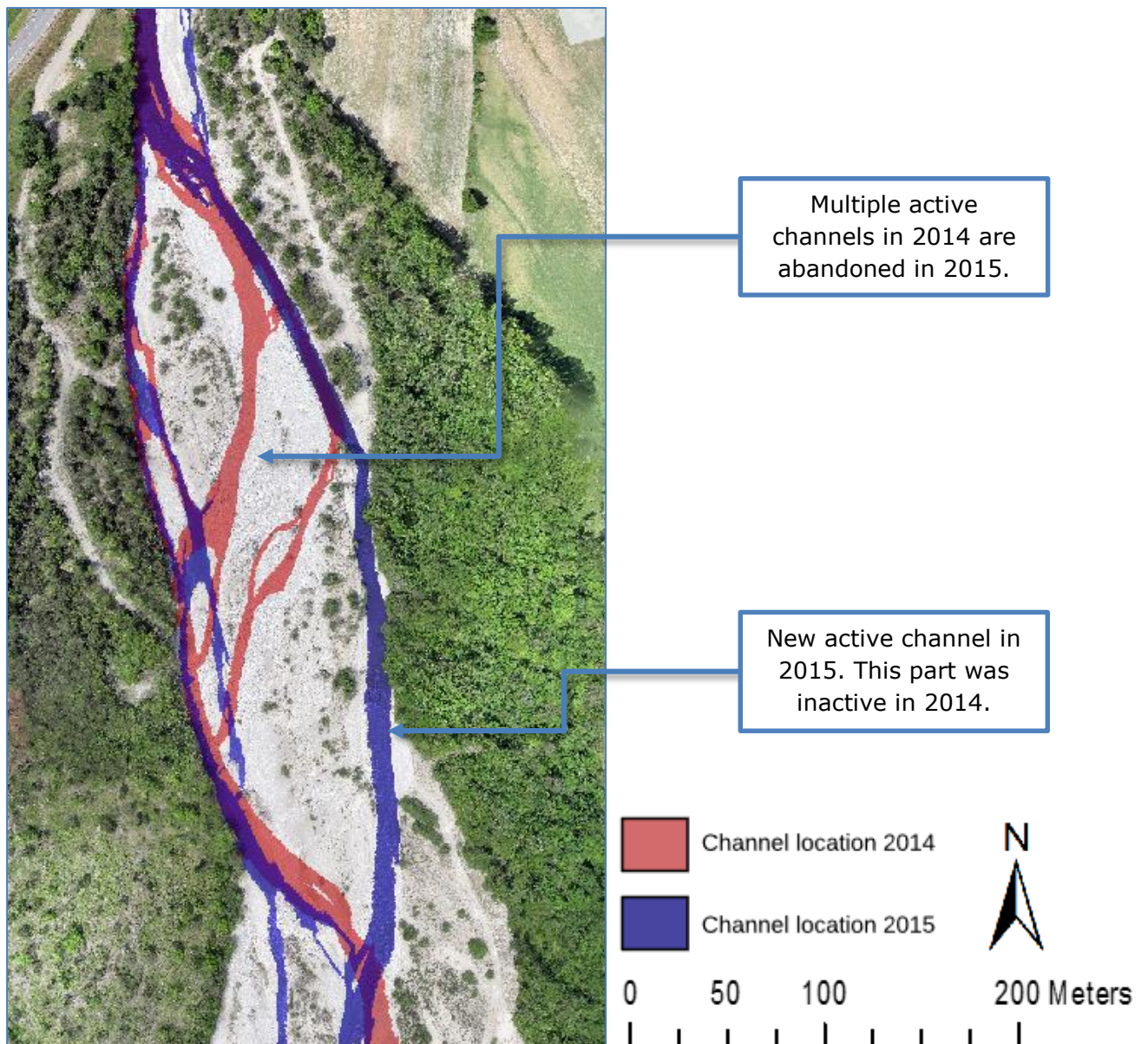
Figure 3.11 Close up of largest river bank at Chabestan in 2015 with classified active channels in 2014 (red) and 2015 (blue).

3.3.2 Channels displacement at La Bâtie-Montsaléon

The La Bâtie-Montsaléon site is characterised by a meander bend and both years have a general meandering pattern. There is no change in the channel location from one side of the river plain to the other between 2014 and 2015. This allows to determine the magnitude of the expanding channel belt at multiple locations (*Figure 3.12* and *Table 3.6*). At these locations, the distance was measured by comparing the difference in distance between the channel in 2014 and the channel in 2015. These values give an indication of the displacements that can occur within one year.
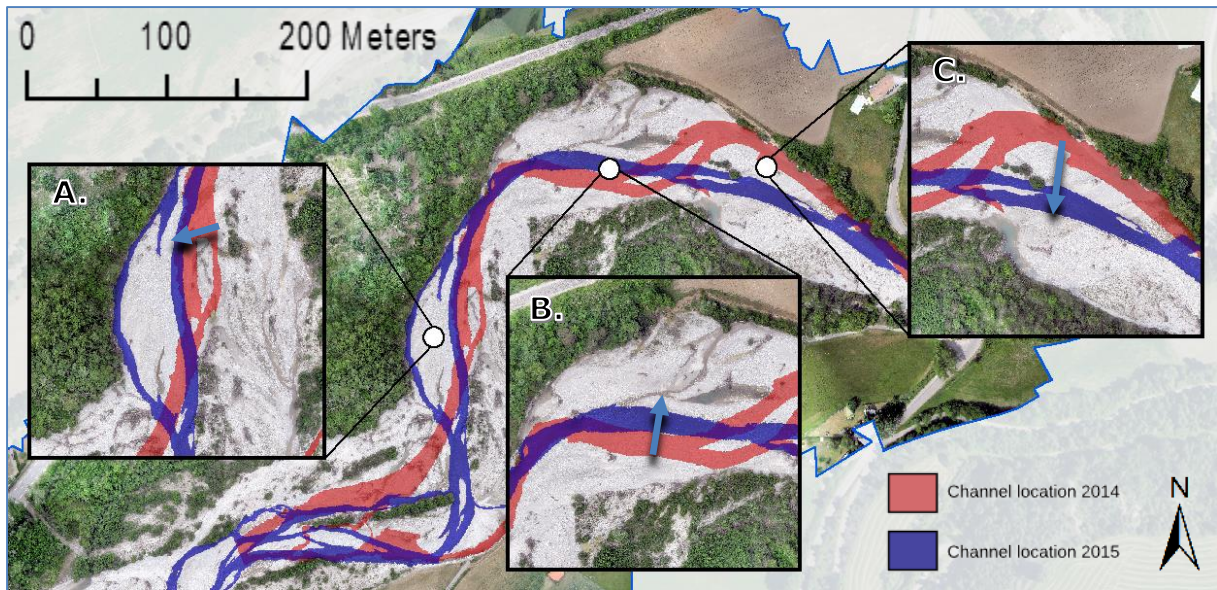
Figure 3.12 Three key locations are highlighted (A, B and C) at La Bâtie-Montsaléon in 2014 (red) and 2015 (blue). The displacement direction of the channel is given by the blue arrow.

Table 3.6 Approximately channel displacements along the major axis between 2014 and 2015 at three locations (*Figure 3.12*) at La Bâtie-Montsaléon.

Location	Approximate channel displacements
A	20 m
B	15 m
C	20 m

At location A, a large part of the river bank was eroded between 2014 and 2015. However, the main channel only moved approximately 20 m between the two snapshots. There is a new secondary channel at a maximum distance of 40 m of the main channel in 2014. In 2015, there was still a secondary channel active at the edge. The other locations (B and C), show only some displacement within the river plain itself. In 2015, the channel has some wandering or braided patterns at the lower left side as there are multiple river banks and between two and four active channels (*Figure 3.13*) while in general the river channel is meandering.
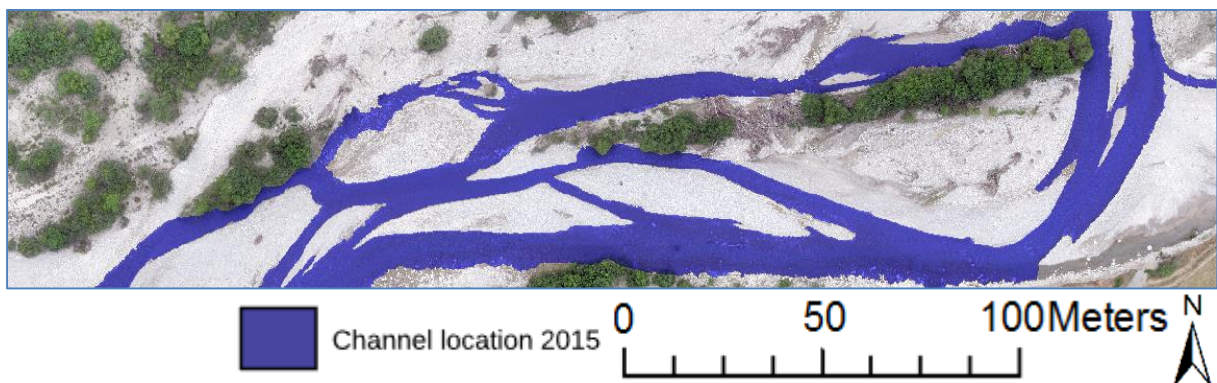
Figure 3.13 Braided pattern with multiple active channels at La Bâtie-Montsaléon in 2015. There are moist sandy locations in the lower right corner.

Between 2014 and 2015, a number of active channels changed and consequently the location of the banks also moved. Logically, when there are many active channels then between those channels small river banks will emerge. The large river banks remain at the same location within one year. However, the edges might experience erosion.

3.3.3 Channels displacement at Serres

Serres is the only research location where the sides of the river have been secured by placing boulders. This has a large impact on the river dynamics as natural conditions are disturbed.

Due to a completely fixed embankment, it is not possible to characterise this river as meandering, wandering nor braided. However, within the river plain there are a couple of displacements (*Figure 3.14A*). The main active channel moved from the left side of the river plain towards the right side. This corresponds with a displacement of approximately 50 m. This is the only significant change at this location. When the channel comes nearer towards the dam, water starts to back up and forms a sheet of water over the morphology of the river, causing the disappearance of the channels. There are no substantial changes in the area close by the Saint-Sauveur dam in 2014 and 2015.

The dry banks are more or less fixed as the channels do not change location between the years. On the bank there is small vegetation that is likely older than one year (*Figure 3.14B*).
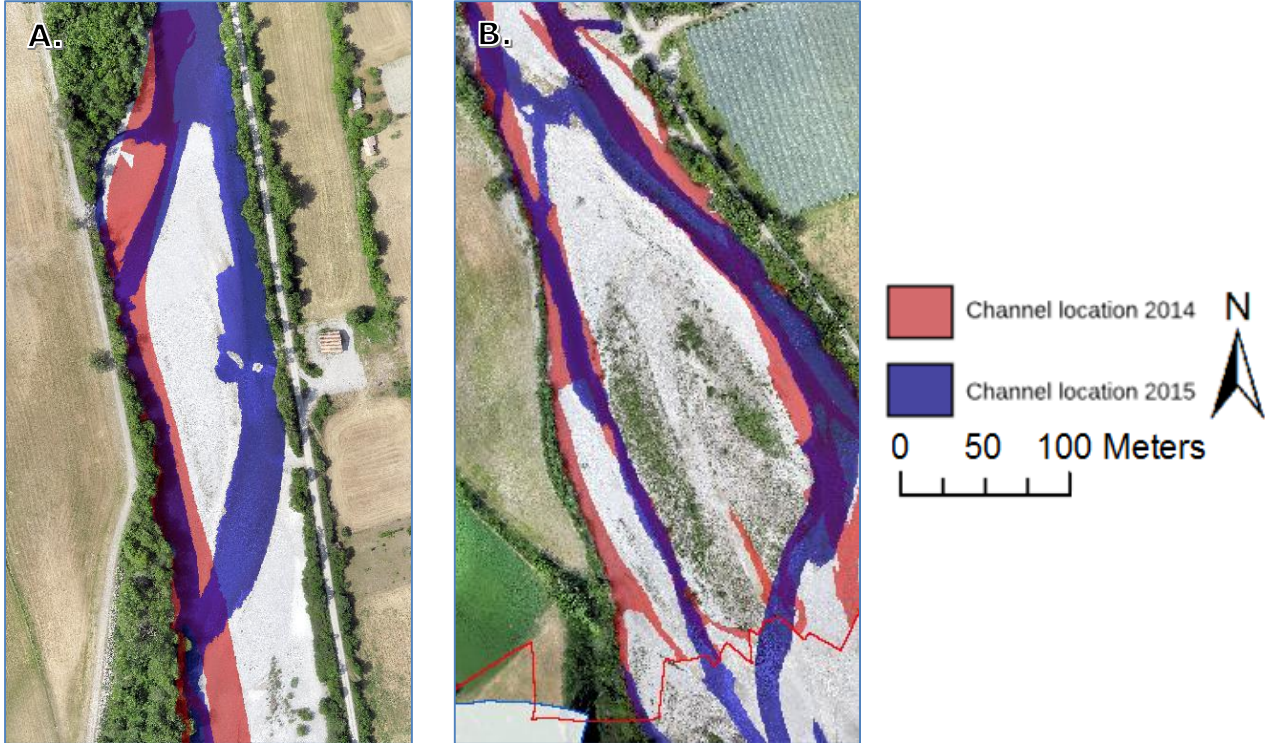
Figure 3.14 (A) Movement of channel 2014 (red) from left side of the river plain to right side of the river plain in 2015 (blue) at Serres. (B) In the middle a vegetated river bank at Serres.
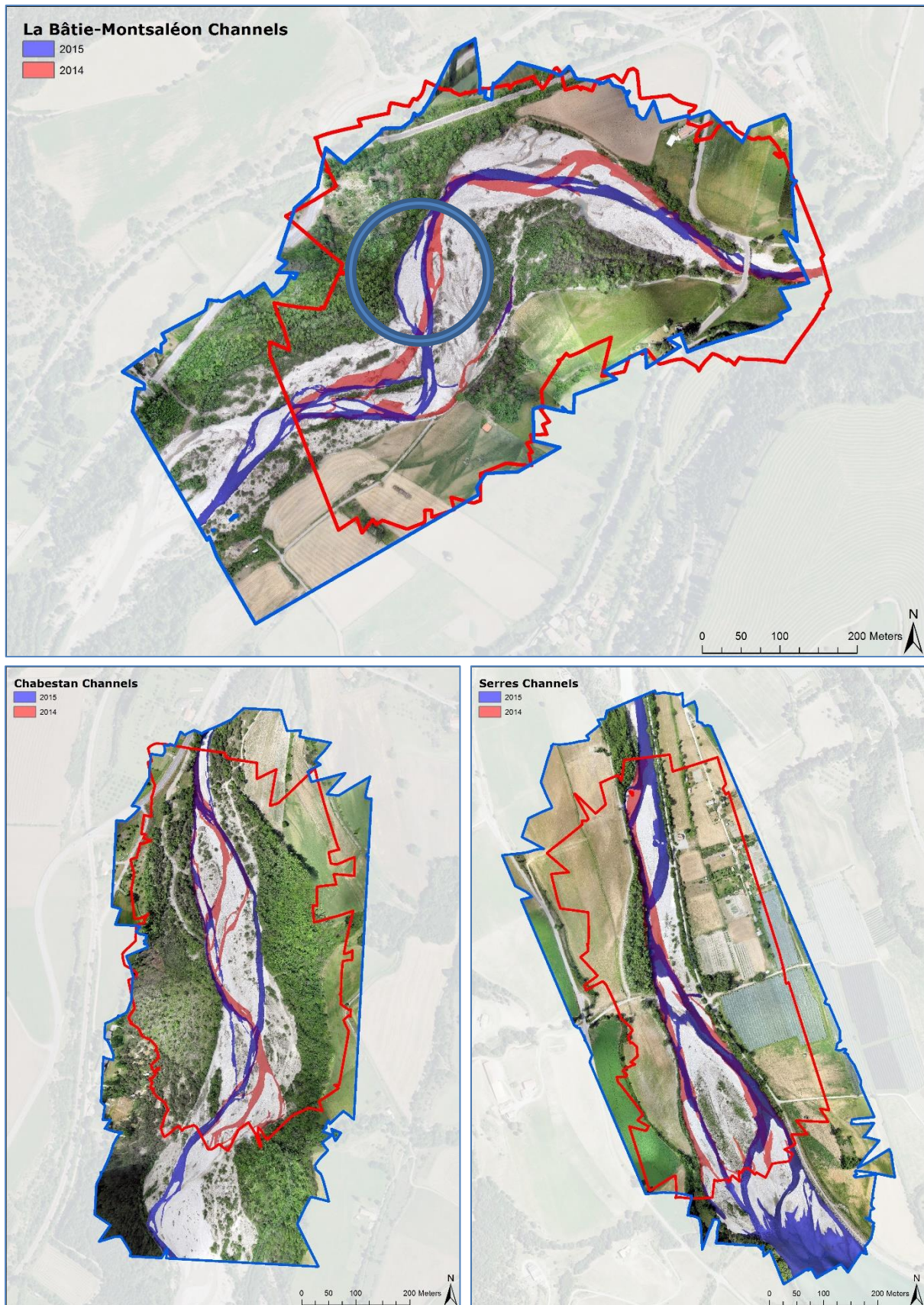
Figure 3.15 Channel and bank displacements for (A) La Bâtie-Montsaléon, (B) Chabestan and (C) Serres. The channels active in 2014 and 2015 are visualised in respectively red and blue. The circle at La Bâtie-Montsaléon indicates the largest erosion site (*discussed in chapter 3.5*).

3.4 Bank erosion

Bank erosion only occurs at Chabestan and La Bâtie-Montsaléon. At Serres the banks of the river are completely fixed by boulders and concrete dykes and consequently excluded from this topic. The bank erosion is estimated using elevation data provided by the OrthoDEMs.

3.4.1 Bank erosion at Chabestan

At Chabestan there are many banks with high steep edges indicating active erosion processes. Only one of these sites can be observed as there are just a couple of trees on top of this river bank instead of being completely covered with trees. In addition, this river bank is located directly next to the active channel.

3.4.1.1 *Transects Chabestan*

Four transects perpendicular to the flow direction were created. The DSM of 2014 and 2015 were compared to determine whether bank erosion took place within one year (*Figure 3.16*).

Figure 3.16 The location of the four transects (A-D) at the bank erosion site at Chabestan in 2014 and 2015.

At transect A (*Figure 3.17A*) there was a main channel in both 2014 and 2015. The edge of the bank moved towards the east with about 1 m. In 2014, the channel was wider. In 2015, sediment was deposited on the left bank with a height increase of approximately 60 cm. The channel incision in 2015 is more than in 2014 as the channel width decreased.

Transect B (*Figure 3.17B*) is located at the point where in 2014 the channel divided up into two channels. This is recognisable in the DSM of 2014 by a small increase in elevation. The right bank indicates some signs of erosion of approximately 1 m. Similarly,

as at transect 1, the left bank does not experience erosion and the channel incises between the years.

Bank erosion starts to increase at transect C (*Figure 3.17C*). Here, bank erosion reaches up to 2 m in the lateral direction. There were still two active channels in 2014 within the middle a small bank. The left side bank does not experience erosion and the channel of 2015 is more incised similarly to the previous two transects.

There is only a secondary channel in 2014 at transect D (*Figure 3.17D*). In 2015, this has become the main channel instead of a secondary channel. This results in more bank erosion. Around 3 m is eroded within a year. On the opposite side of the channel, material is deposited. The main channel is situated lower than the surroundings.

Figure 3.17 Chabestan transects A-D. For all transects an elevation model is plotted in red and blue for 2014 and 2015 respectively. The y-axis shows the elevation in (m) and the x-axis the length of the transects. The location of the channel is indicated by dashed part in the profile line.

In 2015, at transect A there is a clear elevation spike at a location where the channel is located caused by water. Transect B, C and D do indicate some small elevation differences caused by water. In general, the disturbance caused by water is minimal compared to disturbance caused by trees or vegetation.

3.4.2 Bank erosion at La Bâtie-Montsaléon

There is a clear example of a site with bank erosion at La Bâtie-Montsaléon. In 2002, as described in the qualitative description, there was a tarred agricultural road next to the river. However, due to bank erosion, the road was partly collapsed in 2010. In addition, this bank erosion site is easy accessible and visible due to the agricultural fields and no interference of foliage.

3.4.2.1 *Transects La Bâtie-Montsaléon*

Four transects (*Figure 3.18*) were created based on the OrthoDEM of 2014 and 2015. The active channel was not directly next to the transects in 2014. There was still a thin sheet of water located above the river banks. In 2015, transect A is located perpendicular to the channel but the transect B, C and D are located on the moist and sandy river. These transects were compared to determine the erosion between 2014 and 2015.
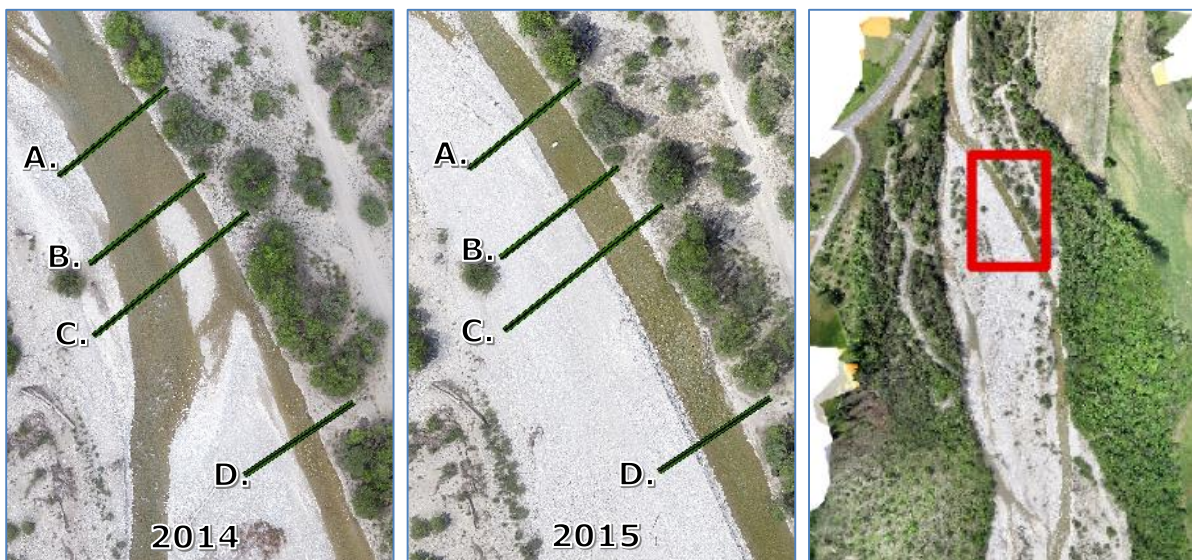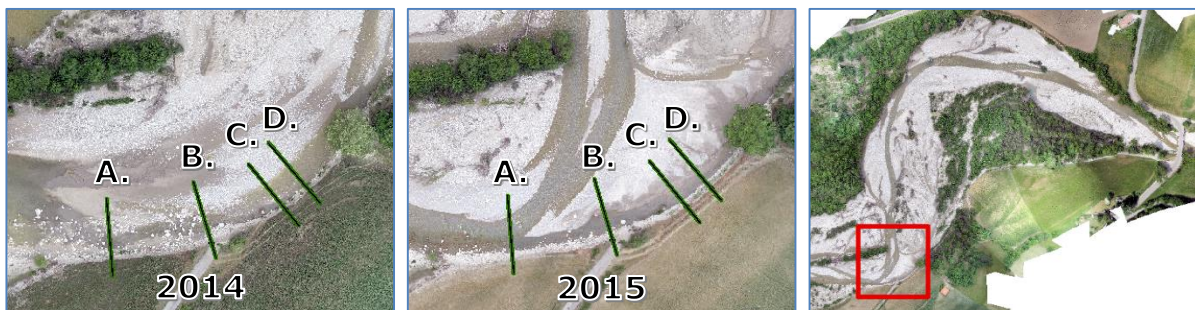

Figure 3.18 The location of the four transects (A-D) at the bank erosion site at La Bâtie-Montsaléon in 2014 and 2015.

Transect A (*Figure 3.19A*) is located nearest to the main active channel in 2015 at only a distance of 3 m. In 2014, there was only a small secondary channel at this location. The main active channel in 2014 was located on the opposite site of the river plain. Between 2014 and 2015, 1.5 m lateral bank erosion occurred.

Transect B (*Figure 3.19B*) is situated next to a river bank and is approximately 20 m away from the active channel in 2015. There was a small stream next to the bank erosion site in 2014. No bank erosion could be measured between 2014 and 2015. The graph shows a small (centimeters) increase of the size of the bank in 2015.

The subsequent transect C and D (*Figure 3.19C* and *Figure 3.19D*) do not indicate any bank erosion between 2014 and 2015. The distance to the active channel in 2015 increased to more than 30 m and in 2014 there was, similar to the other transects, only a small stream next to the bank erosion site. Transect C and D show that there is 20 cm of material deposited on the edge below the erosion site and 50 cm on the closest river bank between 2014 and 2015. On top of the bank erosion site, there are some artefacts that show an elevation increase in 2015 that is likely caused by agricultural crops.

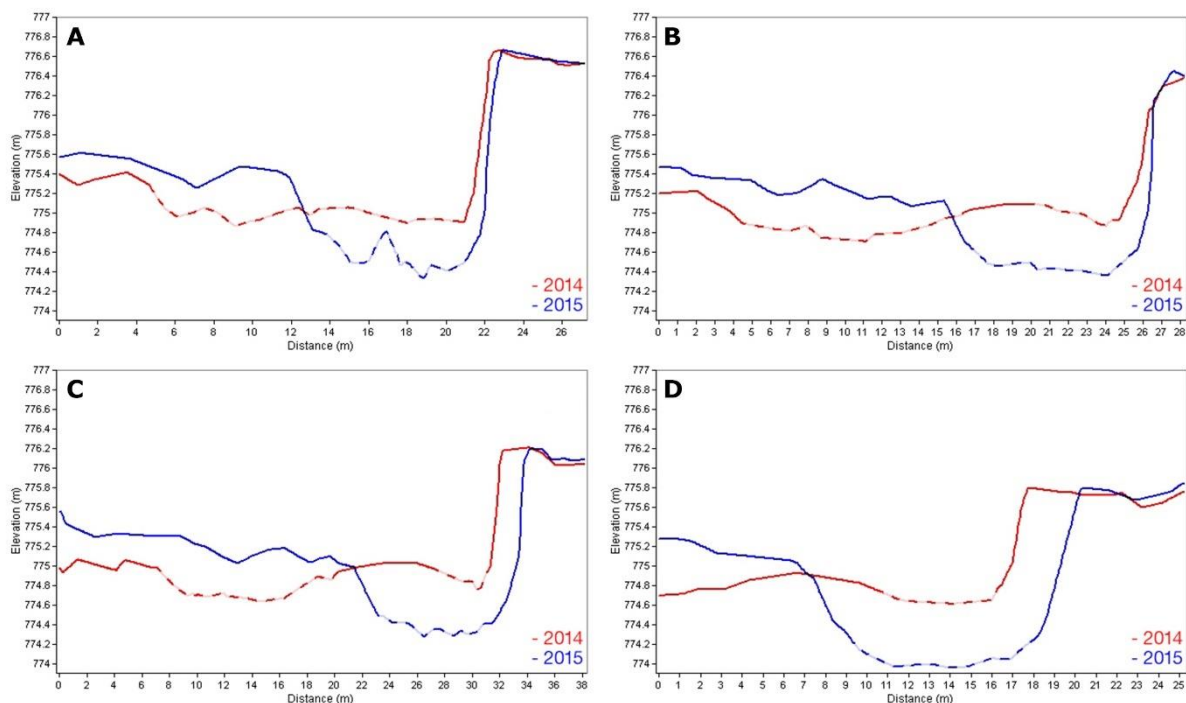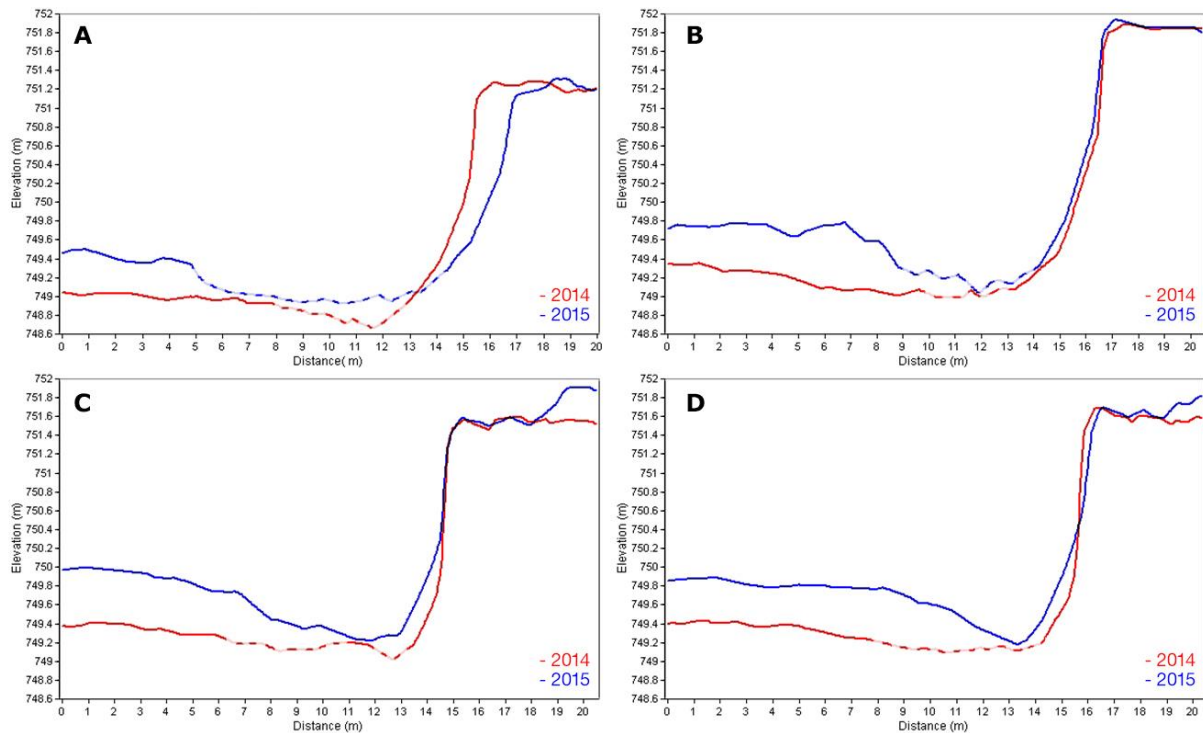Figure 3.19 La Bâtie-Montsaléon transects A-D. For all transects an elevation model is plotted in red and blue for 2014 and 2015 respectively. The y-axis shows the elevation in (m) and the x-axis the length of the transects. The location of the channel is indicated by dashed part in the profile line.

The La Bâtie-Montsaléon erosion site was less active compared to the erosion site at Chabestan. The maximum erosion was 1.5 m at La Bâtie-Montsaléon and 3 m at Chabestan. Besides that, three out of the four transects at La Bâtie-Montsaléon do not even indicate any bank erosion between 2014 and 2015 but rather deposition at the foot of the bank. So activity between 2014 and 2015 was modest and a longer time series is needed to observe bank erosion at these transects.

3.5 Erosion volume

There was a large bank erosion event between 2014 and 2015. That was not visible or identified during the fieldwork. When the OrthoMosaic of 2015 was compared with the OrthoMosaic of 2014, it revealed that a large patch of the bank including trees was eroded (*Figure 3.20*). The bank was not accessible to due dense vegetation on top on the bank. During acquisition of the 2015 dataset there was still a secondary channel remaining on the foot of the bank in.

An area with a length of approximately 150 m and a maximum with of 40 m was eroded. This corresponds with an area of 3296 m^2. For each cell an elevation difference in meters (elevation 2014 – elevation 2015) was calculated. The elevation values per cell for this site in 2015 are based on the OrthoDEM of 2015. For 2014, the elevation values per cell at the site were completely disturbed by vegetation. Therefore, an estimated elevation of 753 m was used for each cell. This value was obtained from nearest clearly observable river bank in the 2014 dataset. By multiplying elevation values per cell with the cell size a volume difference per cell is acquired. By adding up each cells, a volume difference for the entire bank erosion site is acquired. This results in a volume change of 5853.55 m^3.

The bank erosion reaches up to a maximum width of 40 m. This is significantly larger than the bank erosion of a maximum width of 3 m that was previously observed at transects at Chabestan and La Bâtie-Montsaléon.
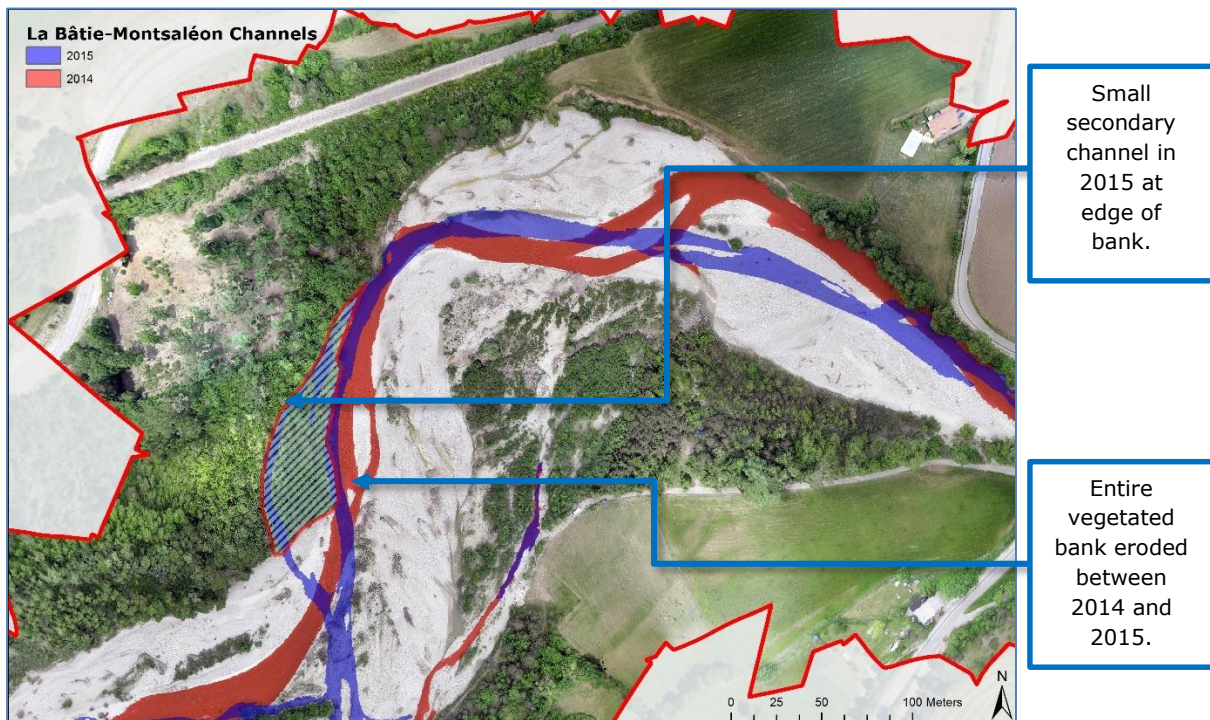
Figure 3.20 La Bâtie-Montsaléon OrthoMosiac of 2014 with the location of the channel of 2014 (red) and 2015 (blue). The striped polygon indicates the part of the bank that was eroded in 2015.

4 Discussion

This chapter is divided into two parts. The first part will focus on the accuracy of the resulting OrthoMosaics and OrthoDEMs products. A good insight in the sources of uncertainty and the causes of errors in the final products is useful to improve future research investigation. Suggestions and recommendations are given to improve future dataset quality. The second part will discuss the river dynamics, channel displacements and bank erosion.

4.1 Accuracy and spatial resolution

Markers were distributed across the research locations to geo-reference the OrthoMosaic and OrthoDEMs. These markers were mapped with a DGPS to assure an accuracy up to centimetres. With this method an average positional accuracy of up to 30 cm is reached in the XY-direction and 2 cm in the Z-direction across all datasets. The orientation and magnitude of the errors between the measured markers and the markers within the OrthoMosaic are random. This shows that the entire area is covered from all angles.

The most interesting finding concerning the accuracy is that the derived accuracy for the Z-direction is excellent, while the XY-direction accuracy is not on the same level. This likely occurs due to the nature of the terrain (*Figure 4.1*). Although the Buëch has a high gradient, elevation differences overall are not that large. Therefore, a large error in the XY direction will result in a small error in the Z-direction.

Figure 4.1 Elevation difference across the area are relatively small. Therefore, a large error in XY-direction will corresponds with a small error in Z-direction.

The accuracy analysis was not an independent accuracy analysis. All available markers were unfortunately required to optimise and geo-reference the dataset. Consequently, the derived accuracy was based on the same markers that were used as input. With an increasing distance to a marker the error will increase. Therefore, the derived accuracy values for the 2014 and 2015 datasets are more accurate than when analysis was based on independent markers. There are measurements that indicate an error up to meters in the Z-direction (for example at Chabestan the maximum error is -2.12 m in 2014). This is the result of the marker location. These markers were located near trees that obstructed the view. The size of the positional errors is influenced by different sources of uncertainty or suboptimal conditions and are different per dataset.

In addition, these datasets have a high spatial resolution (cell size) of approximately 3 cm for the OrthoMosaic and 6 cm on the OrthoDEM that can be compared with TSL or LiDAR. The spatial resolution is much higher compared with satellite data. For example, RGB products of ASTER and Landsat 8 have a spatial resolution of 15 m and 30 m respectively (*Lillesand and Kiefer, 2015*). In comparison, the final products are highly accurate and detailed and, therefore, ideal to be used to quantify geomorphic changes between years even on scales smaller than a meter.

4.2 Sources of uncertainties

To better understand the quality and practicality of the exported products (OrthoMosaics and OrthoDEMs), it is important to assess different sources of uncertainty.

Some sources of uncertainty can be minimalised or removed. Most of these uncertainties are related to the quality of the dataset. A low quality dataset can be a result of insufficient resolution or motion blur (*Figure 4.2*) within the imagery (*Bemis et al., 2014*). Low quality images are excluded from analysis. Not every image can be removed as sometimes these images are necessary to cover an area. For example, the bridge at La Bâtie-Montsaléon is an important location as here the river plain becomes narrow. The bridge is covered by only a few images that in were not optimal. These images could not be removed as there was no substitute available for these images.

Figure 4.2 An photograph that is not sharp due to motion blur.

Within the datasets, brightness differences occur based on the time and conditions during acquisition. In addition, when two highly contrasting surfaces such as white river plains and patches of green forests are within a single frame, the imagery will be overexposed (*Figure 4.3*). This occurs at almost all edges of the river plain and this will increase the error associated with the images alignment (*James and Robson, 2012*). The images that contain brightness differences were removed where possible.

Figure 4.3 Brightness differences caused by the high contrast difference between vegetation and riverbed.

Different sources of uncertainty could be based on the method of image acquisition. The used UAV did not acquire the imagery along a pre-programmed flightpath and the position of the camera was not identified during the acquisition of imagery. The platform height could vary during image acquisition (*Figure 4.4*). This will result in different scales between the photographs that affected the resolution and details in the textures. The SfM algorithm is scale invariant and thus can solve changes in scale between imagery (*Smith et al., 2015*). However, large differences in scale can prevent accurate matching and therefore are best avoided (*Bemis et al., 2014*). In addition, in general overlap and orientation is random (*Figure 4.4*). The SfM algorithm uses the different angles between the imagery to reconstruct the position of the camera in a 3D scene (*Smith et al., 2015*). Nevertheless, SfM is more accurate when the imagery is taken within straight flight paths with the same percentage of overlap as the interference on key point matching caused by lightning difference and shadow location will be minimalised (*James and Robson, 2012, 2014*). Likewise, difference in orientation such as yaw, pitch and roll between the imagery are solved (*Smith et al., 2015*). However, correct key points are optimally identified when angular changes are limited to 10°-20° or not larger than 25°-30° between the camera locations. (*Bemis et al., 2014; Moreels and Perona, 2007*).
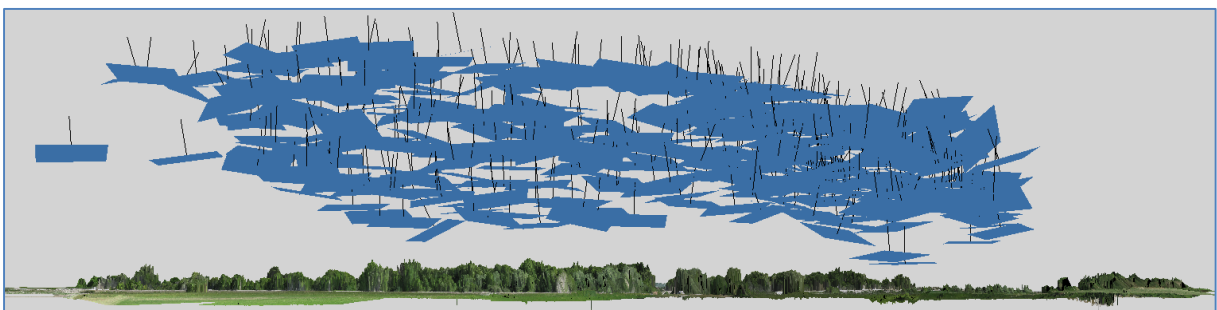

Figure 4.4 Illustration of varying camera location. Platform height and camera orientation and percentage of overlap between imagery varies.

Some sources of uncertainty cannot easily be reduced in these datasets. These sources of uncertainty are caused by vegetation and water. Vegetation and water are not static between imagery. In addition, water is shiny which result in sun glitter (*Figure 4.5*). This results in changing apparent features between the camera position and corresponding imagery (*Smith et al., 2015*). The SfM algorithm is able to solve imagery that contain vegetation and water. However, due to the changing apparent features it is less accurate (*Dietrich, 2016*). On the OrthoMosaic, texture near vegetation and water are distorted. Vegetation and water are associated with this research area and will always be present. This can be solved by manually masking all water and vegetation in all input imagery.

Figure 4.5 Water with sun glitter. The apparent features of the water with sun glitter changes from different viewing angles.

4.3 River dynamics

By analysing the OrthoMosaics and OrthoDEMs and by quantifying bank erosion and channel displacements, it is apparent that the Buëch is an active river at the research locations Chabestan and La Bâtie-Montsaléon. At Serres, the Buëch is almost inactive as there the entire embankment is fixed and conditions controlled by humans.

Bank erosion and channel displacement occur during events with higher discharge. At the identified bank erosion sites in Chabestan and La Bâtie-Montsaléon, adjacent to the main channel, lateral erosion in general occurred up to approximately 3 m. In a comparable fluvial geomorphology study by Miřijovský and Vavra (*2012*) lateral bank erosion of a meandering river reached up to 5 to 7 m. However, a larger erosion event occurred at a location that was not identified during fieldwork as a bank erosion site. At La Bâtie-Montsaléon a river bank with trees alongside a length of 150 m and a maximum width of 40 m eroded between 2014 and 2015. A volume of 5853.55 m^3 was displaced. This is the largest event that is recorded in the dataset and, consequently, must be the result of large discharges. Unfortunately, there is no discharge data available that can be linked to this or other erosion events. It is not possible to determine the location where the next large erosion or channel displacement will take place as these processes are irregular. During image acquisition, the Buëch had primarily meandering characteristics. The location of the

channel varies each year. Maximum channel displacement of the main channels reached up to 20 m at La Bâtie-Montsaléon. In the OrthoDEM many old channels can be identified with varying depths. When discharge increases, the number of active channels increases, creating a more braided pattern until bank full discharge conditions.

The flow dynamics are influenced by the morphology of the channel (*Miřijovský and Langhammer, 2015*). There are rapids at some shallow locations. These rapids occur when the flow reaches almost critical conditions in a bedrock controlled river (*Magirl et al., 2009*). Tree remains or other obstructions in the channel can function as a sediment trap. Behind tree remains, vegetation can start to grow which offer flow resistance and strengthen sediments with their roots (*Gurnell et al., 2012*). In the river plain of the Buëch, vegetation can be identified at identical locations at different years. This suggests that between those years the erosion processes were too small or even inactive to remove the already pioneering or sprouting vegetation (*Gurnell et al., 2012*). Differences in deposited materials adjacent to the river become evident as humidity difference during irrigation of the fields. This especially occurs at La Bâtie-Montsaléon and these differences are the result of depositions that have different permeability. These deposits are possible old river channels and show characteristics with old meander belts. This is in accordance with the fact that the valleys through which the Buëch flows are presently less wide than at the higher erosional phases of the Buëch (*Descroix and Gautier, 2002)*. In addition, although the Buëch is presently in a low eroding phase, the sediment budget is disturbed by a dam and quarries that excavate gravel. This results in a deficit of sediment and, consequently, an increase in carrying capacity. This will lead to an increase of erosion or incision until the sediment budget is in balance *(Frings et al., 2014a*).

An UAV acquired dataset offers an excellent start to determine river dynamics and quantify changes as processed UAV datasets have a high spatial resolution with a high accuracy including small topographical details to observe small changes in the river geomorphology (*Dietrich, 2014; Miřijovský and Vavra, 2012*). The main advantage is that UAV systems are mobile and easy to transport and areas can quickly and often be covered enabling the option to create time series. With larger time series, more site with bank erosion or channel displacements can be identified. In addition, compared with datasets of similar quality derived with TSL or LiDAR the data acquisition less expensive due to lower material cost of the camera and UAV (*Smith et al., 2015*). Another advantage of using an UAV compared with LiDAR is that there is a person in the field to identify key locations or perform additional measurements for later analysis.

4.4 Challenges

With Agisoft PhotoScan and the SfM algorithm, UAV datasets can be processed successfully with a high resolution. However, a couple of problems were experienced related to processing or subsequent analysis of the OrthoMosaic and OrthoDEM.

4.4.1 Classification channel displacements

It was preferred to automatically classify the channel location in OrthoMosaics by supervised or unsupervised classification. The result with supervised and unsupervised classification was inadequate as the channel was not recognisable. The channel was mostly mixed with vegetation. With these mixed classes, quantifying channel displacement was impossible. The most optimal option would be to mask out the vegetation by calculating the NDVI. However, for these datasets there was no NIR data available. Vegetation and channels can be distinguished based on elevation data from the OrthoDEMs as vegetation is higher than the channel but this led unfortunately to critical program errors during classification. Otherwise, Object Based Image Analysis (OBIA) could be used to automatically classify the OrthoMosaic by including neighbourhood and shape information but for this study it would be more time consuming than manual mapping.

4.4.2 Artefacts OrthoDEMs

The resulting OrthoDEMs have a high resolution of approximately 5.7 cm. This gives a detailed view on the elevation of the surface. There is one complication with the OrthoDEMs. The derived product is a DSM and not a Digital Terrain Model (DTM). A DSM gives the elevation including vegetation while a DTM gives elevation data of only the ground level. In general, this is not a large problem but at bank erosion sites it provides a challenge. At bank erosion sites, it occurs that either vegetation hangs over the bank or tree remains obstructs the view (*Figure 4.6*).

Figure 4.6 Tree remains at the bank erosion site in Chabestan 2015.

For example, at La Bâtie-Montsaléon a bank eroded with a maximum width of 40 m but the bank was completely covered with trees. This was addressed by estimating the height of the bank based on elevation of neighbours. In addition, vegetation results in artefacts in the OrthoDEM (*Figure 4.7A*). Near vegetation the OrthoMosaic is blurry, (*Figure 4.7B*)

making it difficult to determine the edge of the river bank. This is a disadvantage of UAV products in comparison with LiDAR products. LiDAR data contains multiple returns for either crown of vegetation or the ground level (*Sun Guoqing and Jon Ranson, 2000*).
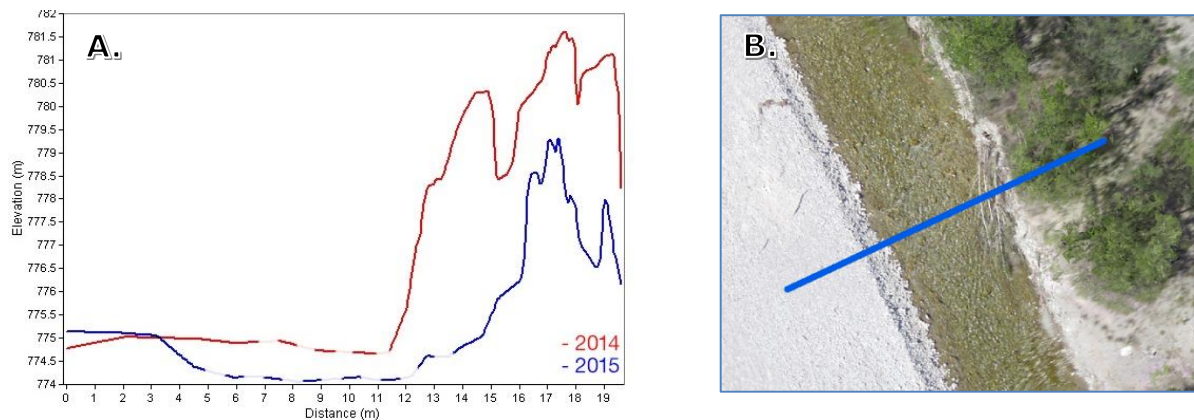

Figure 4.7 (A) Profile of 2014 and 2015 with artefacts between a distance of 12 – 19 m. The channel location is indicated by the dashed line. (B) Location of the transect at Chabestan, artefacts and blurring caused by tree remain and vegetation on top of bank.

4.4.3 Alignment La Bâtie-Montsaléon 2011

The only dataset that could not successfully be processed with the used workflow (*chapter 2.4.2 general workflow*) was La Bâtie-Montsaléon 2011 as the photographs could not be aligned. The difference between the La Bâtie-Montsaléon 2011 dataset compared with all other datasets was that the photographs were taken closer to the ground. This resulted in more detailed images. Unfortunately, there was not enough overlap as the minimum requirement of approximately 60% overlap between images (*Dietrich, 2014, 2016*) was not met. This emphasises that the increase in resolution must be balanced with platform height or a shorter time between images acquisition to assure sufficient overlap and consequently successful processing.

4.5 Recommendations

There are many improvements possible to obtain an even more accurate 3D model with the accompanying OrthoMosaic and OrthoDEMs.

4.5.1 Materials

Literature suggest that XY accuracy up to a few centimetres can be reached with an optimal SfM workflow. Errors smaller than 10 cm for XY-direction and Z-direction have been achieved in other studies (*Mesas-Carrascosa et al., 2014; Ruzgienė et al., 2015; Uysal et al., 2015*). To get a better quality dataset, there are a couple of changes advised for the used materials during the image acquisition. At present the camera location of the imagery is unknown. When this information is added by using a GPS and altimeter aboard the UAV, the processing time in Agisoft PhotoScan will be reduced as the imagery can be grouped into clusters that are near each other. In that case, only the imagery within this clusters needs to be matched. Without the camera location, each image is compared with all other

imagery or a pre-scan is used (*Smith et al., 2015*). A GPS in the UAV is convenient but cannot replace markers in the field.

Varying platform height due to changing flight altitude is preferably prevented. A change in scale between imagery, because of different height of the camera position, will make feature detecting more difficult and less precise if the variations are too large (*Bemis et al., 2014*). This is the result of changes in texture. When the image is taken closer to the ground, more detail will be visible as there are more pixels available for a smaller area than compared with higher elevation. This can be prevented by using an autopilot that continuously monitors the UAVs position and follows a pre-programmed optimal flight path (*Ruzgienė et al., 2015*). This will also eliminate problems regarding sufficient overlap (>60% or more) (*Dietrich, 2014, 2016*) and too large angular changes (>20° or more) (*Bemis et al., 2014; Moreels and Perona, 2007*). In addition, imagery on the same camera location does not add more information to the model and is preferable avoided (*Favalli et al., 2012*). This makes the datasets smaller and less time consuming to process.

To quantify bank erosion, small details such as the exact locations of the edges of the natural embankment are needed. If the details in the imagery are insufficient or the picture is blurred, small differences will be undetectable. To solve this problem, a better camera with higher resolution and better stabilisation can be used. Otherwise, the resolution of the imagery can be increased by lowering flight altitude. Optionally, shutter speed can be decreased to minimise motion blur (*Flener et al., 2013; Turner et al., 2015*) but this can also result in not enough light falling on the sensor under different conditions.

4.5.2 Future research

The scope of this research can be expanded by including more datasets that are geo-referenced. This will result in a longer time series that enables the description of more detailed characteristics and dynamic processes of the river. More frequent UAV flights can add to the understanding of river dynamics as more and different conditions are observed. Matching discharge data with erosion events will give more insight in the dynamics. Different type of sensors can be included. A NIR camera is especially convenient for fluvial geomorphological research. When a NIR camera is used in conjunction with the RGB camera, the matching NIR dataset can be used to classify the vegetation with NDVI. This will enable the opportunity to focus on the river plain by automatically masking out the vegetation or to expand the research to the vegetation related research fields.

VR is rapidly evolving and more commonly used. The OrthoMosaics and OrthoDEMs derived with Agisoft PhotoScan can be exported to suitable data formats. These 3D models can be viewed on 3D monitors such as in the iScope available within Shell and with VR headsets. This will give a realistic experience that can potentially provide new insights.

5 Conclusion

An Unmanned Airborne Vehicle (UAV) is a flexible lightweight tool to acquire high spatial resolution imagery. The imagery was processed with Structure from Motion (SfM) algorithm. This algorithm aligns the imagery and reconstruct the 3D model based on different viewing angles. The resulting products such as the OrthoMosaic and OrthoDEM give a detailed view of multiple years of Chabestan, La Bâtie-Montsaléon and Serres alongside the Buëch. These products have a high spatial resolution (cell size) of approximately 3 cm for the OrthoMosaic and approximately 6 cm for the OrthoDEM.

The accuracy is calculated by comparing Differential Global Position System (DGPS) measurements of markers that function as Ground Control Points (GCPs) with the same marker in the OrthoMosaic. This resulted in a positional accuracy in the XY-direction of approximately 30 cm and in the Z-direction of approximately 2 cm. The error had a random error orientation which indicates that the areas were covered from all angles. The workflow with UAVs and SfM is usable in fluvial geomorphological research and easily repeatable. The method can be improved by adding to the UAV a GPS, an altimeter and an autopilot which are expected to further increase the accuracy to errors smaller than 10 cm in the XY-direction.

The Buëch can be defined as a river that has primarily meandering characteristics. Depending on discharge multiple secondary channels are becoming active, resulting in braided patterns. Accurate data combined with high spatial resolution makes it possible to map patterns, quantify bank erosion (extend and volume) and channel displacements to determine river dynamics even when changes occur on a small sub-meter scale.

By analysing the OrthoMosaics and OrthoDEMs for all available years, it is apparent that the Buëch is geomorphological very active at La Bâtie-Montsaléon and Chabestan. Channel displacements up to 20 m are observed at La Bâtie-Montsaléon within a single year and bank erosion occurs. An OrthoMosaic is a good addition to field observations. The largest bank erosion site at La Bâtie-Montsaléon was not identified in the field but recognised in the OrthoMosaics of 2014 and 2015. A stretch of 150 m of the river bank including patches of trees on top of the bank were eroded with a maximum width of 40 m. This resulted in an estimated volume change of 5853.55 m^3. From 2002 to 2015 agriculture fields and an agricultural road were eroded at La Bâtie-Montsaléon. At Chabestan, a large active channel was abandoned between 2014 and 2015. The new active channel eroded a river bank, with a maximum lateral erosion of up to 3 m. The Buëch, at the research location in Serres is not that active as this location is human controlled. The banks are fixed with boulders and concrete dykes. At Serres, the only changes observed are channel displacements within the river plain.

References

Agisoft PhotoScan Professional Edition Version 1.1.6 build 2038 (64-bit) © 2015 Agisoft LLC., available on http://www.agisoft.com/ (last accessed August 2016)

Bemis, S. P., Micklethwaite, S., Turner, D., James, M. R., Akciz, S., T. Thiele, S. and Bangash, H. A.: Ground-based and UAV-Based photogrammetry: A multi-scale, high-resolution mapping tool for structural geology and paleoseismology, J. Struct. Geol., 69(PA), 163–178, doi:10.1016/j.jsg.2014.10.007, 2014.

Bhardwaj, A., Sam, L., Akanksha, Martín-Torres, F. J. and Kumar, R.: UAVs as remote sensing platform in glaciology: Present applications and future prospects, Remote Sens. Environ., 175, 196–204, doi:10.1016/j.rse.2015.12.029, 2016.

Descroix, L. and Gautier, E.: Water erosion in the southern French Alps: Climatic and human mechanisms, Catena, 50(1), 53–85, doi:10.1016/S0341-8162(02)00068-1, 2002.

Dietrich, J. T.: Application of Structure-from-Motion photogrammetry to fluvial geomorphology, PhD Thesis, (December), 109, 2014.

Dietrich, J. T.: Riverscape mapping with helicopter-based Structure-from-Motion photogrammetry, Geomorphology, 252, 144–157, doi:10.1016/j.geomorph.2015.05.008, 2016.

Favalli, M., Fornaciai, A., Isola, I., Tarquini, S. and Nannipieri, L.: Multiview 3D reconstruction in geosciences, Comput. Geosci., 44, 168–176, doi:10.1016/j.cageo.2011.09.012, 2012.

Flener, C., Vaaja, M., Jaakkola, A., Krooks, A., Kaartinen, H., Kukko, A., Kasvi, E., Hyyppä, H., Hyyppä, J. and Alho, P.: Seamless mapping of river channels at high resolution using mobile LiDAR and UAV-photography, Remote Sens., 5(12), 6382–6407, doi:10.3390/rs5126382, 2013.

Fleury, T. J., Pothin, V., Vella, C., Dussouillez, P. and Izem, A.: Low altitude aerial photogrammetry application to braided river systems . Example of the Buech River , Alps , France ., Geophys. Res. Abstr., 17, 8695, 2015.

Fonstad, M. A., Dietrich, J. T., Courville, B. C., Jensen, J. L. and Carbonneau, P. E.: Topographic structure from motion: A new development in photogrammetric measurement, Earth Surf. Process. Landforms, 38(4), 421–430, doi:10.1002/esp.3366, 2013.

Frings, R. M., Berbee, B. M., Erkens, G., Kleinhans, M. G. and Gouw, M. J. P.: Human-induced changes in bed shear stress and bed grain size in the River Waal (The Netherlands) during the past 900 years, Earth Surf. Process. Landforms, 34(4), 503–514, doi:10.1002/esp.1746, 2009.

Frings, R. M., Döring, R., Beckhausen, C., Schüttrumpf, H. and Vollmer, S.: Fluvial sediment budget of a modern, restrained river: The lower reach of the Rhine in Germany, Catena, 122, 91–102, doi:10.1016/j.catena.2014.06.007, 2014a.

Frings, R. M., Gehres, N., Promny, M., Middelkoop, H., Schüttrumpf, H. and Vollmer, S.: Today's sediment budget of the Rhine River channel, focusing on the Upper Rhine Graben and Rhenish Massif, Geomorphology, 204, 573–587, doi:10.1016/j.geomorph.2013.08.035, 2014b.

Gurnell, A. M., Bertoldi, W. and Corenblit, D.: Changing river channels: The roles of hydrological processes, plants and pioneer fluvial landforms in humid temperate, mixed load, gravel bed rivers, Earth-Science Rev., 111(1-2), 129–141, doi:10.1016/j.earscirev.2011.11.005, 2012.

HYDRO Discharge Datasets (*French), available on* http://www.hydro.eaufrance.fr/ (last accessed August 2016)

Immerzeel, W. W., Kraaijenbrink, P. D. A., Shea, J. M., Shrestha, A. B., Pellicciotti, F., Bierkens, M. F. P. and De Jong, S. M.: High-resolution monitoring of Himalayan glacier dynamics using unmanned aerial vehicles, Remote Sens. Environ., 150, 93–103, doi:10.1016/j.rse.2014.04.025, 2014.

Institut Géographique National Datasets (*French)*, available on http://www.ign.fr/ (last accessed August 2016)

James, M. R. and Robson, S.: Straightforward reconstruction of 3D surfaces and topography with a camera: Accuracy and geoscience application, J. Geophys. Res. Earth Surf., 117(3), 1–17, doi:10.1029/2011JF002289, 2012.

James, M. R. and Robson, S.: Mitigating systematic error in topographic models derived from UAV and ground-based image networks, Earth Surf. Process. Landforms, 39(10), 1413–1420, doi:10.1002/esp.3609, 2014.

Javernick, L., Brasington, J. and Caruso, B.: Modeling the topography of shallow braided rivers using Structure-from-Motion photogrammetry, Geomorphology, 213(MAY), 166–182, doi:10.1016/j.geomorph.2014.01.006, 2014.

Kraaijenbrink, P., Meijer, S. W., Shea, J. M., Pellicciotti, F., De Jong, S. M. and Immerzeel, W. W.: Seasonal surface velocities of a Himalayan glacier derived by automated correlation of unmanned aerial vehicle imagery, Ann. Glaciol., 57(71), 103–113, doi:10.3189/2016AoG71A072, 2016.

LaMétéo Climate Datasets (*French)*, available on http://www.lameteo.org (last accessed August 2016)

Landau, H., Chen, X., Klose, S., Leandro, R. and Vollath, U.: Trimble's Rtk And Dgps Solutions In Comparison With Precise Point Positioning, Int. Assoc. Geod. Symp., 133, 709–718, doi:10.1007/978-3-540-85426-5_81, 2009.

Liébault, F., Lallias-Tacon, S., Cassel, M. and Talaska, N.: Long profile responses of alpine braided rivers in se France, River Res. Appl., 29(10), 1253–1266, doi:10.1002/rra.2615, 2013.

Lillesand, T. M. and Kiefer, R. W.: Remote sensing and image interpretation. 7th edition, Remote Sens. image Interpret. [online] Available from: http://www.scopus.com/inward/record.url?eid=2-s2.0-0018730387&partnerID=tZOtx3y1, 2015.

Magirl, C. S., Gartner, J. W., Smart, G. M. and Webb, R. H.: Water velocity and the nature of critical flow in large rapids on the Colorado River, Utah, Water Resour. Res., 45(5), 1–17, doi:10.1029/2009WR007731, 2009.

Malaimani, E. C.: DGPS Principles, Errors, and Achievable Accuracies, Geospatial Technol. Clim. Chang., 10, 239–246, doi:10.1007/978-3-319-01689-4_14, 2013.

Marek, L., Jakub, M. and Pavel, T.: Monitoring of the Shallow Landslide Using UAV Photogrammetry and Geodetic Measurements, Eng. Geol. Soc. Territ. - Vol. 2 Landslide Process., 2, 1–2177, doi:10.1007/978-3-319-09057-3, 2015.

Mesas-Carrascosa, F. J., Rumbao, I. C., Berrocal, J. A. B. and Porras, A. G. F.: Positional quality assessment of orthophotos obtained from sensors onboard multi-rotor UAV platforms, Sensors (Switzerland), 14(12), 22394–22407, doi:10.3390/s141222394, 2014.

Miřijovský, J. and Langhammer, J.: Multitemporal Monitoring of the Morphodynamics of a Mid-Mountain Stream Using UAS Photogrammetry, Remote Sens., 7(7), 8586–8609, doi:10.3390/rs70708586, 2015.

Miřijovský, J. and Vavra, A.: UAV PHOTOGRAMMETRY IN FLUVIAL GEOMORPHOLOGY, in 12th International Multidisciplinary Scientific GeoConference SGEM 2012, vol. 2, pp. 909–916., 2012.

Moreels, P. and Perona, P.: Evaluation of features detectors and descriptors based on 3D objects, Int. J. Comput. Vis., 73(3), 263–284, doi:10.1007/s11263-006-9967-1, 2007.

Niethammer, U., Rothmund, S., James, M. R., Travelletti, J. and Joswig, M.: UAV-based remote sensing of landslides, Int. Arch. Photogramm. Remote Sens. Spat. Inf. Sci. - ISPRS Arch., 38(2005), 496–501 [online] Available from: http://www.scopus.com/inward/record.url?eid=2-s2.0-84873737591&partnerID=tZOtx3y1, 2010.

Niethammer, U., James, M. R., Rothmund, S., Travelletti, J. and Joswig, M.: UAV-based remote sensing of the Super-Sauze landslide: Evaluation and results, Eng. Geol., 128, 2–11, doi:10.1016/j.enggeo.2011.03.012, 2012.

Prosdocimi, M., Calligaro, S., Sofia, G., Dalla Fontana, G. and Tarolli, P.: Bank erosion in agricultural drainage networks: New challenges from structure-from-motion photogrammetry for post-event analysis, Earth Surf. Process. Landforms, 40(14), 1891–1906, doi:10.1002/esp.3767, 2015.

Ruzgienė, B., Berteška, T., Gečyte, S., Jakubauskienė, E. and Aksamitauskas, V. Č.: The surface modelling based on UAV Photogrammetry and qualitative estimation, Measurement, 73, 619–627, doi:10.1016/j.measurement.2015.04.018, 2015.

Sandre Rivers Datasets (*French)*, available on http://www.sandre.eaufrance.fr/ (last accessed August 2016)

Smith, M. W., Carrivick, J. L. and Quincey, D. J.: Structure from motion photogrammetry in physical geography, Prog. Phys. Geogr., 40(2), 247–275, doi:10.1177/0309133315615805, 2015.

Sun Guoqing, R. and Jon Ranson, K.: Modeling lidar returns from forest canopies, IEEE Trans. Geosci. Remote Sens., 38(6), 2617–2626, doi:10.1109/36.885208, 2000.

Turner, D., Lucieer, A. and de Jong, S. M.: Time series analysis of landslide dynamics using an Unmanned Aerial Vehicle (UAV), Remote Sens., 7(2), 1736–1757, doi:10.3390/rs70201736, 2015.

Uysal, M., Toprak, A. S. and Polat, N.: DEM generation with UAV Photogrammetry and accuracy analysis in Sahitler hill, Meas. J. Int. Meas. Confed., 73, 539–543, doi:10.1016/j.measurement.2015.06.010, 2015.

Westoby, M. J., Brasington, J., Glasser, N. F., Hambrey, M. J. and Reynolds, J. M.: "Structure-from-Motion" photogrammetry: A low-cost, effective tool for geoscience applications, Geomorphology, 179, 300-314, doi:10.1016/j.geomorph.2012.08.021, 2012.

Addendum

A. Agisoft PhotoScan reports

Chabestan 2015

Agisoft PhotoScan
Processing Report
29 June 2016

Survey Data

Fig. 1. Camera locations and image overlap.

Legend		
■	> 9	
■	9	
■	8	
■	7	
■	6	
■	5	
■	4	
■	3	
■	2	
■	1	
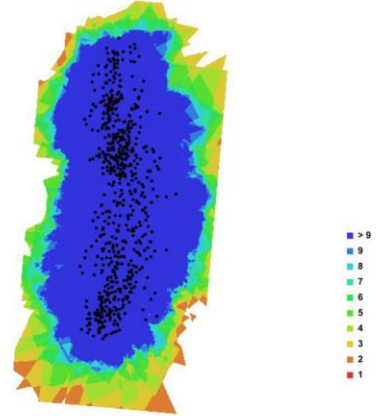
Number of images:	655	Camera stations:	650
Flying altitude:	136.044 m	Tie-points:	25168
Ground resolution:	0.0309351 m/pix	Projections:	231267
Coverage area:	0.413342 sq km	Error:	1.49597 pix

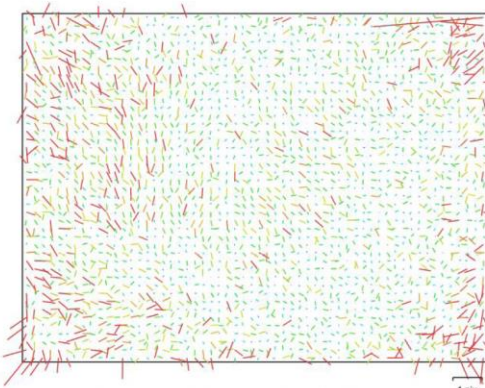| Camera Model	Resolution	Focal Length	Pixel Size	Precalibrated
Canon PowerShot D10 (6.2 mm)	4000 x 3000	6.2 mm	1.54199 x 1.54199 um	No

Table. 1. Cameras.

Camera Calibration

Fig. 2. Image residuals for Canon PowerShot D10 (6.2 mm).

Canon PowerShot D10 (6.2 mm)

Type:	Frame	K1:	-0.174155
Fx:	4138.03	K2:	0.0787695
Fy:	4138.39	K3:	0.162085
Cx:	2026.08	K4:	0
Cy:	1459.91	P1:	0.00034045
Skew:	-0.571084	P2:	-0.000468175

Ground Control Points

Fig. 3. GCP locations.

Label	X error (m)	Y error (m)	Z error (m)	Error (m)	Projections	Error (pix)
gcp1	0.077747	0.158170	0.016763	0.177040	31	0.500158
gcp2	-0.117183	-0.045896	0.027189	0.128754	34	0.413209
gcp3	-0.060403	0.080052	-0.041355	0.108476	38	0.555523
gcp4	-0.116347	-0.374641	-0.022561	0.392939	50	0.610509
gcp5	-0.119635	0.670676	-0.051756	0.683225	50	0.455566
gcp6	0.193415	-0.135313	-0.008277	0.236194	35	0.553253
gcp7	0.317443	0.186475	-0.001933	0.368167	45	0.647210
gcp8	0.124491	-0.171835	0.026858	0.213885	55	0.619063
gcp9	-0.415259	-0.264905	-0.004423	0.492579	69	0.732398
gcp10	0.013905	0.007505	-0.044013	0.046764	82	0.676167

Label	X error (m)	Y error (m)	Z error (m)	Error (m)	Projections	Error (pix)
gcp11	-0.005984	-0.431966	-0.090151	0.441314	81	0.595602
gcp12	-0.265251	-0.375152	-0.013199	0.459643	70	0.644317
gcp13	-0.104446	0.597886	0.024131	0.607420	66	0.567241
gcp14	0.309395	0.462144	-0.063916	0.559810	89	0.747336
gcp15	0.101438	-0.441092	0.011291	0.452746	107	0.647984
gcp16	-0.364868	-0.439869	-0.006404	0.571537	84	0.807571
gcp17	0.264053	-0.096090	-0.028703	0.282455	85	0.651889
gcp18	-0.271854	0.205304	-0.033131	0.342275	66	0.694222
gcp19	-0.107531	0.302825	-0.055645	0.326133	86	0.504891
gcp20	-0.103554	0.229314	-0.097632	0.269890	74	0.652788
gcp21	-0.175676	0.247338	-0.001768	0.303383	74	0.668785
gcp22	0.135677	-0.015551	0.028596	0.139527	60	0.783995
gcp23	-0.280280	-0.397345	0.040815	0.487961	61	0.675585
gcp24	-0.116252	0.489311	0.069381	0.507694	63	0.716796
gcp25	-0.039844	0.381491	0.024437	0.384344	70	0.588471
gcp26	-0.242744	-0.496447	-0.001097	0.552616	64	0.544651
gcp27	0.341591	-0.406100	-0.026725	0.531334	54	0.687537
gcp28	0.043112	-0.221059	0.016187	0.225804	44	0.653770
gcp29	0.162272	0.047976	-0.022161	0.170661	31	0.784469
gcp30	0.124512	0.277952	-0.012662	0.304829	34	0.509006
gcp31	0.335473	0.143597	0.058992	0.369652	53	0.526870
gcp32	-0.016801	-0.176026	0.013134	0.177313	54	0.612420
gcp33	-0.067768	-0.334403	-0.002537	0.341210	56	0.723544
gcp34	0.336168	0.402399	0.070004	0.528994	71	0.704894
gcp35	0.133273	0.195673	0.003390	0.236772	98	0.581911
gcp36	-0.184125	0.431937	-0.009036	0.469631	88	0.627364
gcp37	0.244939	-0.304732	0.036914	0.392707	59	0.687278
gcp38	0.141604	-0.299664	0.053479	0.335723	53	0.719712
gcp39	0.234930	-0.308564	0.106706	0.402231	53	0.690686
gcp40	-0.122501	0.113025	0.081623	0.185589	42	0.650040
gcp41	-0.271252	-0.216607	-0.011967	0.347331	65	0.499296
gcp42	0.043280	-0.342895	-0.012751	0.345851	66	0.567907
gcp43	0.027487	0.335959	-0.017622	0.337542	48	0.453326

Label	X error (m)	Y error (m)	Z error (m)	Error (m)	Projections	Error (pix)
gcp44	-0.224041	-0.321435	0.031332	0.393061	52	0.476309
gcp45	-0.103063	0.140400	-0.012429	0.174610	33	0.463143
gcp46	0.226296	0.017744	0.000053	0.226990	51	0.437602
gcp47	-0.110907	-0.201204	-0.019871	0.230604	38	0.412229
gcp48	0.208889	0.447213	0.007072	0.493643	53	0.503169
gcp49	0.042045	-0.485017	0.055013	0.489934	48	0.392067
gcp50	-0.093413	0.525378	-0.033766	0.534685	50	0.466585
gcp51	-0.071941	0.203751	-0.072275	0.227845	28	0.481255
Total	**0.193945**	**0.326524**	**0.041632**	**0.382055**	**3011**	**0.621027**

Table. 2. Control points.

Digital Elevation Model
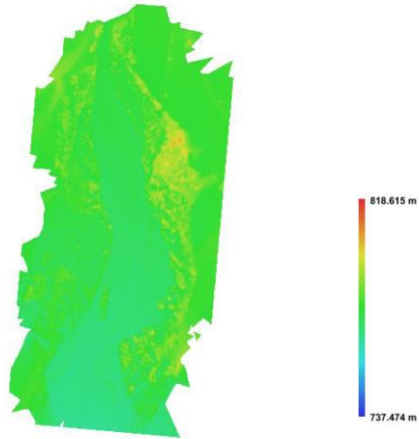
Fig. 4. Reconstructed digital elevation model.

Resolution:	0.0618702 m/pix
Point density:	261.239 points per sq m

Chabestan 2014

Agisoft PhotoScan

Processing Report
29 June 2016

Survey Data
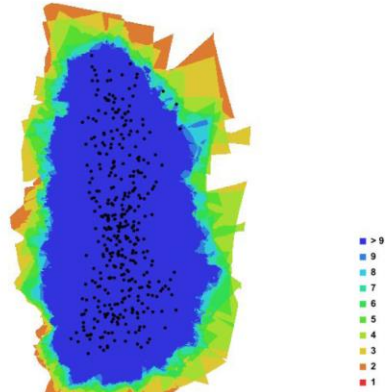
Fig. 1. Camera locations and image overlap.

Number of images:	380	Camera stations:	375
Flying altitude:	134.314 m	Tie-points:	19214
Ground resolution:	0.0306553 m/pix	Projections:	180788
Coverage area:	0.241589 sq km	Error:	1.23187 pix

Camera Model	Resolution	Focal Length	Pixel Size	Precalibrated
Canon PowerShot D10 (6.2 mm)	4000 x 3000	6.2 mm	1.54199 x 1.54199 um	No

Table. 1. Cameras.

Camera Calibration
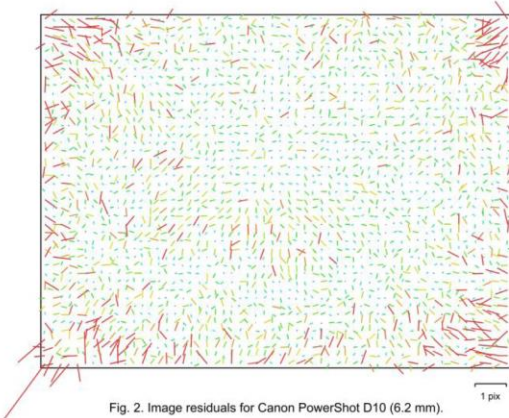
Fig. 2. Image residuals for Canon PowerShot D10 (6.2 mm).

Canon PowerShot D10 (6.2 mm)

Type:	Frame	K1:	-0.175445
Fx:	4143.28	K2:	0.0857232
Fy:	4143.28	K3:	0.147574
Cx:	2023.19	K4:	0
Cy:	1454.11	P1:	0.000296253
Skew:	0	P2:	-0.000338053

Ground Control Points

Fig. 3. GCP locations.

Label	X error (m)	Y error (m)	Z error (m)	Error (m)	Projections	Error (pix)
chabestan1	-0.286901	-0.326713	0.004833	0.434830	64	0.561019
chabestan2	-0.167945	0.067966	0.118049	0.216241	53	0.559617
chabestan3	-0.349546	-0.213430	0.013351	0.409772	49	0.460491
chabestan4	0.107437	0.085945	-0.031986	0.141253	38	0.418770
chabestan5	0.250761	-0.094537	-0.065738	0.275934	41	0.476203
chabestan6	-0.194665	0.113579	0.004300	0.225418	46	0.632628
chabestan7	0.234493	0.020733	-0.011482	0.235687	65	0.621765
chabestan8	0.207797	-0.046866	-0.002931	0.213037	57	0.723102
chabestan9	-0.051815	-0.234265	-0.002464	0.239939	73	0.537085
chabestan10	0.323751	-0.571632	-0.090636	0.663169	69	0.552491

| Label	X error (m)	Y error (m)	Z error (m)	Error (m)	Projections	Error (pix)
chabestan11	0.272137	-0.018518	-0.011622	0.273014	70	0.621170
chabestan12	-0.167706	-0.590351	-0.013216	0.613852	38	0.450330
chabestan13	-0.211330	0.380319	-0.054269	0.438461	48	0.774000
chabestan14	-0.268681	0.503064	-0.012270	0.570450	67	0.641561
chabestan15	0.106727	-0.520773	0.070604	0.536264	51	0.718997
chabestan16	0.221255	-0.052797	0.052158	0.233371	37	0.496062
chabestan17	0.085312	0.324595	-0.067647	0.342368	31	0.707060
chabestan18	-0.298919	0.066896	-0.068807	0.313946	27	0.363176
chabestan19	0.059143	-0.258283	0.068519	0.273684	33	0.358548
chabestan20	0.331537	0.264291	0.006883	0.424045	64	0.542215
chabestan21	-0.278203	0.459376	0.013095	0.537210	34	0.739894
chabestan22	0.104105	0.296588	-0.022032	0.315099	41	0.626733
chabestan23	-0.179063	-0.295396	-0.031535	0.346867	46	0.680100
chabestan24	0.193779	-0.035922	-0.035872	0.200318	47	0.654881
chabestan25	0.103469	0.275408	0.007360	0.294295	31	0.572125
chabestan26	-0.172417	-2.109117	0.168781	2.122873	66	0.625602
chabestan27	-0.284702	-0.432643	0.093861	0.526351	65	0.499343
chabestan28	0.092875	0.123577	-0.108352	0.188778	44	0.779478
chabestan29	-0.124330	0.104521	-0.066642	0.175567	49	0.594388
chabestan30	-0.243828	0.280920	0.015962	0.372321	53	0.566306
chabestan31	0.174357	0.382037	0.037055	0.421575	59	0.518010
chabestan32	0.154923	0.410419	-0.043632	0.440850	73	0.600635
chabestan33	0.400660	-0.236851	-0.052420	0.468374	77	0.560303
chabestan34	-0.144375	0.400664	-0.046705	0.428435	75	0.519232
chabestan35	-0.166885	-0.139241	0.081010	0.231950	63	0.566137
chabestan36	0.221982	0.379606	0.166310	0.470144	77	0.583261
chabestan37	0.072538	0.261767	-0.079507	0.283028	72	0.434166
chabestan38	-0.197242	0.236273	0.062155	0.313994	73	0.533706
chabestan39	0.071390	0.197930	-0.052628	0.216893	48	0.750922
chabestan40	-0.001087	0.542548	-0.047210	0.544599	48	0.731592
Total	**0.210068**	**0.452599**	**0.064684**	**0.503148**	**2162**	**0.591585**

Table. 2. Control points.

Digital Elevation Model
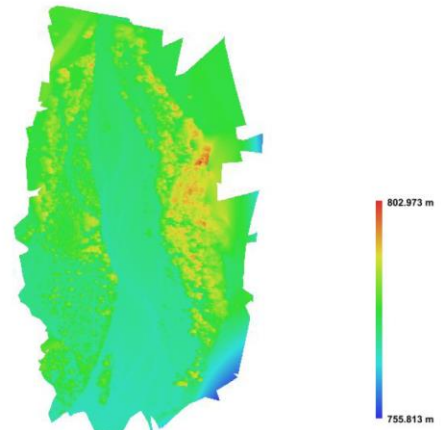
Fig. 4. Reconstructed digital elevation model.

Resolution: 0.0613106 m/pix
Point density: 266.029 points per sq m

La Bâtie-Montsaléon 2015
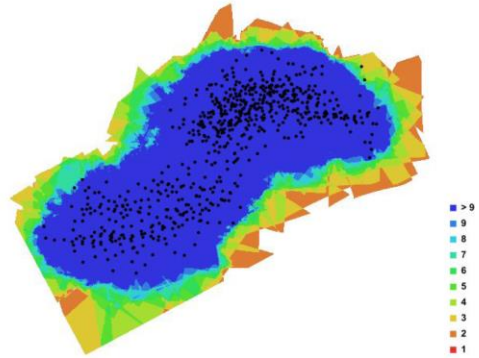
Agisoft PhotoScan

Processing Report
29 June 2016

Survey Data

Fig. 1. Camera locations and image overlap.

Number of images:	692	Camera stations:	681
Flying altitude:	121.457 m	Tie-points:	26329
Ground resolution:	0.0278395 m/pix	Projections:	257363
Coverage area:	0.339984 sq km	Error:	1.43604 pix

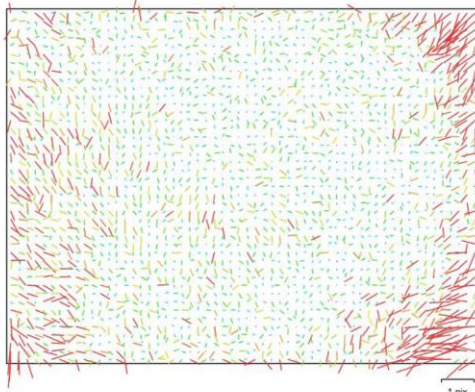| Camera Model	Resolution	Focal Length	Pixel Size	Precalibrated
Canon PowerShot D10 (6.2 mm)	4000 x 3000	6.2 mm	1.54199 x 1.54199 um	No

Table. 1. Cameras.

Camera Calibration

Fig. 2. Image residuals for Canon PowerShot D10 (6.2 mm).

Canon PowerShot D10 (6.2 mm)

Type:	Frame	K1:	-0.173434
Fx:	4142.91	K2:	0.077466
Fy:	4143.55	K3:	0.156066
Cx:	2025.39	K4:	0
Cy:	1458.83	P1:	0.000441472
Skew:	0.170553	P2:	-0.000509349

Ground Control Points

Fig. 3. GCP locations.

Label	X error (m)	Y error (m)	Z error (m)	Error (m)	Projections	Error (pix)
gcp1	-0.046922	-0.088691	0.046284	0.110499	4	0.201195
gcp2	-0.049620	0.079618	-0.015729	0.095124	21	0.426293
gcp3	0.354415	-0.231089	0.016264	0.423411	39	0.558997
gcp4	-0.213429	0.113704	-0.007941	0.241958	75	0.451367
gcp5	-0.309631	0.093750	0.010585	0.323686	107	0.429835
gcp6	-0.065811	0.006041	-0.010209	0.066872	93	0.435690
gcp7	-0.024955	-0.413179	0.024643	0.414665	103	0.562423
gcp8	0.261396	0.295038	0.034575	0.395690	84	0.638058
gcp9	0.298994	-0.157368	0.054999	0.342326	38	0.730198
gcp10	-0.243882	0.265785	0.018101	0.361176	39	0.767568

Label	X error (m)	Y error (m)	Z error (m)	Error (m)	Projections	Error (pix)
gcp11	-0.147141	0.295039	-0.012266	0.329923	34	0.538370
gcp12	0.121775	-0.227776	-0.005522	0.258344	32	0.516334
gcp13	0.156053	-0.326190	-0.012278	0.361805	48	0.526222
gcp14	0.271049	0.172559	-0.027793	0.322516	44	0.587401
gcp15	0.224802	-0.261590	-0.043499	0.347646	49	0.738355
gcp16	-0.246935	0.420141	0.015578	0.487584	47	0.479123
gcp17	0.027284	0.246664	0.040516	0.251454	40	0.481366
gcp18	-0.026572	0.176613	-0.020948	0.179825	50	0.557400
gcp19	-0.028317	-0.451881	-0.009326	0.452863	43	0.831190
gcp20	-0.109442	-0.087217	0.046499	0.147467	42	0.690364
gcp21	-0.210600	-0.427798	-0.008147	0.476896	52	0.594933
gcp22	-0.255875	0.214216	0.014366	0.334016	33	0.810217
gcp23	0.009448	0.184055	-0.023059	0.185734	29	0.814309
gcp24	0.336528	-0.278802	0.061774	0.441359	45	0.499783
gcp25	-0.122771	-0.143306	0.035379	0.191993	52	0.801532
gcp26	0.298291	0.596931	0.018163	0.667558	61	0.441354
gcp27	-0.069999	-0.106538	0.012607	0.128098	61	0.551197
gcp28	-0.030007	0.310415	-0.031050	0.313404	41	0.707118
gcp29	0.211524	-0.394545	-0.023194	0.448270	42	0.645397
gcp30	-0.170910	-0.273677	-0.043856	0.325627	50	0.558952
gcp31	-0.100483	0.095685	-0.046185	0.146238	79	0.561474
gcp32	-0.201390	0.407248	-0.018905	0.454715	84	0.565673
gcp33	-0.098912	-0.167556	-0.019212	0.195519	50	0.448151
gcp34	0.140409	0.294879	0.014888	0.326941	53	0.525369
gcp35	0.356889	-0.486529	-0.029234	0.604098	48	0.396443
gcp36	0.052886	0.377312	0.006829	0.381062	49	0.442100
gcp37	-0.013527	-0.236855	-0.002935	0.237259	91	0.370352
gcp38	-0.149186	0.017269	-0.019165	0.151400	62	0.442081
gcp39	-0.304162	-0.271257	-0.007378	0.407615	50	0.516468
gcp40	0.095995	0.362625	0.020324	0.375666	39	0.561900
Total	**0.193349**	**0.285160**	**0.027509**	**0.345625**	**2103**	**0.564262**

Table. 2. Control points.

Digital Elevation Model
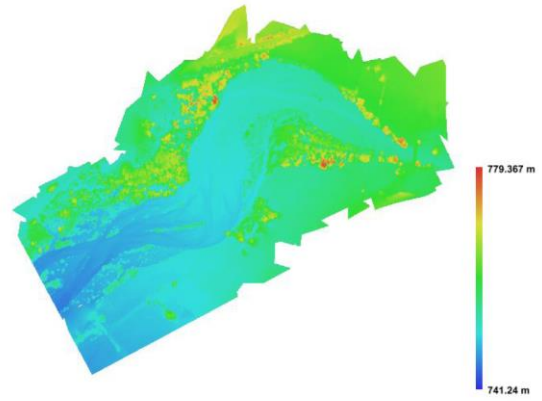
Fig. 4. Reconstructed digital elevation model.

Resolution:	0.0556789 m/pix
Point density:	322.566 points per sq m

La Bâtie-Montsaléon 2014
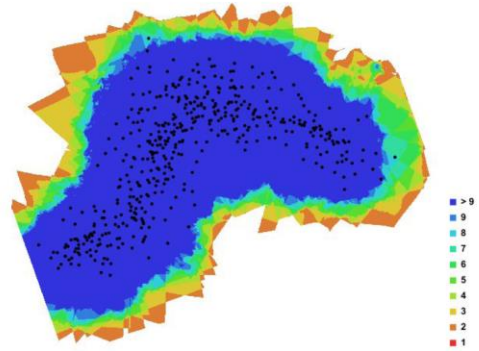
Agisoft PhotoScan

Processing Report
29 June 2016

Survey Data

Fig. 1. Camera locations and image overlap.

Number of images:	473	Camera stations:	470
Flying altitude:	135.946 m	Tie-points:	22766
Ground resolution:	0.0312966 m/pix	Projections:	196784
Coverage area:	0.268291 sq km	Error:	1.48848 pix

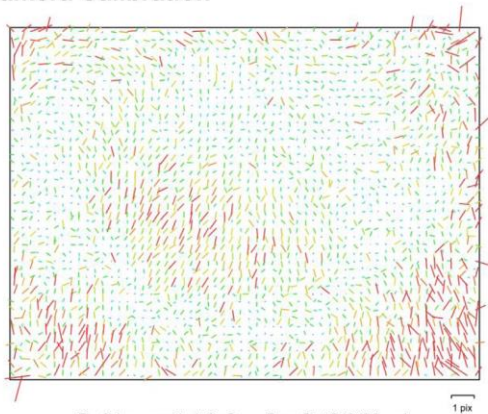| Camera Model	Resolution	Focal Length	Pixel Size	Precalibrated
Canon PowerShot D10 (6.2 mm)	4000 x 3000	6.2 mm	1.54199 x 1.54199 um	No

Table. 1. Cameras.

Camera Calibration

Fig. 2. Image residuals for Canon PowerShot D10 (6.2 mm).

Canon PowerShot D10 (6.2 mm)

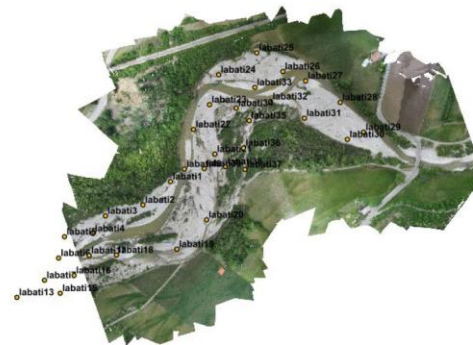|			
Type:	Frame	K1:	-0.177912
Fx:	4140.95	K2:	0.104345
Fy:	4140.95	K3:	0.115577
Cx:	2016.25	K4:	0
Cy:	1437.29	P1:	0
Skew:	0	P2:	0

Ground Control Points

Fig. 3. GCP locations.

Label	X error (m)	Y error (m)	Z error (m)	Error (m)	Projections	Error (pix)
labati1	0.184276	0.230524	-0.025262	0.296205	44	0.349489
labati2	-0.114948	-0.393417	-0.056514	0.413744	39	0.444863
labati3	-0.172628	0.402818	0.125267	0.455801	14	0.507295
labati4	0.035768	-0.242970	0.032470	0.247726	19	0.604191
labati5	0.085556	-0.297138	0.050621	0.313327	7	1.061063
labati6	0.196175	0.317191	-0.105130	0.387489	5	1.269894
labati7	0.066966	-0.532701	-0.004154	0.536910	3	0.430410
labati13	-0.062940	0.675803	-0.066897	0.682016	1	0.000000
labati15	-0.259423	0.186043	-0.085035	0.330369	2	0.263496
labati16	-0.078610	-0.040724	-0.024586	0.091882	9	0.600103

| Label	X error (m)	Y error (m)	Z error (m)	Error (m)	Projections	Error (pix)
labati17	-0.076467	0.361773	-0.008276	0.369859	23	0.443804
labati18	-0.187575	0.035585	-0.038489	0.194762	43	0.485493
labati19	0.213348	0.237894	-0.003990	0.319573	46	0.183036
labati20	0.147377	0.248091	0.003914	0.288590	39	0.442728
labati21	0.280358	0.387524	-0.027932	0.479119	65	0.591754
labati22	-0.369264	-0.048969	0.000597	0.372498	56	0.555821
labati23	-0.362677	-0.073938	-0.009811	0.370267	53	0.493985
labati24	-0.242130	-0.298151	-0.040917	0.386258	41	0.446370
labati25	0.021927	0.136136	0.006665	0.138052	19	0.494505
labati26	0.161916	-0.050351	-0.033542	0.172850	33	0.569727
labati27	0.068160	0.211579	0.010252	0.222523	32	0.499507
labati28	0.026755	0.336830	0.004312	0.337918	42	0.462607
labati29	0.061878	-0.402406	-0.008171	0.407218	59	0.260840
labati30	-0.336806	0.416557	-0.013050	0.535843	55	0.326078
labati31	0.174427	-0.422644	-0.009625	0.457324	64	0.623577
labati32	0.159478	-0.331627	-0.011307	0.368154	66	0.495056
labati33	-0.043382	-0.096379	0.012449	0.106423	64	0.567748
labati34	-0.018517	0.492977	0.028732	0.494160	76	0.618122
labati35	0.285511	-0.266364	0.046146	0.393186	70	0.550010
labati36	-0.014243	-0.199632	-0.004950	0.200201	51	0.509987
labati37	0.146595	0.255463	0.008693	0.294664	37	0.532025
labati38	0.107995	-0.266840	0.020005	0.288559	55	0.501716
labati39	0.089507	-0.402493	0.055974	0.416107	64	0.514699
labati40	-0.333517	0.026930	-0.039318	0.336905	56	0.452834
Total	**0.184781**	**0.314256**	**0.042250**	**0.366996**	**1352**	**0.507811**

Table. 2. Control points.

Digital Elevation Model
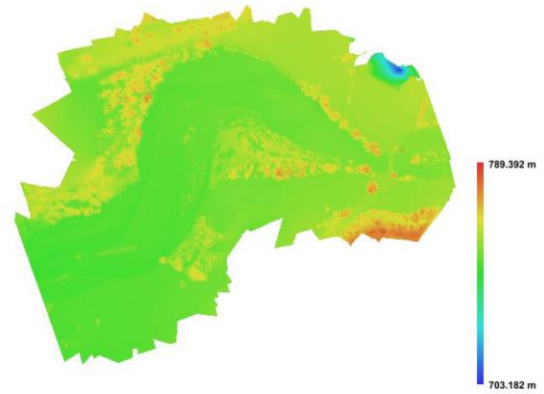
Fig. 4. Reconstructed digital elevation model.

Resolution: 0.0625933 m/pix
Point density: 255.238 points per sq m

Serres 2015
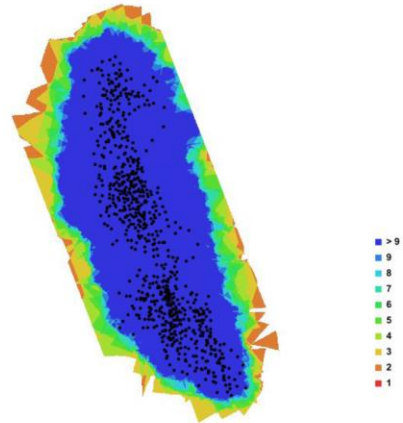
Agisoft PhotoScan

Processing Report
29 June 2016

Survey Data

Fig. 1. Camera locations and image overlap.

Number of images:	767	Camera stations:	765
Flying altitude:	123.67 m	Tie-points:	29401
Ground resolution:	0.0288747 m/pix	Projections:	286055
Coverage area:	0.430663 sq km	Error:	1.51316 pix

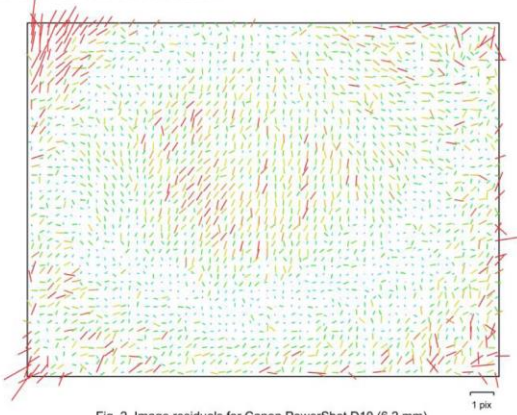| Camera Model	Resolution	Focal Length	Pixel Size	Precalibrated
Canon PowerShot D10 (6.2 mm)	4000 x 3000	6.2 mm	1.54199 x 1.54199 um	No

Table. 1. Cameras.

Camera Calibration

Fig. 2. Image residuals for Canon PowerShot D10 (6.2 mm).

Canon PowerShot D10 (6.2 mm)

Type:	Frame	K1:	-0.173023
Fx:	4136.36	K2:	0.0724276
Fy:	4136.36	K3:	0.17431
Cx:	2029.44	K4:	0
Cy:	1449.86	P1:	0
Skew:	0	P2:	0

Ground Control Points

Fig. 3. GCP locations.

Label	X error (m)	Y error (m)	Z error (m)	Error (m)	Projections	Error (pix)
gcp1	-0.049256	-0.169993	0.032557	0.179954	55	0.369282
gcp2	-0.202486	-0.045495	0.056678	0.215134	37	0.565090
gcp3	0.085745	0.144359	-0.042584	0.173220	33	0.891253
gcp4	0.180674	-0.325089	-0.021103	0.372520	32	0.452213
gcp5	-0.146896	0.226873	-0.024055	0.271345	33	0.636014
gcp6	-0.003713	-0.208066	0.010504	0.208364	23	0.487709
gcp7	-0.272540	-0.148065	0.012985	0.310435	44	0.540586
gcp8	-0.212748	0.017781	0.006288	0.213582	28	0.347140
gcp9	0.147535	-0.040263	0.014157	0.153584	32	0.206041
gcp10	-0.018081	0.072158	-0.022582	0.077741	17	0.277538

Label	X error (m)	Y error (m)	Z error (m)	Error (m)	Projections	Error (pix)
gcp11	-0.120854	0.230520	-0.018214	0.260915	40	0.459124
gcp12	0.139036	-0.276248	0.024232	0.310212	42	0.340411
gcp13	0.291232	0.242676	0.019997	0.379615	69	0.302829
gcp14	-0.016382	0.193795	-0.010896	0.194791	73	0.254399
gcp15	0.318979	-0.170175	-0.006264	0.361588	68	0.394121
gcp16	-0.275399	0.093827	0.003404	0.290963	52	0.425813
gcp17	-0.149610	0.056969	-0.034441	0.163752	53	0.260842
gcp18	0.342227	-0.231962	0.045904	0.415972	46	0.721495
gcp19	-0.408955	0.036886	-0.004569	0.410640	54	0.413973
gcp20	0.308785	0.409134	0.010448	0.512687	71	0.461249
gcp21	0.064420	-0.348163	0.009695	0.354205	65	0.395696
gcp22	-0.163501	0.401835	-0.012425	0.434003	78	0.440250
gcp23	0.269192	0.294697	-0.055248	0.402943	63	0.387461
gcp24	0.317076	-0.162530	-0.035976	0.358116	59	0.468359
gcp25	0.126262	-0.218131	-0.053848	0.257727	58	0.434774
gcp26	-0.253572	-0.413690	0.006273	0.485260	46	0.609403
gcp27	-0.280647	-0.094705	0.065880	0.303433	58	0.589336
gcp28	-0.284901	0.555230	-0.025302	0.624571	50	0.574775
gcp29	-0.005145	0.018515	0.051358	0.054836	49	0.579806
gcp30	-0.064612	-0.448665	-0.036112	0.454729	48	0.423950
gcp31	0.334285	0.096395	-0.008306	0.348005	44	0.439151
gcp32	-0.302506	-0.089331	0.018550	0.315965	45	0.648866
gcp33	0.403932	0.554753	0.029459	0.686862	40	0.590133
gcp34	-0.000412	-0.011095	0.023688	0.026161	33	0.463787
gcp35	-0.033394	0.018403	-0.005831	0.038572	10	0.652401
gcp36	0.049845	-0.114664	-0.087596	0.152661	28	0.706309
gcp37	0.189591	-0.111362	-0.026355	0.221452	34	0.618456
gcp38	-0.027032	0.122883	0.044910	0.133596	39	0.481696
gcp39	-0.284919	-0.085447	0.005582	0.297509	42	0.552972
gcp40	0.007920	-0.074106	0.028043	0.079629	33	0.594476
Total	**0.216884**	**0.238918**	**0.032628**	**0.324323**	**1824**	**0.489357**

Table. 2. Control points.

Digital Elevation Model

733.239 m

676.025 m
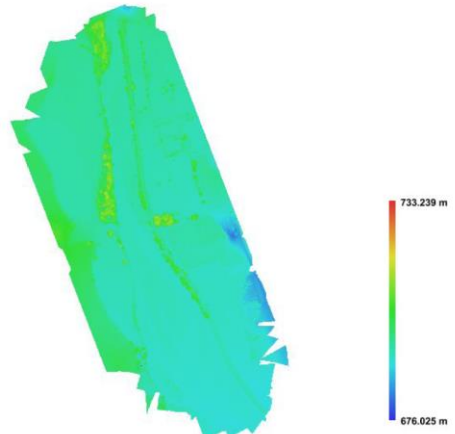
Fig. 4. Reconstructed digital elevation model.

Resolution:	0.0577494 m/pix
Point density:	299.851 points per sq m

Serres 2014

Agisoft PhotoScan

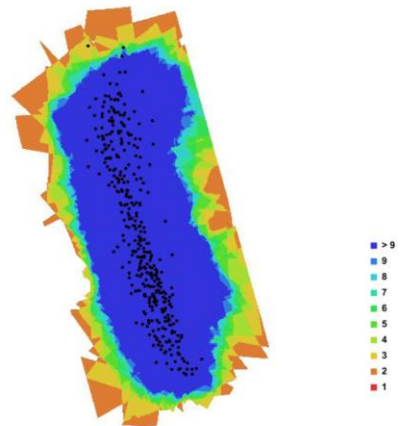Processing Report
29 June 2016

Survey Data

Fig. 1. Camera locations and image overlap.

Number of images:	370	Camera stations:	365
Flying altitude:	139.483 m	Tie-points:	20706
Ground resolution:	0.0318892 m/pix	Projections:	213074
Coverage area:	0.249482 sq km	Error:	1.40952 pix

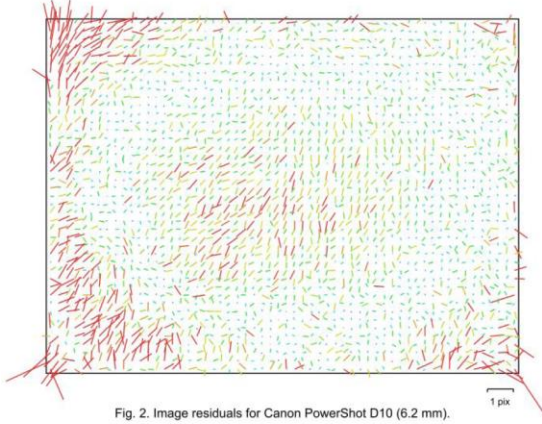| Camera Model	Resolution	Focal Length	Pixel Size	Precalibrated
Canon PowerShot D10 (6.2 mm)	4000 x 3000	6.2 mm	1.54199 x 1.54199 um	No

Table. 1. Cameras.

Camera Calibration

Fig. 2. Image residuals for Canon PowerShot D10 (6.2 mm).

Canon PowerShot D10 (6.2 mm)

Type:	Frame	K1:	-0.172623
Fx:	4141.06	K2:	0.0664619
Fy:	4141.06	K3:	0.191824
Cx:	2016.81	K4:	0
Cy:	1433.12	P1:	0
Skew:	0	P2:	0

Ground Control Points

Fig. 3. GCP locations.

Label	X error (m)	Y error (m)	Z error (m)	Error (m)	Projections	Error (pix)
serres1	-0.256883	0.062160	0.021042	0.265133	40	0.410005
serres2	-0.092985	0.330845	-0.005738	0.343711	54	0.492609
serres3	-0.203174	-0.155857	0.000613	0.256070	71	0.286777
serres4	-0.175078	-0.253487	-0.007295	0.308158	50	0.422056
serres5	0.200256	0.166150	0.003806	0.260236	15	0.304546
serres6	-0.039304	-0.075000	-0.015869	0.086149	42	0.488002
serres7	0.177087	0.099300	-0.013830	0.203498	61	0.358868
serres8	-0.031030	-0.089703	0.035951	0.101499	43	0.545261
serres9	0.346028	-0.153060	0.019728	0.378882	78	0.481184
serres10	-0.204374	0.113390	-0.035816	0.236451	73	0.417426

Label	X error (m)	Y error (m)	Z error (m)	Error (m)	Projections	Error (pix)
serres11	0.013559	-0.036119	0.007844	0.039370	7	0.185037
serres12	-0.162769	-0.438177	-0.058934	0.471132	1	0.000000
serres13	-0.000000	0.000000	0.000000	0.000000		
serres14	-0.014135	-0.002577	0.032985	0.035979	3	0.056042
serres15	0.161050	-0.008513	-0.016731	0.162140	22	0.306552
serres16	-0.209140	0.094570	-0.020915	0.230479	43	0.248212
serres17	0.052343	-0.089104	0.035283	0.109197	70	0.456750
serres18	0.223868	-0.067169	-0.024638	0.235022	68	0.534416
serres19	0.059442	0.081991	-0.001723	0.101286	79	0.378894
Total	**0.167801**	**0.163963**	**0.024221**	**0.235855**	**820**	**0.424434**

Table. 2. Control points.

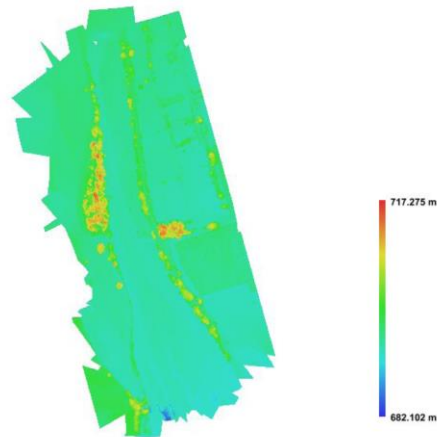## Digital Elevation Model

717.275 m

682.102 m

Fig. 4. Reconstructed digital elevation model.

Resolution: 0.0637785 m/pix
Point density: 245.839 points per sq m